NANOSTRUCTURED GLASS COVERS FOR PHOTOVOLTAIC APPLICATIONS

MRIDUL SAKHUJA

(BSc. (Hons.), University of Delhi, New Delhi, India)

A THESIS SUBMITTED

FOR THE DEGREE OF DOCTOR OF PHILOSOPHY

DEPARTMENT OF ELECTRICAL AND COMPUTER ENGINEERING

NATIONAL UNIVERSITY OF SINGAPORE

2014

Declaration

I hereby declare that this thesis is my original work and it has been written by me in its entirety. I have duly acknowledged all the sources of information which have been used in this thesis.

This thesis has also not been submitted for any degree in any university previously.

Mridul Sakhuja

Mridul Sakhuja

17 January 2014

Acknowledgements

Firstly, I would like to express my deep and sincere gratitude to my supervisors Assoc. Prof. Aaron J. Danner and Prof. Charanjit S. Bhatia for their invaluable guidance, advice and counselling during my Ph.D candidature. I would also like to thank Assoc. Prof. Hyunsoo Yang for his guidance and help on this project. It was an absolute pleasure and honour to conduct my research under their supervision. Their patience and assurance during difficult times will always be remembered.

I am also thankful to Dr. Lalit Kumar Verma, Dr. Son Jae Sung, Mr. Lamine Benaissa, and Mr. Le Hong Vu, with whom I have had the privilege to work and learn during my candidature.

Special thanks to all my peers from Sri Venkateswara College, University of Delhi, New Delhi, for helping and guiding me during my initial days at the National University of Singapore (NUS). I would also like to thank my friends and colleagues in the Spin and Energy Lab (SEL) and the Centre for Optoelectronics (COE) for their invaluable help, support and friendship. Many thanks to the lab managers, Ms. Musni bte Hussain, Mr. Tan Beng Hwee and Mr. Jung Yoon Yong Robert, for their help during my study in NUS. I would also like to thank Dr. Timothy Walsh, Dr. Ian Marius Peters, Mr. Jai Prakash Singh and Ms. Nasim Sahraei from the Solar Energy Research Institute of Singapore (SERIS) for their invaluable help and guidance during this PhD candidature. The experimental facilities provided by SERIS for this research work are acknowledged with thanks.

I would like to thank Dr. Wang Qing from Department of Materials Science and Engineering and Prof. Hua Chun Zeng from Department of

Chemical and Biomolecular Engineering to provide their facilities for this research work.

I would also like to thank my friends Subhasis Banerji, Prof. Hector Rafael Orozco Aguirre, Shantanu Samajdar, Daphne Debby Menezes, Gautam Singh, Dr. Ganesh Iyer, Dr. Chaitanya Kantak, Shreya Kundu, Dr. Nikita Gaur, Wong Elaine, Dr. Deng Jun, Siew Shawn Yohannes, Dr. Liao Baochen, Ho Jian Wei and Tung Kar Hoo Patrick for their amazing friendship and support.

I would also like to acknowledge the support provided by Singapore National Research Foundation grant number NRF2008EWT-CERP02-032 for this work. Also, I am truly grateful to the National University of Singapore for an NUS scholarship.

Last but not least, I would like to thank my family for their endless love, inspiration and encouragement. I would like to thank Almighty God, who always showers his kindness on me at every moment of my life.

A big heartfelt thank you to everyone!!

Mridul Sakhuja

Table of Contents

Abstract

Glass covers are an integral part of solar modules since they provide mechanical stability to the underlying solar cells. Their optical transparency, chemical and thermal stability have made them ideal as front covers for solar modules. However, reflection losses and accumulation of dust particles at the primary air-glass interface affect the omnidirectional optical transmission of these glass covers. These losses further affect the overall power conversion efficiency of the underlying solar cells. These optical losses can be minimized by introducing smart coatings or surfaces on the glass covers that combine both antireflective and self-cleaning properties. This represents a potentially important way of improving solar module efficiency, and one that has not been thoroughly studied as other loss mechanisms.

In this thesis, smart omnidirectionally antireflective and self-cleaning glass covers based on nanoscale texturing are fabricated using a developed and optimized non-lithographic process. This fabrication process provides advantages of being simple, easy and scalable, and is particularly suitable for solar packaging glass, where highly ordered texture is not required.

Initially, computational studies are carried out to confirm the antireflective effect of nanostructures on the optical properties of planar glass. Periodic cylindrical textures with varying feature sizes on the surface of glass are simulated. Stochastic textures with optimized nanostructure size distributions are subsequently simulated, exhibiting enhancement in both broadband and omnidirectional antireflection properties, similar to results from periodic textures.

The nanostructured glass samples are fabricated with varying pitches and diameter but with uniform heights. These samples are then measured for their omnidirectional transmission. An absolute gain of ~3.4% in broadband transmission at normal incidence is observed, with an omnidirectional improvement also noted. Multicrystalline silicon solar cells are then packaged with nanostructured glass samples which showed a gain of 1.0 % (absolute) in the absolute power conversion efficiency.

Since the improvement in transmission does not translate to an effective performance of a solar module in real-life conditions, both planar and nanostructured glass samples are tested outdoors in the tropical climate of Singapore for 3 months. The samples are mounted flat, as well as at inclinations of 10° and 20°. The nanostructured glass samples provide superior antireflective and self-cleaning performance compared to a planar glass sample over the testing period. They also show the best performance when tested as packaging covers of solar modules, with a reduction in efficiency of only 0.3% over a testing period of 5 weeks. Thus, the performance of these nanostructured glass samples in real-life conditions is confirmed.

Subsequently, the scattering properties of the nanostructured glass samples are also studied where it is observed that low aspect ratio features provide less scattering compared to high aspect ratio features. These nanostructured glass samples are also used as packaging covers of solar modules and their external quantum efficiency is measured.

Summarizing, this thesis has focused on creating antireflective and self-cleaning technology for the solar module glass covers. Moreover, the fabrication technique also has potential of being scalable, and is a promising candidate for large area production of nanostructured glass panels.

List of Publications

Publications in peer-reviewed journals

1. **M. Sakhuja**, N. Sahraei, M. Peters, H. Yang, C. S. Bhatia, and A. J. Danner, “Study of optical scattering by nanostructured glass for photovoltaic applications”, Under Review, Solar Energy Materials and Solar Cells.
2. **M. Sakhuja**, J. Son, H. Yang, C. S. Bhatia, and A. J. Danner, “Outdoor performance and durability testing of antireflecting and self-cleaning glass for photovoltaic applications”, Under Review, Solar Energy.
3. J. Son, **M. Sakhuja**, A. J. Danner, C. S. Bhatia, and H. Yang, “Large scale antireflective glass texturing using grid contacts in anodization methods”, Solar Energy Materials and Solar Cells, 116, pp. 09-13, 2013.
4. **M. Sakhuja**, J. Son, L. K. Verma, H. Yang, C. S. Bhatia, and A. J. Danner, “Omnidirectional study of nanostructured glass packaging for solar modules”, Progress in Photovoltaics: Research and Applications, 22, pp. 356-361, 2014. (Published online – September 2012).
5. J. Son, S. Kundu, L. K. Verma, **M. Sakhuja**, A. J. Danner, C. S. Bhatia, and H. Yang, “A practical superhydrophilic self cleaning and antireflective surface for outdoor photovoltaic applications”, Solar Energy Materials and Solar Cells, 98, pp. 46-51, 2012.
6. L. K. Verma, **M. Sakhuja**, J. Son, A. J. Danner, H. Yang, H. C. Zeng, and C. S. Bhatia, “Self-cleaning and antireflective packaging glass for solar modules”, Renewable Energy, 36, pp. 2489-2493, 2011.

Conferences

1. **Oral and Conference Paper**: **M. Sakhuja**, H. Yang, C. S. Bhatia, and A. J. Danner, "Antireflective and self-cleaning glass for solar modules: Investigation of outdoor performance and durability", International Photovoltaic Science and Engineering Conference 23 (PVSEC 23), October 28 – November 1, 2013, Taipei, Taiwan.
2. **Oral**: **M. Sakhuja**, C. Z. Yap, G. Perera, H. M. Teng, C. M. Maung, L. J. George, S. H. Shin, E. s/o Dayalan, L. T. Tan, and A. J. Danner, "Photocatalytic activity of sputtered titanium dioxide on solar cell efficiency", 2nd International Conference on Solar Energy Materials, Solar Cells and Solar Energy Applications, Solar Asia 2013, August 22 – 24, 2013, Kuala Lumpur, Malaysia.
3. **Oral**: **M. Sakhuja**, H. Yang, C. S. Bhatia, and A. J. Danner, "Antireflective and self-cleaning packaging glass for solar modules". 27th European Photovoltaic Solar Energy Conference and Exhibition (EUPVSEC), September 24-28, 2012, Frankfurt, Germany. (**Best Student Paper Award**)
4. **Invited Talk**: **M. Sakhuja**, J. Son, L. H. Vu, C. S. Bhatia, H. Yang, and A. J. Danner, "Nanopatterned and self-cleaning glass substrates for solar cell packaging", India-Singapore Joint Physics Symposium (ISJPS), February 20-22, 2012, New Delhi, India.
5. **Keynote Talk and Conference Paper**: **M. Sakhuja**, J. Son, L. H. Vu, L. K. Verma, X. Baojuan, H. C. Zeng, H. Yang, A. J. Danner, and C. S. Bhatia, "Nanopatterned and self-cleaning glass substrates for solar cell packaging", The 2nd International Conference on Control,

Instrumentation and Automation (ICCIA), December 27-29, 2011, Shiraz, Iran, pp. 90-101.

6. **Poster**: **M. Sakhuja**, L. K. Verma, H. Yang, C. S. Bhatia, and A. J. Danner, "Parameter optimization of nanostructured glass for solar cell packaging". International Conference on Materials for Advanced Technologies (ICMAT), June 26 – July 1, 2011, Suntec Convention Centre, Singapore.
7. **Poster and Conference Paper**: **M. Sakhuja**, L. K. Verma, H. Yang, C. S. Bhatia, and A. J. Danner, "Fabrication of tilted nanostructures for omnidirectional transmission in solar modules", Proceedings of 37th IEEE Photovoltaics Specialists Conference, June 19-24, 2011, Seattle, Washington, United States of America, pp. 000932-000935.
8. **Poster**: **M. Sakhuja**, L. Benaissa, L. K. Verma, H. Yang, A. J. Danner and C. S. Bhatia "EBIC characterization for direct extraction of diffusion length of semiconducting materials", MRS-S Trilateral Conference on Advances in Nanoscience: Energy, Water and Healthcare, August 11-13, 2011, IMRE, NUS, Singapore.

List of Figures

List of Acronyms

TW	Terawatt
CO_2	Carbon dioxide
PV	Photovoltaic
EVA	Ethyl vinyl acetate
FDTD	Finite difference time domain
I-V	Current voltage
CVD	Chemical vapour deposition
PS	Polystyrene
PMMA	Polymethyl methacrylate
UV	Ultraviolet
POSS	Polyhedral oligomeric silsesquioxane
PDMS	Polydimethylsiloxane
RTA	Rapid thermal annealing
ICP-RIE	Inductively coupled plasma reactive ion etching
SEM	Scanning electron microscope
SR	Spectral responsivity
EQE	External quantum efficiency
E	Electric field
H	Magnetic field
PML	Perfect matching layer
RTP	Rapid thermal processing
CFP	Conventional furnace processing
DI	Deionized

List of Symbols

Si	Silicon
GaAs	Gallium arsenide
I_{sc}	Short circuit current
V_{oc}	Open circuit voltage
P_{mpp}	Maximum output power
FF	Fill factor
η	Efficiency
J_{sc}	Short circuit current density
I_m	Maximum current
V_m	Maximum voltage
θ_c	Contact angle
R	Reflectance
n_1	Refractive index of the source medium
n_2	Refractive index of thin film or material substrate
θ_1	Angle of incidence
θ_2	Angle of refraction
HNO_3	Nitric acid
Si_3N_4	Silicon nitride
n_{layer}	Refractive index of thin film single antireflective layer
n_0	Refractive index of air
n_s	Refractive index of substrate
MgF_2	Magnesium fluoride
TiO_2	Titanium dioxide
SiO_2	Silicon dioxide/Silica
Al_2O_3	Aluminium oxide

ZrO_2	Zirconium oxide
CeF_3	Cerium fluoride
n_{pc}	Refractive index of porous medium
n_{dc}	Refractive index of dense medium
P	Porosity percentage
Ni	Nickel
d	period for zero order grating
m	integer order number
θ_{in}	angle of incidence
θ_m	outgoing propagation angle of order m
SF_6	Sulphur hexafluoride
HF	Hydrofluoric
γ_{sg}	Surface tension between solid and gas phase
γ_{sl}	Surface tension between solid and liquid phase
γ_{lg}	Surface tension between liquid and gas phase
θ_w	Apparent contact angle
r	Surface roughness
φ	Surface fractions of different phases
φ_s	Fraction of solid surface wet by the liquid
ZnO	Zinc oxide
n	Refractive index
λ	Wavelength in free space
c	Speed of light
α	Absorption
$\theta_{t(r)}$	Zenithal angle of emergence of transmitted (or reflected) radiation
$\varphi_{t(r)}$	Azimuthal angle of emergence of transmitted (or reflected) radiation

θ_i, φ_i	Angle of incidence on incoming radiation illuminating a sample
d	Thickness of antireflection coating
n_{eff}	Effective refractive index of an antireflection coating
n_s	Refractive index of the substrate
f	Filling factor
ε_T	Strain in thin film due to thermal mismatch
α_s	Thermal expansion coefficient of the film
α_f	Thermal expansion coefficient of the substrate
ε_0	Strain in the film before temperature is applied

List of Equations

List of Tables

1. Introduction and Motivation

1.1 Solar Technology Outlook

The energy crisis [1] has become a major concern in recent years. It is expected that the population density will dramatically increase from the present 7 billion to at least 9 billion by 2050 [2]. With this as a background, the demand for energy consumption will almost certainly rise in the decades to come. In fact, the global energy consumption rate is predicted to increase at a rate of 300% (threefold) from 13.5 Terawatt (TW) in 2001 to approximately 40.8 TW in 2050, mainly driven by growth in developing nations [3].

The greatest challenge is the fact that this increase in consumption must be accompanied by a significant reduction in carbon dioxide (CO_2) emissions [4]. This is an exceptional task, considering the fact that fossil fuels currently dominate energy production. However, depreciating reserves of fossil fuels are far from able to meet the demands of the surging population, which exerts intense pressure on socio-economic development of the world [5]. Therefore, it is essential to find ways of investigating and applying alternative routes of energy generation, such as renewable sources like solar, wind, geothermal, tidal, wave, hydropower and biomass, which do not contribute to CO_2 emissions.

Solar energy has proved to be a promising candidate to replace fossil fuels to a certain extent; solar energy could theoretically provide as much as 1.2×10^5 TW [6], far more than the other energy sources. Solar energy is advantageous since it is readily available free, and is also a clean source of energy. 14 TWh [6] of converted electrical power can be provided by an hour irradiation of Sun on the surface of Earth, which amounts to the annual energy consumption of the world. Solar energy has been widely explored and converted to other useful forms of energy such as heat [7], electricity [8] and chemical fuels [9]. Solar cells have been a useful source of energy, converting solar radiation into electricity through the photovoltaic (PV) effect for about 60 years. A number of PV technologies have entered the market, the largest being crystalline silicon (Si) solar cells [10], with a market share of 85% in 2010, and thin film solar cells which make up the remaining 15%.

The PV industry is undergoing rapid development, with annual growth rates of 45% for the last 15 years [12]. Figure 1.1 shows the yearly installed capacity in MW_p. W_p (watt-peak) denotes the output of solar modules at standard test conditions with a solar irradiance of 1000 W/m^2. Extensive research and new fabrication technologies are reducing the cost of solar cells, which has helped to increase the installed capacity [11].

Prices for solar modules have also decreased drastically over the years; the per-watt net cost was 0.85 $\$/W_p$ in 2011, and is predicted to drop to 0.36

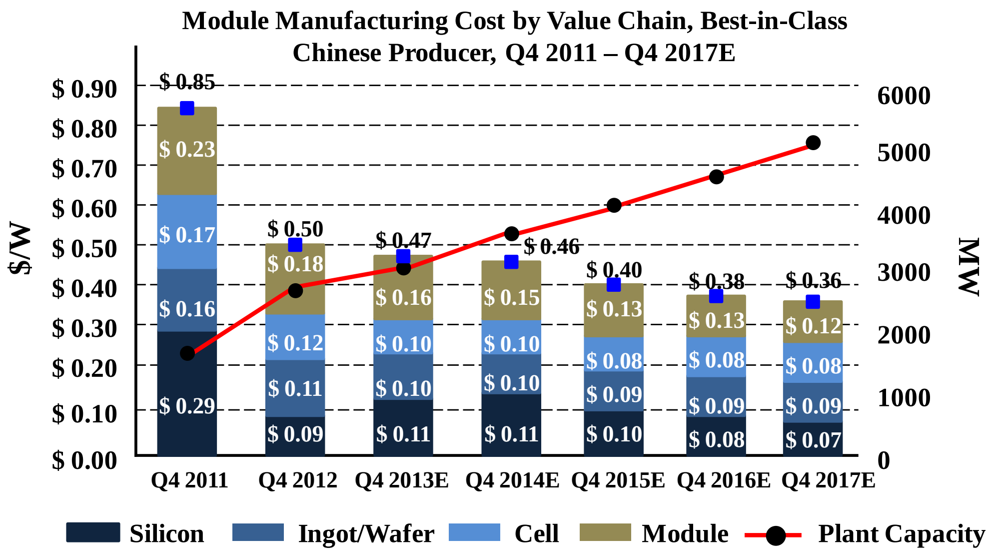

Figure 1.1 Yearly installed capacity (MW) and cost per watt for Si solar modules [11].

$/Wp by the year 2017 [13]. This has allowed the investment and application of PV technology in most of the developed and developing world energy markets. The trend of module cost over the years of development can be seen in figure 1.1. To allow further development and cost reduction of the price of solar modules, constant effort has to be made to increase the efficiency of solar cells.

1.2 Solar Module: Components and Measurement Parameters

A solar cell is defined as a device that directly converts the Sun’s energy into electrical energy through the PV effect. The development of solar cells began in 1839 by a French physicist Alexandre-Edmond Becquerel when he found that certain materials produce small amounts of electric current when exposed to light [14]. This conversion of incident light into electric current is known as the PV effect. However, the first efficient solar cell was fabricated at Bell Laboratories in 1954 [15]. Since then, the field of PV has witnessed a wide variety of solar cells ranging from crystalline Si solar cells, amorphous Si solar cells, organic solar cells, dye-sensitized solar cells, multijunction solar cells and many more fabricated using different light sensitive materials such as Si and gallium arsenide (GaAs).

When used for practical applications, a single solar cell might not be powerful enough to provide the required current and voltage to drive an electrical circuit. Therefore, a number of solar cells are typically electrically connected, usually in series to each other and packaged or encapsulated into an assembly known as a solar module. The different components of a solar module are shown in figure 1.2.

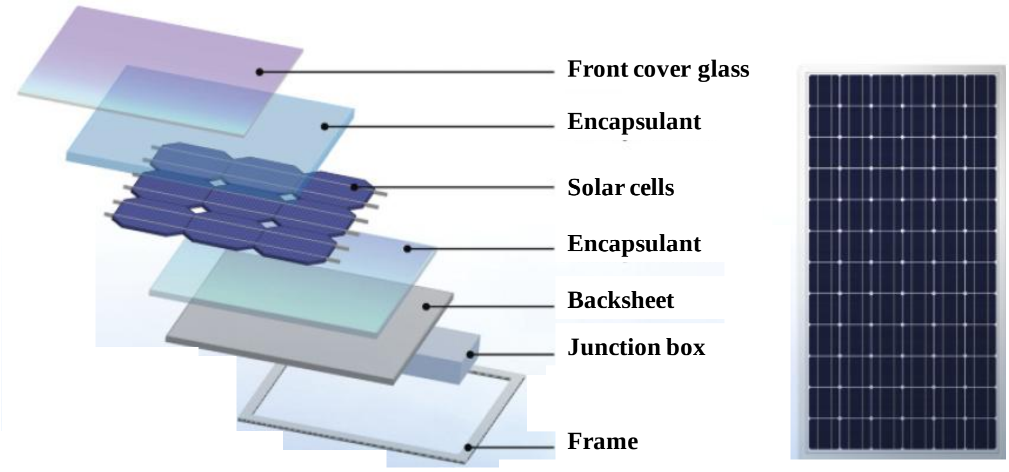

Figure 1.2 Components of a solar module [16].

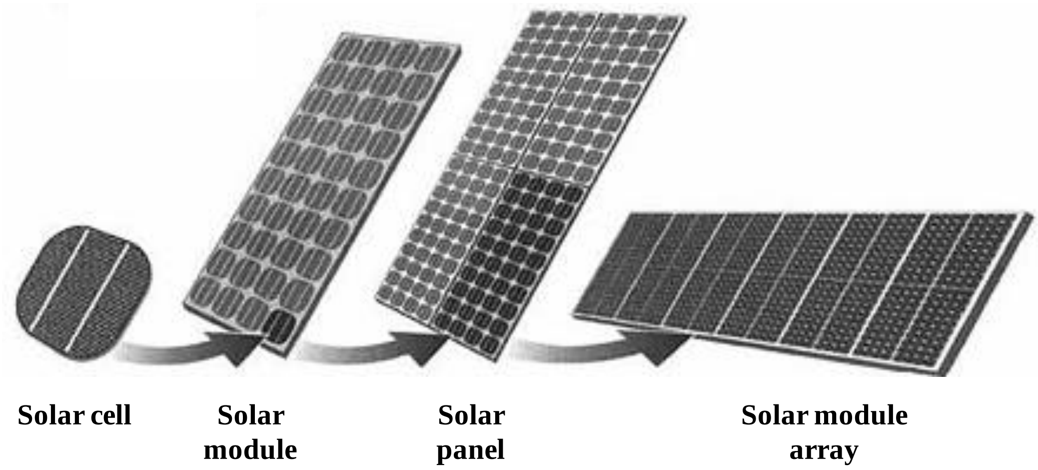

Figure 1.3 Different stages of assembly in a PV system [17].

A solar module consists of a finite number of solar cells electrically connected and placed between a tough and protective glass in the front and usually a Tedlar backsheet within a frame and sealed using an encapsulant material, usually ethyl vinyl acetate (EVA).

When the packaged solar modules are electrically connected to each other and mounted on a supporting structure, it is known as a solar panel. If numerous solar panels are connected and mounted together on a supporting structure, it is known as a solar module array. Different stages of assembly are shown in figure 1.3.

The performance of solar cells and solar modules is usually governed by certain electrical parameters such as short circuit current (I_{sc}), open circuit voltage (V_{oc}), output power (P_{mpp}), fill factor (FF) and efficiency (ƞ). A typical current-voltage (I-V) curve for a solar cell is shown below in figure 1.4.

The electrical parameters which govern the performance of a solar cell are defined below:

1) **I_{sc}**: Short circuit current is defined as the current through a solar cell when the voltage across the solar cell is zero. This current is due to the generation and collection of charge carriers when light is irradiated on the solar cell. The current generated by the solar cell depends on the area of the solar cell (larger the area of solar cell, higher the current generated), intensity of the incident light (governs the number of photons striking the surface of solar cell), optical properties of the cell's surface and the module components, and the collection probability of the solar cell (depends on the surface passivation of the cell). When the output current for a solar cell or a solar module is reported, it is usually reported per unit area. This current per unit illuminated area is known as short circuit current density (J_{sc}).

2) **V_{oc}**: Open circuit voltage is defined as the maximum voltage available from a solar cell when the current is zero. V_{oc} depends on the saturation current (depends on recombination in the solar cell) and I_{sc}.

3) **P_{mpp} and FF**: I_{sc} and V_{oc} are the current and voltage that can be derived from a solar cell device. However, their net product, which is P_{mpp}, is zero at both these operating points (I_{sc} and V_{oc}). The FF determines the maximum power from the solar cell when none of the current and voltage values are zero. These values of current and voltage that define the maximum power are

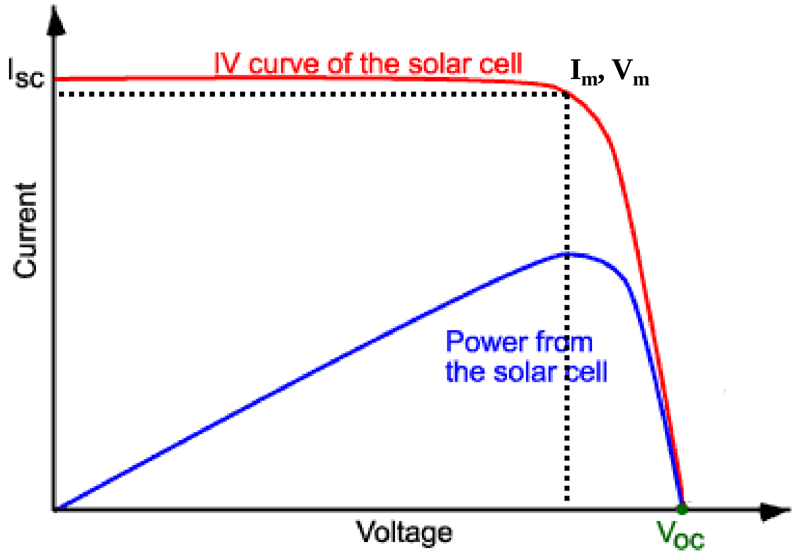

Figure 1.4 I-V curve of a solar cell [18].

termed as maximum current (I_m) and voltage (V_m). The FF is defined as the ratio of the maximum power from the solar cell to the product of V_{oc} and I_{sc}. FF and hence P_{mpp} are both affected by parasitic resistive losses in the solar cell which directly affect the current and voltage generation in the cell.

4) **η**: Efficiency is the most important parameter when comparing the performance of solar cells to one another. It is defined as the ratio of energy output from the solar cell to input energy from the sun. The efficiency of a solar cell depends on the optical properties of the solar cell and components of the solar module, spectrum and intensity of the incident sunlight and temperature of the solar cell. Therefore, measurement conditions must be carefully controlled to compare the performance of one device to another.

The performance of solar cells and solar modules is governed by the above four listed parameters, but the output power and output voltage govern the performance of solar panels and solar module arrays.

1.3 Motivation: Optical Losses at the Air-Glass Interface

PV technology has shown a tremendous improvement over the years since the first efficient cell was developed at Bell Laboratories. However, the efficiency of solar cells has saturated over more recent years despite the best efforts of researchers and scientists.

The saturated efficiency of solar cells has been attributed to various electrical and optical losses at the device level. Figure 1.5 lists the possible losses that affect the operation of solar cells and solar modules (after solar cells are encapsulated).

The loss of low energy and high energy photons first occurs at the solar cell device level and front glass cover where most of the photons are reflected from the surface. Some of the incoming photons are also absorbed in the intermediate encapsulant EVA layer. The other losses highlighted in red occur in the solar cell device due to its material properties. The system losses usually

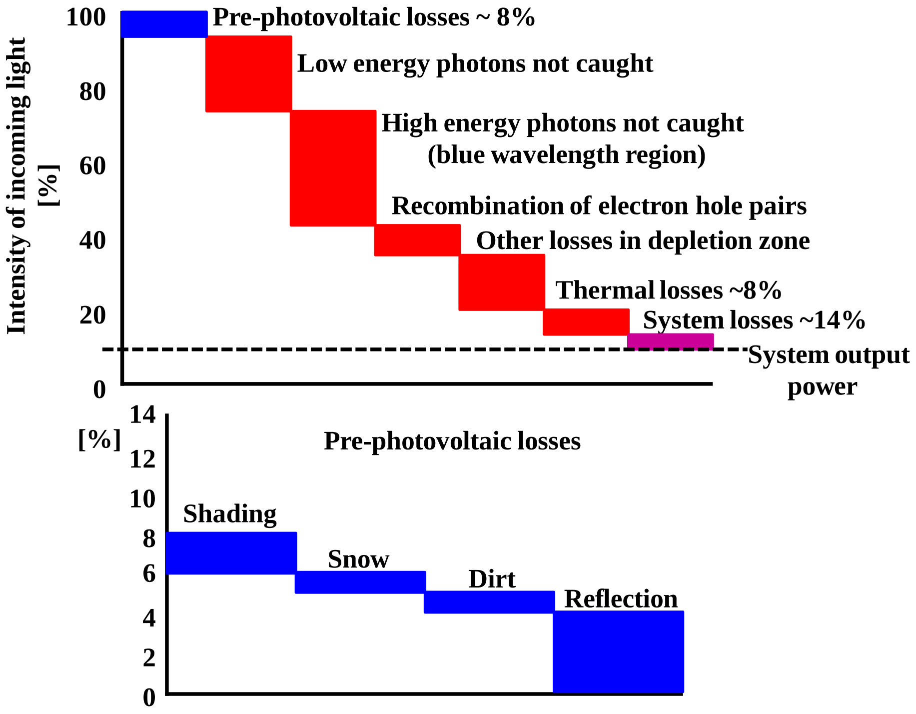

Figure 1.5 Optical losses in solar cells and solar modules [19].

occur when the solar modules are electrically connected and mounted in an array.

While much has been done to minimize electrical and optical losses at the solar cell device level, less attention has been paid to the optical losses occurring at solar module level especially at the air-glass interface. Such losses that occur at the front air-glass interface of front glass cover are called "pre-photovoltaic losses". The main causes of these pre-photovoltaic losses are reflection, accumulation of dust and snow, and shading.

A brief description of various PV pre-photovoltaic losses is given below:

1) **Reflection**: As seen in figure 1.2, a solar module consists of various components which can add to reflection losses. The losses mainly occur at the front glass cover and at the interface of the glass with the underlying solar cells. When light is incident on the solar module, there is an abrupt change in the refractive index from air to glass medium which causes the reflection of a part of the incident light. Moreover, the reflection increases when light traverses through the glass-Si interface which has a larger

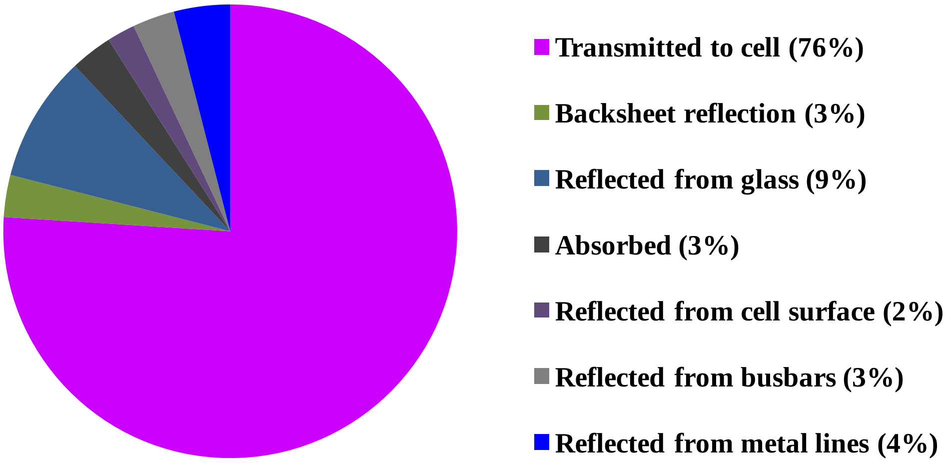

Figure 1.6 Reflection and transmission values at various components of a solar module.

difference in the refractive index. Figure 1.6 presents a summary of reflection losses at different components of a solar module (solar cell, backsheet, front glass cover, absorption by the encapsulant, electrical contacts on solar cell called busbars and silver metal lines on solar cells).

These reflection losses further increase with the angle of incidence of incoming light. It is essential for the solar panels to be normal to the incoming sunlight when placed outdoors to exhibit maximum performance. This condition is only satisfied when using solar panels with tracking systems. Tracking systems are automated mounting systems which constantly track the sun’s movement over an entire day. These tracking systems are fitted with a light sensitive device called a pyranometer which is designed to measure the solar radiation intensity from a field of view of 180°. The pyranometers help to align the solar panel tracking systems to the sun in maximizing their output performance. The tracking systems are effective to maximize the output performance of PV systems but add to the installation costs of PV systems. On the other hand, fixed mount PV systems suffer from angular reflection losses due to a change in the sun’s position over a day. This concept is described pictorially in figure 1.7 below.

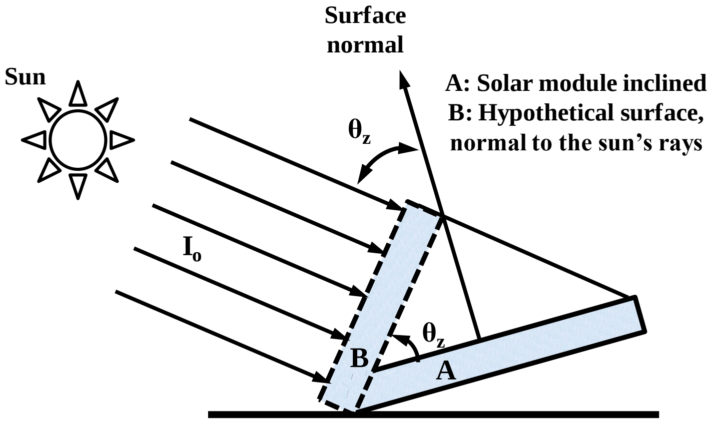

Figure 1.7 Illustration to explain the cosine effect in solar modules [20, 21].

Consider a fixed mount solar panel placed on the ground at a certain angle depending on the latitude position of the location. When this surface is normal to the incident radiation, the solar irradiance falling on it termed as I_o will be maximum, in figure 1.7. If the surface of the solar panel is not normal to the sun, the solar irradiance falling on it will be reduced by a factor of the cosine of the angle between the surface normal and the ray from the sun. As can be seen in figure 1.7, the rate of solar energy falling on both surfaces A and B is the same; however, the rate of solar energy per unit area falling on surface A is less than that of surface B. The area of surface A towards the incident radiation is greater than that of surface B. Therefore, this reduction of radiation by the cosine of the angle in fixed mount PV systems due to the sun's movement is termed as the cosine effect.

The front glass cover suffers from transmission losses which worsen with an increase in the angle of incidence. This undermines the omnidirectional performance of solar panels when placed outdoors. The term omnidirectional refers to the output performance of solar panels at several of incident light.

2) Accumulation of dust and snow: Dust accumulation is detrimental to the performance and yield of PV modules when installed outdoors. The accumulation of dust on the surface of PV modules interferes with insolation, causing both attenuation and scattering of the incident light. The constitution, density and size distribution of the dust particles have a varied effect on the performance of PV modules [22]. Dust particles accumulate on the surface either due to gravity, electrostatic charge or environmental conditions such as wind or water droplets and their adherence is governed by electrostatic potential near the surface, surface energy effects and capillary effects [23, 24].

These factors usually depend on the location of the PV installation [25]. The dust accumulation is severe in arid regions such as deserts of Saudi Arabia and Kuwait as compared to tropical locations like Singapore. Since there is less rainfall in the desert regions, wind speeds govern the cleaning of dust particles from the surface of PV modules. Slow wind speeds increase the deposition of dust particles, whereas high wind speeds help to blow away the dust [26, 27].

However, in tropical regions, rainfall is the primary cleaning agent for PV modules. But water can also be harmful since it mixes with the accumulated dust to form grime which sticks to the surface of the glass cover, thus, reducing the module's output performance. It has been studied that the PV performance losses due to dust accumulation could reach 15% in dry areas [28]. The only present solution to overcome this problem is to periodically clean the modules with water. This solution tends to be expensive due to the cost of manual labour involved in the task and shortage of water in many dry areas. A study in Saudi Arabian deserts has shown a degradation of 7% per month in the efficiency of solar panels [29] if left uncleaned.

The accumulation of snow in cold regions also has a similar effect to that of dust accumulation. It has been observed that the accumulation of snow can lead to a power loss of 25% in solar panels tilted at 39° to the ground surface and 42% in flat oriented solar panels over a course of a seven month winter period [30]. Thus, it is essential to keep the solar panels clean for effective output performance over a long period of time.

3) Shading losses: Shading losses can come in many forms. They can be either seasonal, or for a few hours each day depending on sun and cloud movements. Shading losses usually occur when a part of the solar panel mounted outdoors gets shaded either by clouds, accumulation of dust or snow or solar panel orientation. This causes fluctuation in the output power of the PV system, thus delivering lower power or not operating at maximum power point. The shading losses can also lead to the formation of hot-spots in solar modules. The solar cells in solar modules are connected in series which forces all cells to operate at the same current. Whenever, a cell gets shaded in a solar module or a solar module gets shaded in an array, the shaded cell or module becomes reverse biased which leads to power dissipation and thus heating effect. This heating of the cell or module creates hot spots which affects the overall PV output performance. The problem of shading losses has been resolved by the use of bypass diodes connected to every solar module in a solar panel or a solar module array [31]. Bypass diodes are passive components used in the interconnection circuit in junction boxes of solar modules which avoid thermal overload and the formation of hot spots in solar modules when shaded.

The motivation behind this thesis is to develop a solution to minimize the reflection and cleaning issues at the front glass cover, especially at the air-glass interface. This is done by creating a morphological change on the surface of front glass cover which imparts both antireflective and self-cleaning properties to the glass cover.

1.4 Research Objectives

The research objectives of this thesis are as follows:

a) The first step towards realizing antireflection structures for an optical material is to determine the feature size of the antireflection structures. Therefore, in this thesis, finite difference time domain (FDTD) simulations were carried out to design sub-wavelength structures for planar glass to study the increase in the spectral transmission of glass at normal incidence and oblique angles of incidence.

b) The thin-film coatings developed to minimize reflections on glass are limited in performance due to delamination and lifetime issues. Therefore, nanostructured surfaces were developed in the past. However, the literature lacks studies regarding performance of these nanostructured surfaces at oblique angles of incidence. In this thesis, a non-lithographic method has been developed to realize nanostructured features on glass substrates. Subsequently, a study is presented to gain an understanding of the omnidirectional properties of nanostructured glass. Mini solar modules (of area 39.75 cm^2) using multicrystalline Si solar cells have also been fabricated with nanostructured glass as their packaging covers and their performance has been evaluated by I-V measurements at different angles of incidence of light.

c) Durability and outdoor performance are key requirements for any nanostructured surface developed for glass covers of solar modules. In this thesis, an outdoor testing of 3 months has been carried out for the fabricated nanostructured glass substrates at different mounting inclinations of 0°, 10° and 20°. Solar modules fabricated for omnidirectional testing have also been tested outdoors for 5 weeks and their performance has been evaluated by I-V testing.

d) Nanostructure features also scatter the incident light. Scattering is advantageous in the case of thin film PV technology where the scattered light gets internally reflected at the glass-cell interface and helps to increase the I_{sc} and η of thin film solar cells. In this thesis, the scattering of nanostructured glass substrates has thus also been studied. A separate set of mini solar modules packaged with nanostructured glass substrates have been fabricated, where their quantum efficiency performance has also been evaluated.

1.5 Layout of Thesis

Chapter 1 discusses the present status of the PV industry and a forecast of installed capacity and solar module cost. A brief summary of different electrical and optical losses is also provided. The optical losses encountered at the air-glass interface of glass covers of solar modules provide the motivation and research objectives of the work in this thesis.

Chapter 2 gives a detailed overview about the naturally occurring species that have inspired the present state of the art antireflection and self-cleaning technologies. The principle and fabrication methods of antireflective and self-cleaning surfaces have also been discussed.

Chapter 3 introduces the experimental details and theoretical details of the FDTD simulation software used in this thesis.

Chapter 4 discusses the simulations carried out to study the performance of nanostructured glass samples. Their performance was compared to that of planar glass and thin film coating.

Chapter 5 discusses the fabrication method developed to create nanostructures on the glass surface. The optical performance of planar and nanostructured samples at normal and oblique angles of incidence is discussed. The nanostructured glass samples are used as packaging covers of solar modules. The performance of solar modules is evaluated for different angles of incidence of light.

Chapter 6 discusses the outdoor performance and durability of planar and nanostructured glass samples. The outdoor performance of solar modules with nanostructured glass samples as packaging covers is also evaluated.

Chapter 7 discusses the scattering properties of planar and nanostructured glass samples. The haze and angular scattering intensity of glass samples have been measured. External quantum efficiency (EQE) of the solar modules with planar and nanostructured glass samples as their packaging covers, was also measured to gain an understanding of their spectral performance.

Chapter 8 states the conclusions of the thesis and suggestions for the future work.

2. Antireflecting and Self-Cleaning Surfaces

2.1 Biomimetics: Inspiration from Nature

> "Biomimetics is the extraction of good design from nature"
>
> Prof. Andrew R. Parker [32]

Nature has been an inspiration to the human race throughout history [33], providing solutions to many problems in various fields [34-38] such as material science, mechanics, medicine, flight engineering, and architecture. A few incredible examples inspired by nature, that can be cited are buildings (similar to termite dens) [39], Velcro (similar to hooks of burrs) [39], jets/airplanes (similar to the V-shaped body of birds while in flight) [39], swimsuits (similar to shark skin) [39], and waterproof paints (similar to lotus leaves) [40]. Nature also has a self-healing ability as well as the ability to adapt to its surroundings whenever it encounters any difficulty.

Biomimetics can be defined as the transfer of a convincing design in nature to engineering applications. The term "biomimetic" was first given by Otto Schmitt in 1957 [41]. The field of biomimetics is a result of multiple "trials and errors" in nature which have resulted in a vast database of optimized structures that allow scientists to study them and cast applications for efficient use. Such biological features have been refined over a million years of adaptation. Their study has become a scientific discipline since the 1960s [42], where researchers and scientists have adopted these structures for commercial applications. One such renowned project [43] is being conducted at the Technical University of Denmark where researchers have provided resources and libraries of naturally occurring structures, and scientific methodologies for the study of biomimetics. In one recent discovery in the field of biomimetics at the University of Cambridge, scientists found a set of gears in the hind legs of the flightless planthopper [44]. Nature has provided numerous wonderful and clever solutions for mankind.

PV technology has also taken inspiration from nature [45]. Scientists have replicated naturally occurring textured surfaces on the surface of Si wafers for fabricating solar cells as well as front glass covers of solar modules for antireflection and self-cleaning applications. The following sections summarize the naturally occurring species, both flora and fauna, which have inspired the PV field.

2.1.1 Biomimetics for Antireflection Effect

Nature has provided a superior solution to solve reflection problems encountered by optoelectronic devices. The discovery of antireflective structures in nature took place while studying the compound eyes of insects, especially the moth-eye [46]. These studies opened up new avenues of research using sub-wavelength structures in optoelectronic devices and as a potential driving mechanism to minimize reflection losses in engineered structures. This section focuses on moth-eye structures.

Moth-eye structures were first examined by Bernhard, Miller and Moller [47, 48] in their studies of the corneal surface of the eyes of moths. The special features on the cornea of moth-eyes allow a moth to see clearly at night without producing back-reflections of incident light. This allows it to

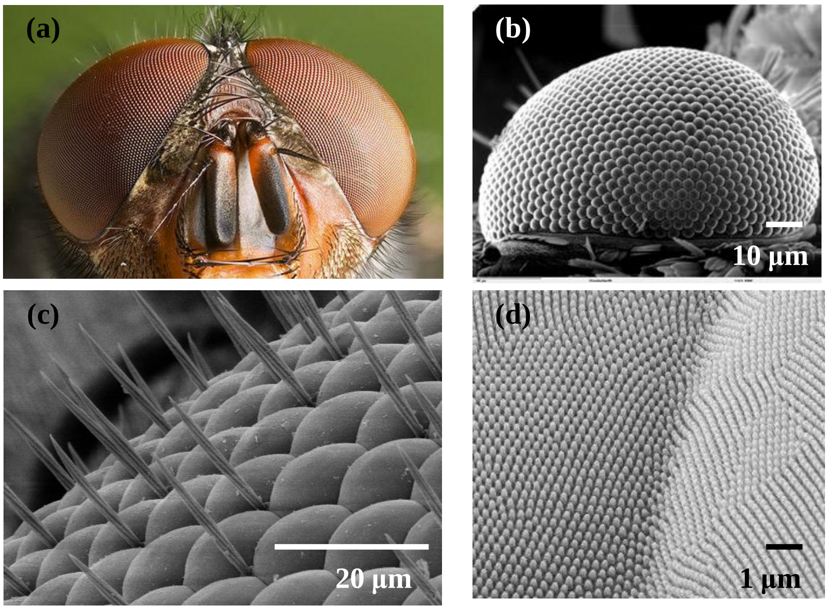

Figure 2.1 (a) Macroscopic image of a moth [49], (b) Scanning electron micrograph of the cornea of a moth-eye [50], (c) Scanning electron micrograph of ommaditia on a moth-eye [51], (d) Scanning electron micrograph of a nipple-array on the cornea of a moth-eye [52].

overcome the shining of its own eyes in the dark and hiding its location from its predators [47, 48].

An electron microscopy image as seen in figure 2.1 of the cornea of a moth insect revealed that the eye surfaces consist of numerous radial elements called ommaditia with a diameter of 15-40 µm. Each radial unit was also covered with a large number of minute protruding features, which were small enough to be seen only with an electron microscope. The protuberances observed were nearly conical in shape with feature sizes of ~200-nm in height and pitches of ~200-nm arranged in a hexagonal lattice. Bernhard and his colleagues termed these minute features as “nipples” and the whole surface as a “nipple array” [47]. These features can also be called “sub-wavelength features” in general, since their feature sizes are less than wavelengths in the visible regime.

Bernhard and his colleagues also studied the optical properties of the nipple array, primarily by two methods: transmission and reflection measurements using a microwave model and spectrophotometer measurements [47, 48]. A replica of the moth-eye features was created to be used at microwave wavelengths due to unavailability of nanoscale fabrication techniques at that time. The experimental measurements of these microscale features gave a clear indication that the protuberances helped to increase the transmission of incident light through the surface and decrease surface reflections. A comparison of these results to the actual dimensions of the nipple array showed that the nipples also increase transmission and reduce reflections in the visible regime. Further, the sub-wavelength features of moth-eyes were compared to the smooth surfaced cornea of a grasshopper by conducting spectrophotometric measurements. The results obtained from the measurements were in agreement with the increase in transmission observed with the microscale features. The microscope images of the nipple array were also used to study the functionality of the surface. Images of the moth-eye cornea appeared to be darker than the smooth surfaced cornea of the grasshopper, which is a confirmation of low reflections from sub-wavelength features.

Structures similar to nipple arrays have also been observed on the wings of a hawk moth (scientific name: Cephonodes Hylas) as seen in figure 2.2. These structures make their wings transparent to the eyes of predators. The microscope images reported by Yoshida et al. [54, 55], showed that these nipple like features were ~250-nm in height and had a pitch of ~200-nm. Spectrophotometric measurements of the hawk moth wings showed reflection less than 2% over a spectral wavelength range of 200-800 nm. Although features identical to nipple array were observed in many insect species, they are all generally referred to by the name “moth-eye” since it was first investigated on the cornea of the moth.

Another antireflective structure similar to the moth-eye structure was found by Andrew Parker et al., who termed it as a fly eye grating [57] seen in figure 2.3. The unique feature about this surface was that the ommaditia of the insect was curved with slanted ridges which resulted in angle independent reflection. A number of other species of insects have also been found with a combination of nipple arrays and slanted ridges. The same features that moth insects have, have also been seen on the wings of butterflies. These are usually

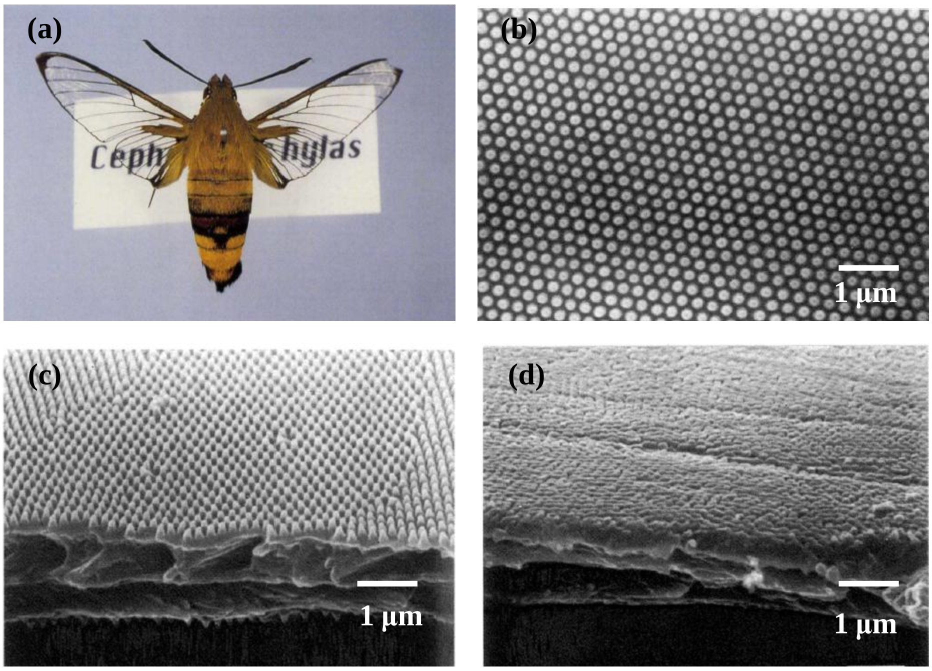

Figure 2.2 (a) Macroscopic image of a hawk moth showing its transparent wings, (b) Scanning electron micrograph of the top-view of the wing of a hawk moth, (c) Scanning electron micrograph of sub-wavelength features on the wings of a hawk moth, (d) Zoomed out scanning electron micrograph of a hawk moth wing [53].

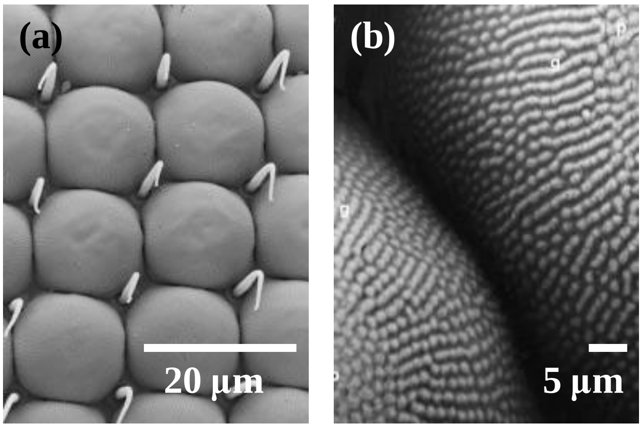

Figure 2.3 (a) Scanning electron micrograph of ommaditia of the fly eye, (b) Zoomed in scanning electron micrograph of ommaditia of the fly eye [56].

the black regions on the wings of butterflies which look distinctive among the striking colours on the wings. These highly absorbing structures have complicated three dimensional features on top and a non-reflective layer underneath to prevent backscattering at lower parts of the wing to interfere with the “ultra-black” [47, 58, 59].

Other than the field of optoelectronics, antireflective structures have found application in a wide range of defence and commercial applications [60-67], such as gemstones, stealth applications from infrared to radio frequencies, fade-resistant paints, electronic paper and high contrast ultra-black displays.

2.1.2 Biomimetics for Self-Cleaning Effect

One of the factors which affect the performance of solar modules when installed outdoors is the accumulation of dust particles. Nature has provided a solution to this problem as well, in the form of a wide variety of surfaces and morphologies in its flora and fauna exhibiting multifunctional properties. These have inspired scientists and researchers to develop various self-cleaning coatings and surfaces for a variety of applications in agriculture, military and industry. The terms superhydrophobic, superhydrophilic, hydrophobic and hydrophilic, and contact angle (θ_c) used in this section will be explained in detail later in this chapter.

The first structure which inspired scientists to study self-cleaning surfaces is the outermost layer of a plant surface called a “cuticle” [68-70]. The cuticle provides hydrophobicity to the plant surface which enables it to overcome the physical problems associated with the environment around it. The cuticle is basically made of a naturally occurring polymer material called cutin and integrated lipids called “waxes” superimposed on the cutin. Besides planar surfaces such as cutin, a wide variety of surface structures [68] have been discovered in plants, which help them to modify their surface wettability and which also have a significant influence on particle adhesion.

One of the first optimized non-wettable surfaces was found on the leaves of the lotus plant (Nelumbo nucifera). The surface of the lotus leaf exhibits superhydrophobic ($\theta_c > 150°$) and self-cleaning properties due to hierarchical roughness (microbumps superimposed with nanostructures) with a hydrophobic ($\theta_c > 90°$) coating [68-70, 74-77] as seen in figure 2.4. The papillose epidermal cells from the papillae provide roughness to the leaf surface on the microscale. The leaf surface is also covered with innumerable nanostructured wax asperities, formed from a mixture of long chain hydrocarbon compounds that provide the hydrophobic property. The superimposition of wax like structures on the epidermal cells gives rise to a hierarchical structure, thus a superhydrophobic property. Similar structures are also found on the surface of the taro leaf (Colocasia esculenta) with the wax

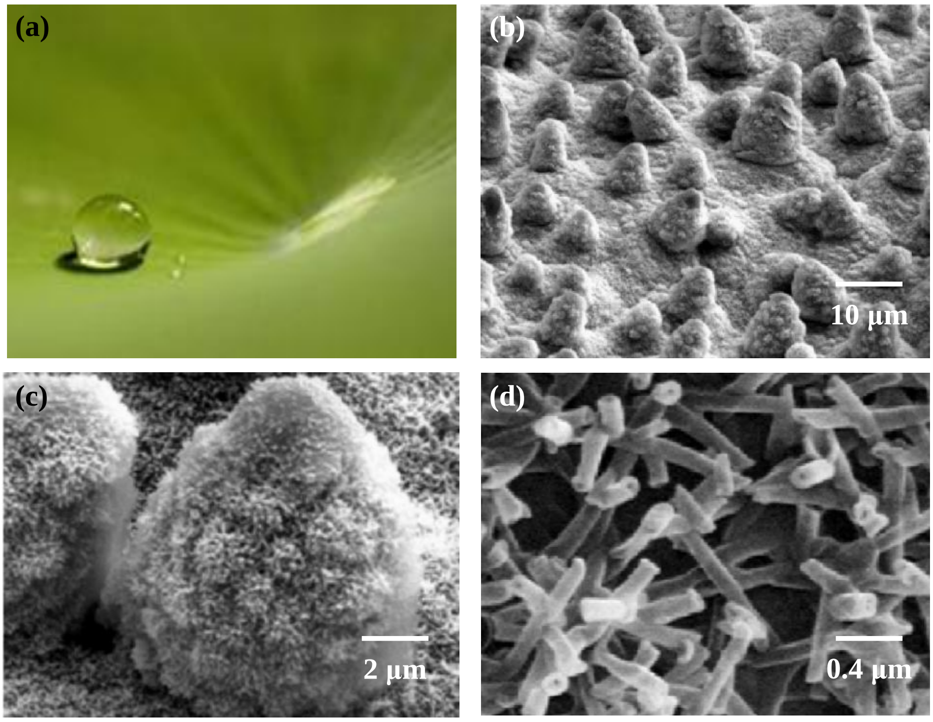

Figure 2.4 (a) Macroscopic image of a lotus leaf with a water droplet on its surface [71], (b) Scanning electron micrograph of surface of a lotus leaf [72], (c) Scanning electron micrograph of microstructure formed by papillose epidermal cells [73], (d) Scanning electron micrograph of epicuticular wax tubules on the surface of a lotus leaf which form nanostructures [73].

asperities having a platelet like morphology unlike the tubular morphology found on the lotus leaf [68-70].

The principle behind their superhydrophobic behavior is that water droplets sit at the apexes of the nanostructures because air bubbles fill the valleys of the structure under the droplet. This is due to the Cassie-Baxter effect which will be explained in subsequent sections. Due to this phenomenon, water droplets on the leaves remove any contaminant particles from their surfaces when they roll off, leading to self-cleaning. Another example of superhydrophobic water leaves is found in floating water ferns [69]. The water fern leaves have different lengths of water-repellent hair on their surfaces which vary on the order of several hundreds of micrometers. These multicellular hairs exhibit a similar hierarchical structure to those of the lotus leaf and impart a self-cleaning behaviour to water ferns.

Such surfaces are of interest and have been utilized for various applications such as self-cleaning windows, windshields, and exterior paints for buildings, boats, ships, aircrafts and solar modules. Such surfaces can also reduce stiction in machinery [78, 79].

Hydrophilic ($\theta_c < 90°$) or superhydrophilic ($\theta_c < 10°$) plant leaves [68-70] have also been reported. Such leaves either absorb water or let water spread on their surface. Examples of such leaves are spanish moss (Tillandsia usneoides) and sphagnum moss.

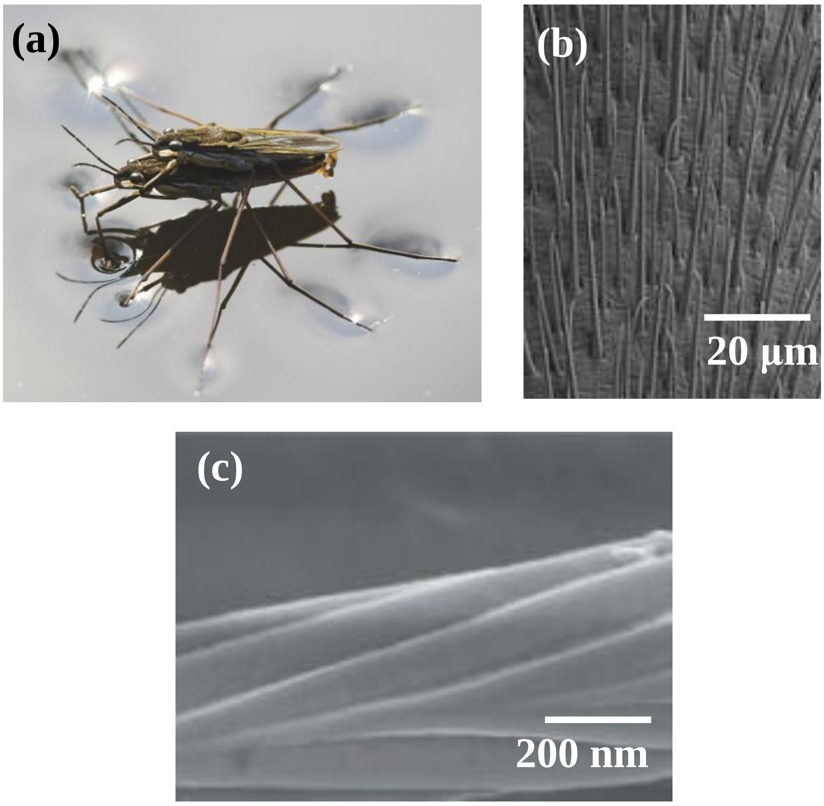

Figure 2.5 (a) Macroscopic image of the pond skater [80], (b) Scanning electron micrograph of a pond skater showing numerous oriented microscale setae [81], (c) Scanning electron micrograph of the nanoscale grooved structures on a seta [82].

The superhydrophobic property has also been discovered and studied on the legs of pond skaters (Gerris remigis) which are insects living on the surfaces of ponds, slow streams and quiet waters. The pond skater has the ability to stand and walk on the water surface without submerging itself into the water [83]. It was shown that the pond skater's legs are comprised of special hierarchical structures (figure 2.5) covered with large number of oriented tiny hair called microsetae with fine nanogrooves and covered with cuticle wax which imparts superhydrophobicity to the legs. The features found on the legs of pond skaters have also been replicated to form self-cleaning nanostructured surfaces [84].

2.2 Antireflective Surfaces: Principle and Fabrication Techniques

According to Fresnel's law of reflection, when a beam of light strikes an optical material like glass, a part of the incident light is transmitted through the material, some part is reflected at the interaction interface and the rest is absorbed in the material itself. This phenomenon has been pictorially shown in figure 2.6.

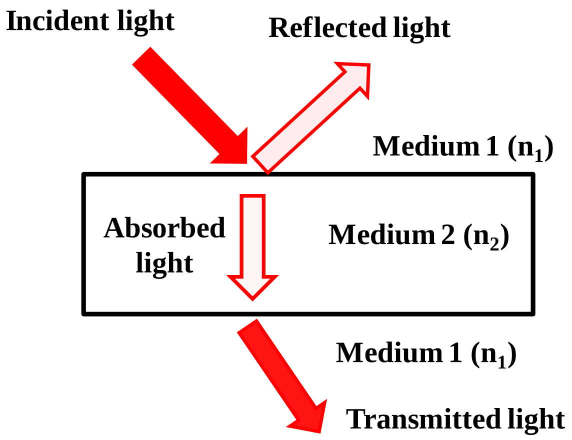

Figure 2.6 Interaction of incident light with a material substrate.

The interaction of light with the optical material is a function of the refractive index of the optical material and the medium surrounding the material. The relationship between reflection and refractive index of the two media (surrounding medium and optical material) is given by the following equation based on the Fresnel equations [85]

$$\boldsymbol{R = \frac{n_1 cos\theta_1 - n_2 cos\theta_2}{n_1 cos\theta_1 + n_2 cos\theta_2}} \qquad \text{Equation 2.1}$$

where R is the reflectance, n_1 and n_2 are the refractive indices of the surrounding medium and optical material respectively and θ_1 and θ_2 are the angles of incidence and refraction respectively.

At normal incidence ($\theta_1 = \theta_2 = 0°$), the reflection between the two media is only dependent on the difference between the refractive indices of the media. However, the problem of reflection increases at oblique angles of index where the $cos\ \theta$ term plays a deciding role. In practical situations, this is known as the cosine effect which has been explained in Chapter 1.

Although reflection is desirable for the operation of many optical and optoelectronic devices and technologies, reflections are generally unwanted in applications where transmission of light plays a major role. Si solar cell technology is identified as one of the main energy harvesting technologies [86] where reflection hampers the operation of the device. However, the reflection of light plays a key role in generating output power in concentrated photovoltaics where a large amount of light is reflected from lenses and mirrors to a small solar cell device [87]. The output power of Si solar modules is far from being close to their expected theoretical maximum. Reflections at various components of the solar module enlisted in chapter 1 undermine the efficiency of solar modules when installed outdoors. Scientists and researchers have developed a wide variety of coatings and surfaces to minimize this problem for the glass-Si interface but less attention has been paid to the critical air-glass interface. Thus, it is of great importance to develop antireflective coatings and structures for the air-glass interface.

This section of the chapter provides an overview of antireflective technologies. They are generally based on two mechanisms – destructive interference or gradual change of refractive index. For this purpose, three technologies are under development, namely, **thin film coatings** (single, and multi-layer thin film antireflective coatings), and **porous coatings** and **sub-wavelength antireflective structures**. These three groups are reviewed in the following section:

2.2.1 Thin Film Coatings (Single Layer and Multi-layer Coatings)

As discussed before, the transmission loss at the air-glass interface is due to the abrupt change in refractive index when light travels from air into glass. Therefore, one of the prime technologies suggested in early 19th century to minimize reflection losses was thin film antireflection coatings. The first proposer of thin film coatings was Fraunhofer in 1817 when he noticed that the reflection of incident light was reduced at an etched surface in an atmosphere of sulphuric and nitric acid (HNO_3) vapours [88]. However, the mathematical concept was not explained until 1880, by Lord Rayleigh, who recognized the potential of gradual transition layers (which we now refer to as graded index layers) as antireflection coatings.

The operating principle of thin film antireflection coatings is based on destructive interference. When there is an interaction between two light waves

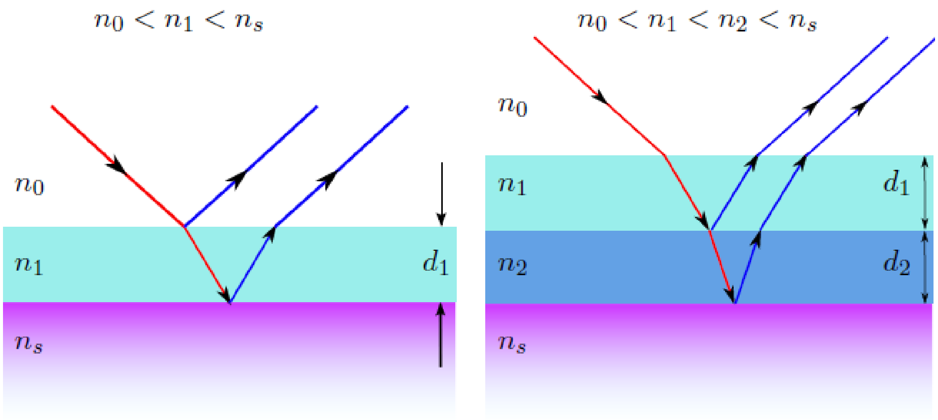

Figure 2.7 Destructive interference using (a) a thin film single layer, (b) a double layer.

with a phase difference of π, the waves interfere destructively. If the amplitude of the two incident waves is equal, the net amplitude would be zero. In this manner, the reflectance of the incident light can be lowered or even reduced to zero using destructive interference.

The reflection loss at an interface can be minimized by employing a thin layer of material having a refractive index value between those of the two surrounding media. Figure 2.7 shows the possible configurations.

When light is incident from a medium of refractive index n_0 on another medium n_s with an intermediate thin antireflective layer of refractive index n_{layer}, two interfaces are created. Consequently, reflection occurs at both interfaces. The path length difference between the two reflected rays, which is dependent on the thickness of the intermediate layer, causes a phase difference which results in constructive or destructive interference. If the intermediate layer has a thickness of a quarter of the wavelength of the incident light, the path difference produces a π phase difference which results in destructive interference. Consequently, it leads to zero reflectance at this particular incident wavelength and lower reflectance at nearby wavelengths.

This technique was primarily used for solar cell antireflective coatings in the photovoltaic industry where silicon nitride (Si_3N_4) was chosen to be an effective candidate [89, 90]. Later, the same idea was also applied in reducing reflections at the air-glass interface. A single layer with an optical thickness equal to a quarter of the wavelength with refractive index $n_{layer} = \sqrt{n_0 n_s}$ can be used as an antireflection coating. For the air-glass interface, n_0 is the refractive index of air which is equal to 1, and n_s is the refractive index of glass which is ~1.52. Therefore, a thin film of quarter wavelength thickness required for reducing reflections on glass should have n_{layer} of ~1.22. However, materials with $n_{layer} \leq 1.22$ are rarely available, so materials with refractive index near the required value can be used for this purpose. Typical single layer coating materials used at the air-glass interface are magnesium fluoride (MgF_2) [91, 92], titanium dioxide (TiO_2) [93-95], silicon dioxide (SiO_2) [96-98], aluminium oxide (Al_2O_3) [99] and cerium oxide [100]. Multi-layer coatings were also employed as intermediate layers of different refractive indices and thicknesses. The main aim of using multi-layer structures is to improve the antireflection property over a broader wavelength range and wider range of incidence angles. The net thickness of multi-layer structures is also quarter of a wavelength and for example, refractive index of a dual-layer system can be calculated using $\boldsymbol{n_1^3 = n_0^2 n_s}$ and $\boldsymbol{n_2^3 = n_0 n_s^2}$.

A study [101] has been presented to explain the difference between the performance of single and multi-layer coatings to minimize reflections on a glass substrate. In this work, a combination of air/MgF_2/glass (single layer), air/MgF_2/Al_2O_3/glass (dual layer), and air/MgF_2/ZrO_2/CeF_3/glass (multi-layer) has been used to explain the practical effect of different thin film layer

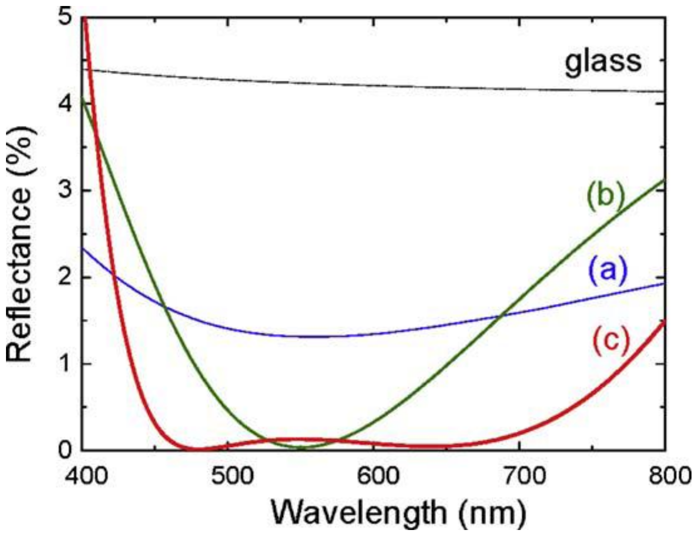

Figure 2.8 Reflectance vs. Wavelength for antireflection coatings: (a) single layer antireflection coating: Air/MgF_2/Glass; (b) dual-layer antireflection coating: Air/MgF_2/Al_2O_3/Glass; (c) three-layer antireflection coating Air/MgF_2/ZrO_2/CeF_3/Glass [101].

systems on antireflection properties. ZrO_2 and CeF_3 are zirconium oxide and cerium fluoride respectively.

As shown in figure 2.8, a single layer coating of MgF_2 reduces the reflection at air-glass interface from ~4.5% to ~1.5%. But, it is observed that the effective reflectance of a dual layer coating decrease significantly approaching zero at a wavelength of 550 nm. It is accomplished by coating a high index material between the low index coating and the glass substrate, providing an effective antireflection effect. On the other hand, the multilayer system provides a lower reflectance over a broader range of wavelengths as shown in figure 2.8(c).

These thin film coatings are generally prepared using physical vapor deposition methods such as magnetron sputtering [102-105], electron beam evaporation [106, 107], or chemical methods such as chemical vapor deposition (CVD) [108-110], sol-gel processing [111-113] and dip-coating [114-116]. While the fabrication processes might not be complicated, there is a limitation on the materials which can be used to provide the required refractive index. The problem becomes profound for the case of multi-layer coatings which are limited by the optimum refractive index, deposition method, uniformity, and thickness and properties of the coatings. These thin film coatings also suffer from problems of weak adhesion and delamination.

2.2.2 Porous Antireflective Coatings

The inability of thin film coatings to provide antireflective properties over a broadband wavelength range led to research on porous structures. These particular coatings are prepared by tuning film topography and structure. The concept behind porous antireflective coatings is that nanometer sized voids of air present between the parent particles can provide a smooth variation in the refractive index. The only requirement for these structures is that homogeneity in pore sizes must be maintained and the size of the parent particles should be smaller than the wavelengths of light in order to avoid scattering. The parent particles of these coatings often look similar to the patterns seen on the cornea of moth-eyes. The relationship between refractive index and porosity [117] is proposed differently in different studies, for example,

$$\boldsymbol{n_{pc} = \left[\left(1 - \frac{P}{100}\right)\left(n_{dc}^2 - 1\right) + 1\right]^{\frac{1}{2}}} \qquad \text{Equation 2.2}$$

where n_{pc}, n_{dc} and P are the refractive index of the porous and dense media, and the porosity percentage respectively. The refractive index of porous structures follows effective medium theory (EMT) [118]. The nanostructures or sub-wavelength structures decrease the effective discontinuity between the two surfaces (of different refractive indices) by making themselves blurred to the incident light. The nanostructured surfaces possess a refractive index that gradually increases from the low refractive index medium to the high refractive index medium. It can be viewed as a composite of a large number of very thin layers, with each layer having a different refractive index increasing from top of the nanostructure to the bottom. Hence, as the light passes through these layers, less reflection takes place, thus providing an antireflective effect.

The first nanoporous films were developed by Fraunhofer in 1819 [119] through wet etching of planar glass. The modern approach to create such structures or coatings is usually done by sol-gel processing, where spin-coating [120-122], dip-coating [123-126] or spray coating [127-129] processes are used to form a layer of the coating on the surface. Typical sol-gel process is shown below in figure 2.9 to fabricate porous antireflective coatings.

Sol-gel processing is a common method in the production of porous antireflection coatings. This process usually involves the use of inorganic salts or metal alkoxides as precursors which when exposed to an aqueous or organic solvent, hydrolyze and condense to form an inorganic polymer comprising of metal-oxide-metal bonds. The porosity, and hence, reflectance of the developed coatings depends on the solution composition, porous film growth rate and film thickness. Industrially, the sol-gel method has been used since 1964 [131] to create porous antireflection coatings. Studies have shown that the optimization of pore size and pore volume depends on the mixing volume of the materials to create a porous coating mixture [132].

For PV applications, numerous materials have been used. For instance, a mixture of polystyrene (PS) and polymethyl-methacrylate (PMMA) in the

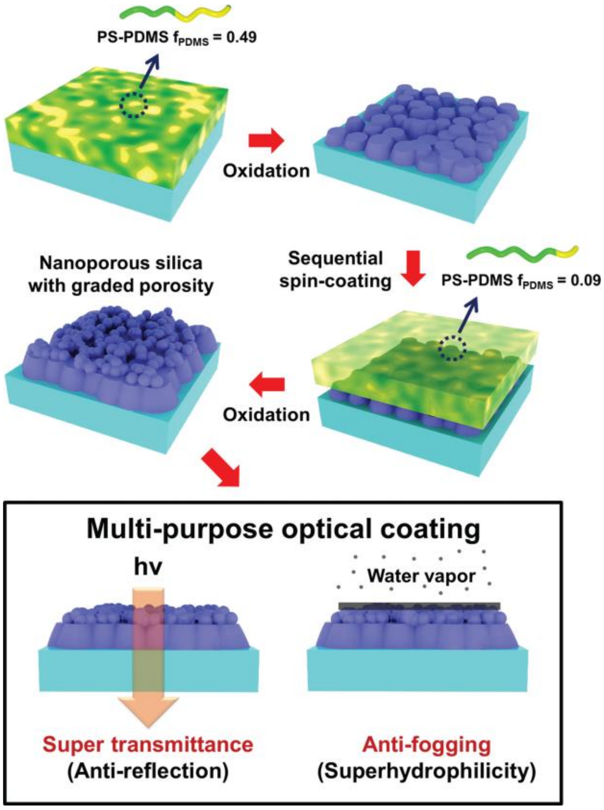

Figure 2.9 Schematic of a sol-gel process [130].

solvent tetrahydrofuran, followed by spin coating on glass and subsequent treatment with cyclohexane to dissolve PS, has been used to create porous PMMA coatings [133]. Other materials used for such purpose are SiO_2 [134], TiO_2 [135], mixture of SiO_2-TiO_2 [136], MgF_2 [137] and Al_2O_3 [138].

Sol-gel technology is a cost-effective technology in PV industry. But, it still has limitations. Sol-gel prepared films often contain unreacted solvent materials which might affect antireflection. In addition, polymer materials employed for this technique are limited by their functionality outdoors since they are prone to wear and tear by dust particles and ultraviolet (UV) discoloration which might also affect transmission. It is also difficult to control the thickness of the porous coatings in fabrication.

2.2.3 Sub-wavelength Antireflective Nanostructures

The unreliable performance of thin film single and multi-layer coatings over a broadband wavelength range led to the investigation of surfaces with a gradient refractive index to achieve superior antireflective performance. Nature has provided a fantastic example of the moth eye which led to the concept of the moth-eye effect. The nanostructures provided an immense improvement since their dimensions were less than the incident wavelength. That is why they are also known as sub-wavelength structures.

Similar to nanoporous structures, sub-wavelength structures also exhibit a gradual change in the refractive index. When light interacts with structures of dimensions smaller than its wavelength, it behaves as if it is encountering a homogeneous medium with no sudden change in the refractive index, so as not to cause the incident light to be reflected. A pictorial representation of a sub-wavelength structure profile can be seen in figure 2.10(b).

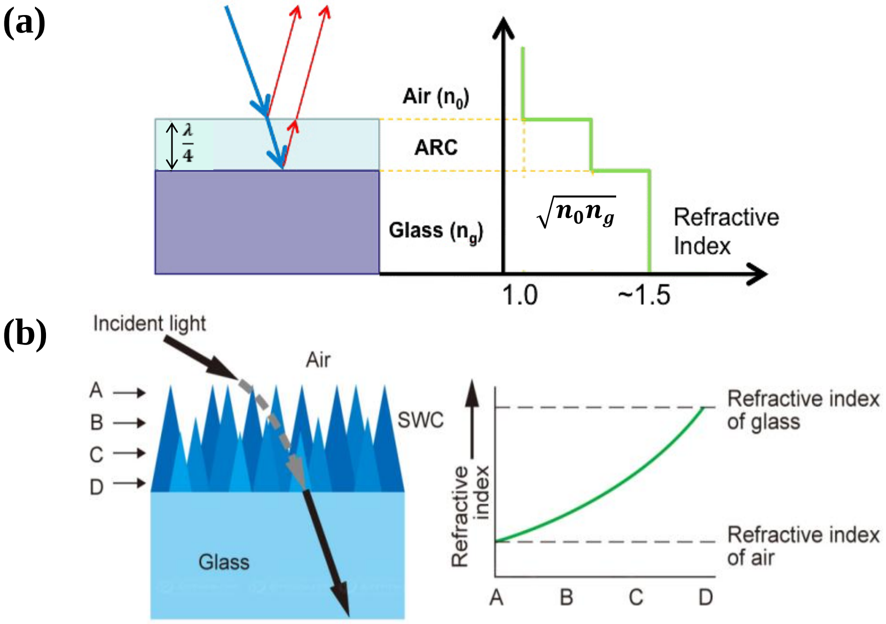

Figure 2.10 (a) Refractive index profile for a thin film dielectric antireflection coating, (b) Refractive index profile for sub-wavelength structures on glass [139].

The sub-wavelength structure behaves as an infinite stack of infinitesimally thin layers, introducing a gradual change in the refractive index from one medium to another. This effectively smoothens the transition between one medium to another for the incident light as stated before. This concept can also be understood in a different manner where these infinitesimally thin layers cause destructive interference between reflections from each layer. This cancels all the reflected light, hence, maximizing the proportion of the transmitted light.

As mentioned before, the sub-wavelength structures can be considered as a stack of many layers, each with an effective refractive index in between those of the media and interface. This forms the basis of EMT. For EMT to apply to sub-wavelength structures, the features at the interface must be sufficiently small so that they cannot be resolved by the incident light. This means that the features should not be large enough to scatter light, when fabricated as periodic or randomly arranged features.

To analyze the underlying physics behind the antireflection effect of sub-wavelength features, they can be treated as a diffraction grating in 2D, with a period small enough to suppress all diffraction orders other than the zeroth

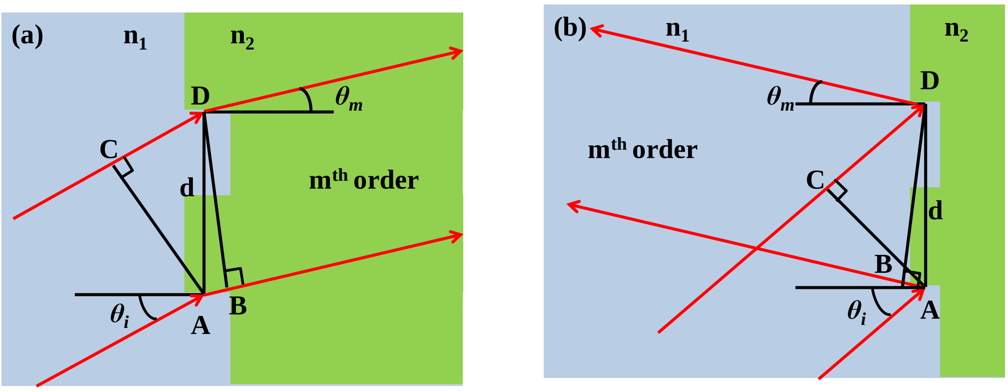

Figure 2.11 Schematic to derive the grating equation for (a) transmission, and (b) reflection.

order. The grating equation can be used to determine the period d for zero order grating. This is derived by equating the path-length difference of two rays incident on adjacent features with an integer number of wavelengths such that they interfere constructively. In transmission, this is given by

$$\boldsymbol{n_2AB - n_1CD = m\lambda} \qquad \text{Equation 2.3}$$

$$\boldsymbol{n_2 \sin\theta_m - n_1 \sin\theta_i = \frac{m\lambda}{d}} \qquad \text{Equation 2.4}$$

where m is an integer order number, λ is the wavelength, θ_i is the angle of incidence and θ_m is the outgoing propagation angle of order m. In reflection, the light is travelling in the same medium, so the grating equation becomes

$$\boldsymbol{\sin\theta_m - \sin\theta_i = \frac{m\lambda}{n_1 d}} \qquad \text{Equation 2.5}$$

If the incident medium is air, then $n_1 = 1$. As d is decreased, the last order should disappear at $\theta_m = 90°$. At normal incidence, $\theta_i = 0°$, the last order to disappear is the first order, $m = 1$ (or $m = -1$). Therefore, the zero order grating condition is given as

$$\boldsymbol{d < \frac{\lambda}{n_2}} \qquad \text{Equation 2.6}$$

for the transmission grating and for reflection, it is given as

$$\boldsymbol{d < \lambda} \qquad \text{Equation 2.7}$$

Therefore, the conditions for d for both transmission and reflection should be satisfied to obtain a significant antireflection effect from sub-wavelength structures.

Fabrication processes that have been used to create sub-wavelength structures on surfaces are nano-imprint lithography [140-142], glancing angle deposition [143,144] and nanosphere lithography in combination with an etching process [145].

The first attempts to create sub-wavelength nanostructures on a glass surface were carried out by imprinting a moth-eye pattern directly on the substrate surface. This was usually done using techniques such as nanoimprint lithography. A schematic of the nanoimprint lithography process is shown in figure 2.12.

Nanoimprint lithography is one of the oldest techniques in the field of nanofabrication which developed from a manual stamping technique to a fully automated process. It serves as an alternative to expensive techniques such as electron beam lithography, which is a time consuming and an expensive technique. This technique usually is used to transfer the pattern on a stamp onto a substrate.

The process starts with the creation of a pattern on a stamp, which is generally made by electron beam lithography. With the correct pattern on the stamp, it can be used for several runs. The features casted on the stamp using electron beam lithography are usually smaller than 200 nm. For bigger features, optical interference lithography can be used. For nanoimprint lithography, the substrate is coated with a suitable thickness of polymer such as photoresist. The substrate is heated and then the stamp with the features is pressed onto the substrate with the correct amount of pressure. After cooling, the stamp is removed. The pattern obtained on the polymer coating is then

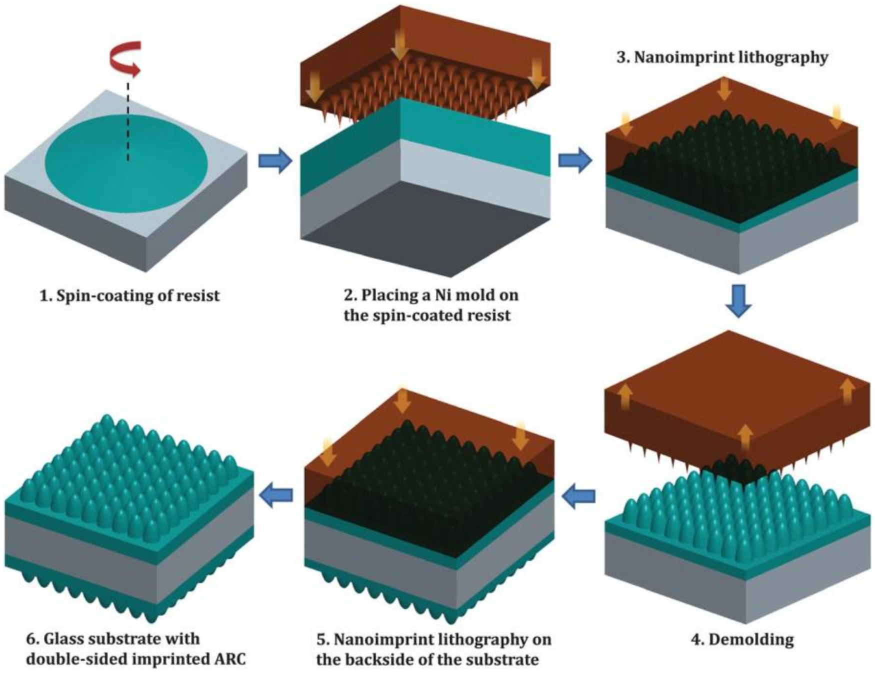

Figure 2.12 Schematic of nano-imprint lithography process where the patterns have been imprinted on both sides of the substrate [146].

transferred onto the substrate by dry or wet etching. The remaining polymer is then removed by chemical means. The minimum feature size that can be obtained by this technique depends on the feature size of the stamp.

In an attempt to make antireflective structures on glass, Raut et al. [146] fabricated methacryl polyhedral oligomeric silsesquioxane (POSS) nanostructures on glass. Initially POSS polymer was coated on glass and then a nickel (Ni) metal mold of size 3 cm × 2.5 cm with nanostructure features of dimensions 200 nm height and diameter 100 nm was used to imprint features on this coated polymer. These sub-wavelength features imprinted on POSS polymer increased the transmission of glass to 98.1% from 92% when imprinting was done on both sides of the glass surface as shown in figure 2.10. Omnidirectional improvement in optical transmission was noticed up to 40° of angle of incident light.

Si moth-eye structures were also fabricated by Yu et al. [147] by means of trilayer nano-imprint lithography and a lift-off. In their process, a Ni mask was used to imprint features of dimensions 200 nm period and 250 nm groove depth. Reactive ion etching was then used to transfer the imprinted pattern on the underlying Si substrate. The moth-eye features exhibited reflection less than 1% in the visible regime. Similarly, Boden et al. [187] also fabricated Si moth-eye structures with the same process. Similar processes have also been demonstrated on GaAs [188] and plastic substrates [189].

Numerous other works have also been reported to fabricate sub-wavelength structures on glass and Si [148-151].

Nano-imprint lithography is a versatile process providing the advantage of scalability along with small feature sizes comparable to features obtained by electron beam lithography. However, the first step of fabricating the master mold or stamp is a tricky process. This is a time consuming and an expensive process which adds to the cost of the final product. Additionally, the shape of features is still very poor, and remains dependent on the etching process.

The fabrication of moth-eye structures sometimes depends on the nature of the materials. Some of the factors that govern the fabrication processes are the thermal mismatch between the substrate and coating as well as the adhesion between the two. Nanosphere lithography offers a cheap method to transfer a pattern on a substrate. In this technique, the nanospheres are arranged on the substrate via a self-assembly process. Then, the feature size of nanospheres is tailored according to the desired feature size of the sub-wavelength structures for the particular substrate and then etching process is carried out to transfer the pattern on the substrate.

The schematic of a possible nanosphere lithography process is shown in figure 2.13.

Maier et al. [153] reported antireflection structures in glass fabricated using dual step fabrication process using SiO_2 nanoparticles as the first layer and SiO_2 thin layer to increase the adhesion between nanoparticles and glass. These nanoparticles were arranged by self-assembly or a colloidal lithography process where they served as a mask for the subsequent wet etching process to create nanostructures on a glass substrate. The authors have reported an enhancement of 1% in optical transmission.

Sun et al. [154] employed monolayer SiO_2 colloidal particles to etch Si and produce moth-eye structures. Spin coating was used to create a random arrangement of 360-nm SiO_2 spheres on Si. Sulphur hexafluoride (SF_6) dry etch was performed to etch the underlying Si substrate through the nanosphere mask. The etching time determined the height of the etched features. The remaining SiO_2 particles were removed by an hydrofluoric (HF) acid wash.

The pattern with a height of 800 nm showed a reflection less than 2.5% over a wavelength range of 400-800 nm. Similar work was also employed to create gallium antimonide moth-eye structures for thermophotovoltaic applications.

This technique has the advantage of being cost-effective and fast as compared to lithographic techniques such as electron beam lithography. This technique also allows large scale production. However, this technique is limited by the self-assembly process where it is hard to obtain a monolayer of particles as well as uniform coverage over the substrate surface. This

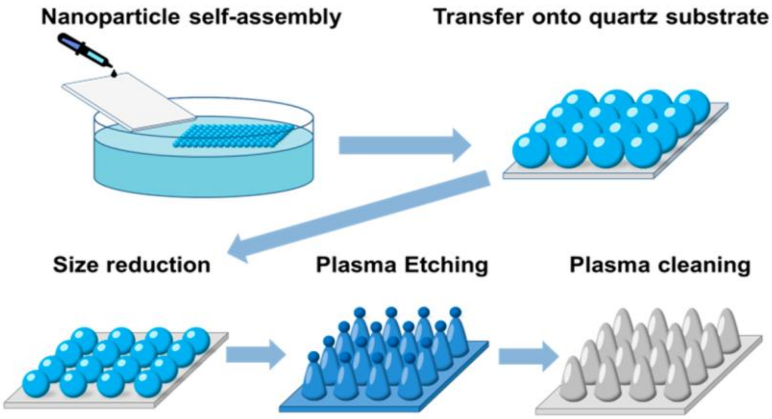

Figure 2.13 Schematic of a nanosphere lithography process [152].

technique is only capable of making hexagonal lattices of protuberances, while aperiodic structures are also attracting some research interest [155].

One of the other techniques which has gained interest in recent years is glancing angle deposition. The schematic of glancing angle deposition is shown in the figure 2.14.

Glancing angle deposition provides an advantage over nanosphere lithography where nanopatterns can be deposited on a substrate using physical vapor deposition tools such as electron beam evaporation and sputtering. Then, the substrate can be subjected to dry etching to fabricate the required size of nanostructures for antireflection applications.

The non-lithographic process to be (described in Chapter 3) used in this thesis is a comparable process to glancing angle deposition. Glancing angle deposition forms a nanostructure template using electron beam evaporation, whereas the thesis process forms nanostructure template by annealed thin metal film deposited on substrate with electron beam evaporation. In both these cases, the substrate is etched later using a dry etching process. Both

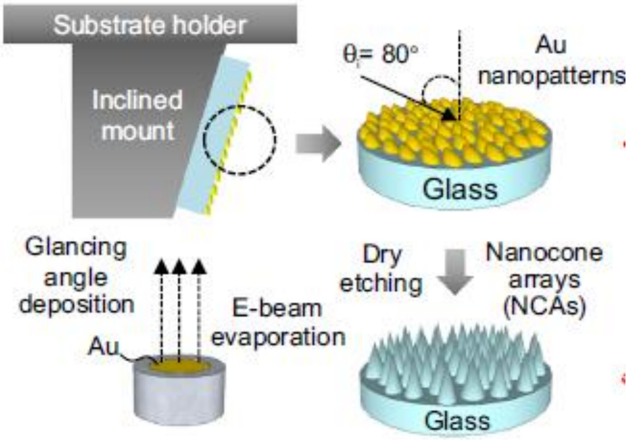

Figure 2.14 Schematic of a glancing angle deposition process [156].

processes provide an advantage of being scalable and less time consuming as compared to nanoimprint lithography.

2.3 Self-Cleaning Surfaces: Principle and Fabrication Techniques

The self-cleaning ability of some materials by simple action of rainfall might seem to be exclusive to modern science but this miracle already exists in nature and has evolved for various flora and fauna. Nature has inspired development of such surfaces for practical applications. Self-cleaning surfaces have become an important requirement for certain optoelectronic devices such as PV modules or panels and aesthetically for sky-scrapers and commercial facades.

Self-cleaning surfaces can be of different types, operating in different ways. The principle behind the self-cleaning property of a surface depends on its chemical and physical characteristics, material composition, and presence of an external stimuli or agent. However, all these surfaces have one common operating principle: water as an active agent for the cleaning process.

2.3.1 Wettability of Solid Surfaces

The interaction between a droplet of water and surface is determined by several factors and characteristics of both states of matter: physical chemistry (wettability), statical physics (pinning of the contact line, wetting transitions etc.), intermolecular and long-range forces (Van der Waals) and fluid dynamics. The liquid may be of different types – water, paint, lubricant, or a dye depending on applications where different liquids are interacting with solid surfaces. The solid surface might be a homogeneous or non-homogeneous surface (smooth, porous, micro-textured or fractal, for example glass).

Depending upon the properties of the liquid and the solid surface in contact, the liquid droplet may assume two different wetting equilibrium regimes: partial wetting or complete wetting. The parameter which indicates the surface property of the solid surface for a particular liquid droplet type is known as the contact angle (θ_c). θ_c is a quantitative measure of wetting of a solid or a liquid. It is defined geometrically as the angle formed by a liquid drop at the three phase boundary where a liquid, vapor and solid intersect each other.

In the case of partial wetting, the contact line between liquid and gas phases is a circle and the droplet has the shape of a spherical cap. In the complete wetting regime, the liquid flattens out homogeneously on a solid

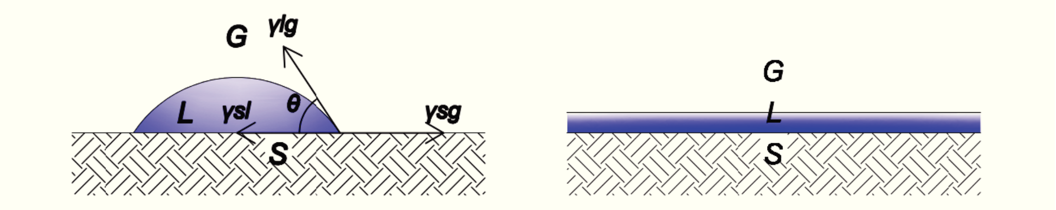

Figure 2.15 Liquid over solid surfaces: partial wetting and complete wetting [157].

surface. Thus, it forms a film over the surface and the thickness of the liquid film is the main determinant of its properties. The partial and complete wetting states are shown in figure 2.15.

On the basis of wetting behavior, four different wetting surfaces are defined:

1) Hydrophobic surfaces - Intrinsic θ_c is greater than 90°.
2) Superhydrophobic surfaces - Intrinsic θ_c is greater than 150°.
3) Hydrophilic surfaces - Intrinsic θ_c is smaller than 90°.
4) Superhydrophilic surfaces - Intrinsic θ_c is smaller than 10°.

There are three wetting models proposed which determine the wettability of a surface mathematically. These are **Young's model**, **Wenzel's model** and **the Cassie-Baxter model**.

An English polymath, Thomas Young was one of the first scientists to explain the wetting phenomena and formulated the law describing the partial wetting case [190]. Young determined the equilibrium shape of a liquid droplet on an ideal solid surface. In his theory, an ideal solid surface was considered to be flat, perfectly smooth, chemically homogeneous and having zero contact angle hysteresis. Young devised an equation which included the surface tensions (forces per unit length) acting at the three phase contact line of the drop in the plane of the solid. These forces upon interacting with each other determine the shape of the liquid droplet. The equation is given as

$$\boldsymbol{\gamma_{sg} = \gamma_{sl} + \gamma_{lg} cos\theta_c} \qquad \text{Equation 2.8}$$

where the symbol γ denotes the surface tensions between the three phases indicated by their subscripts (s - solid, g - gas/vapor, l - liquid). The equation provided by Young only governs cases for partial wetting. However, if the solid/gas interface has a very low surface energy, θ_c can be theoretically 180°, where the drop shape is a complete sphere, thus always keeping the surface dry. At the other extreme, if the sum of liquid/solid and liquid/gas surface tensions equals the solid/gas surface tension, θ_c becomes zero which means the water droplet flattens on the surface (high energy surface), thus giving a complete wetting state.

Young's model has its own limitations. This model has been considered for completely smooth surfaces. But smooth surfaces seldom exist practically, thus this model does not hold on experimental surfaces.

To explain the wettability of practical surfaces which have a characteristic surface roughness, the Wenzel and Cassie-Baxter models were proposed which provide information on partial or complete wetting of non-ideal rough surfaces.

Practical surfaces show very different properties as compared to the ideal surfaces for which Young's model was defined. Practical surfaces are rough, and physically and chemically inhomogeneous. The roughness of a surface determines the wettability. Wenzel and Cassie-Baxter models have been defined to provide expressions for apparent contact angles of liquids on homogeneous and heterogeneous surfaces, respectively. The equations defined by these models are valid when the size of the liquid droplet is greater than the surface roughness scale.

Robert N. Wenzel described the concept of homogeneous wetting surfaces and provided an expression for apparent contact angle between liquid and

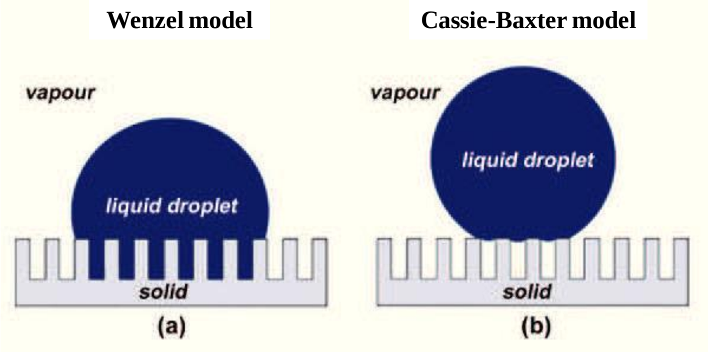

Figure 2.16 Hydrophobic water contact angle with solid surface: (a) Wenzel model, (b) Cassie-Baxter model [158].

solid phase. The Wenzel model [191] describes the contact area between a liquid and solid surface as heterogeneous and composed of air pockets. But for Wenzel model, the amount of wet solid area is greater than that of the smooth area. This means that when a liquid droplet comes into contact with a homogeneous textured surface defined by Wenzel, the liquid seeps into the grooves on the textured surface.

The Wenzel equation provides a relationship between the apparent contact angle θ_w and Young's intrinsic contact angle θ_c as follows:

$$\cos\theta_w = r\cos\theta_c \qquad \text{Equation 2.9}$$

where θ_w corresponds to the equilibrium state on a homogeneous wetting surface and r is surface roughness, defined as the ratio of the actual area of the solid surface to the apparent area:

$$r = \frac{actual\ area}{apparent\ area} \qquad \text{Equation 2.10}$$

where the value of r is always greater than 1. According to Wenzel's equation, the wettability is improved by the roughness of a hydrophilic surface ($\theta_w < \theta$ for $\theta_c < 90°$), but degrades for a hydrophobic surface ($\theta_w > \theta$ for $\theta_c > 90°$). As a consequence, for $\theta_w > 90°$, the free energy of the dry surface is lower than that of the wet solid; therefore the adhesion force between droplet and surface is reduced. On the other hand, a droplet on a rough high energy surface seeps into the textured surface, thus providing a hydrophilic characteristic.

The other set of heterogeneous surfaces were studied by Cassie-Baxter [192] where they assumed that when a liquid droplet settles on the peaks of rough surface, it does not fill the grooves as in Wenzel's model. They assumed that these particular surfaces are composite in nature, including both liquid/solid and liquid/vapour interfaces. Cassie-Baxter devised a complex model to describe heterogeneous surfaces and measure their apparent contact angle with the presence of different materials in the liquid/solid interface. According to Cassie-Baxter, the apparent contact angle is a weighted sum of the cosines of the contact angles on the different homogeneous interfaces:

$$\boldsymbol{\cos\theta_c = \varphi_1 cos\theta_1 + \varphi_2 cos\theta_2} \qquad \text{Equation 2.11}$$

where φ_1 and φ_2 are the dimensionless surface fractions of different phases having contact angles θ_1 and θ_2 respectively. The sum of all φ ratios is equal to 1. When the gas trapped in the grooves below the liquid droplet is air, the equation becomes

$$\boldsymbol{cos\theta_c = \varphi_s cos\theta + (1 - \varphi_s)\cos 180° = \varphi_s(1 + cos\theta) - 1} \quad \text{Equation 2.12}$$

where φ_s denotes the fraction of solid surface area wet by the liquid.

It can be noted from this model that when the liquid droplet sits on the sharp peaks of the textured surface, φ_s tends to zero and θ_c tends to 180°. In this case, the adhesion force between the liquid droplet and solid surface weakens, which allows the liquid droplet to slide easily on the solid surface, thus providing superhydrophobic behavior.

2.3.2 Cleaning Mechanism for Superhydrophobic and Superhydrophilic Surfaces

Superhydrophobic surfaces follow the concept proposed by Cassie-Baxter. Therefore, when a water droplet sits on the surface, it does not seep into the texture, but rather forms almost a complete sphere on the surface, which can referred to a quasi-spherical shape. When the surface is tilted to a certain angle as shown in figure 2.17(b), the water droplet rolls off the surface easily and picks up foreign dirt particles at the same time. In this way, superhydrophobic surfaces can keep themselves clean. Commonly, superhydrophobic surfaces show a self-cleaning property at a sliding angle of 10°. On the other hand, for general surfaces as shown in figure 2.17(a), the water droplet forms a half-spherical shape with the surface. When the solid surface is tilted, the water droplet is unable to carry the dust particles with it causing the surface to remain dirty.

Superhydrophilic surfaces follow the concept of the Wenzel model where the water droplet seeps into the textured hydrophilic surface. Such surfaces have a contact angle of less than 5°, thus exhibiting superhydrophilicity. When the solid surface is tilted to a certain angle, the water forms a sheet across the surface and easily removes dirt as it flows. Superhydrophilicity also prevents a surface from fogging because water spreads instead of forming tiny droplets.

2.3.3 Fabrication Methods for Self-Cleaning Surfaces

Inspired by nature and its processes, technologies have been developed to produce surfaces that can self-clean. The surfaces created either have very low surface energy (hydrophobic/superhydrophobic) or have the ability to break the organic material deposited on them (hydrophilic/superhydrophilic). The

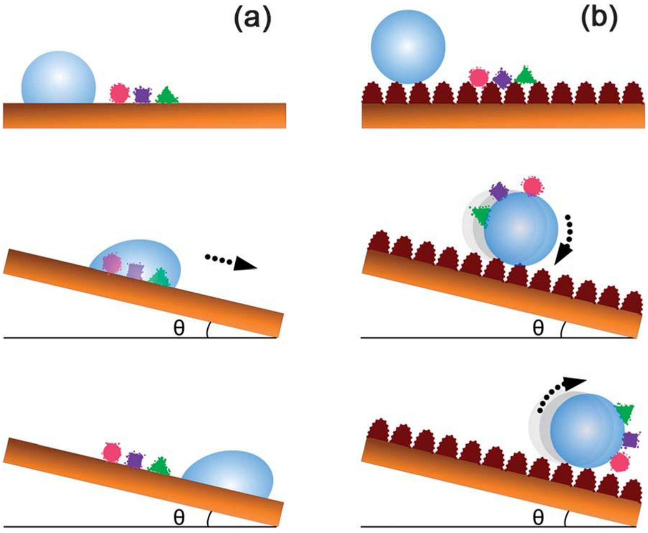

Figure 2.17 Schematic of self-cleaning process shown by superhydrophobic surfaces [159].

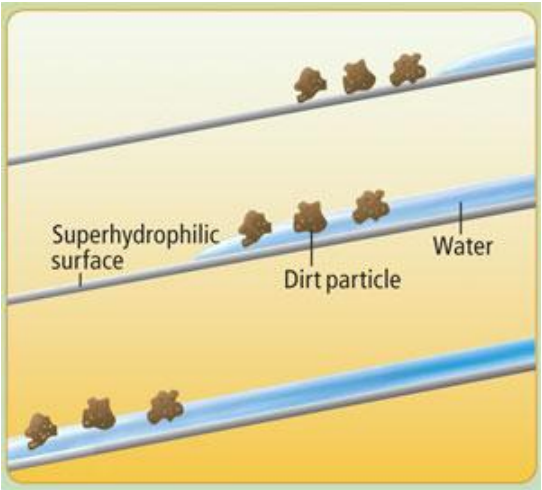

Figure 2.18 Schematic of self-cleaning process shown by superhydrophilic surfaces [160].

development of both surfaces requires strict control over morphology which opens up avenues for new and refined engineered surfaces.

To fabricate self-cleaning surfaces, the most important consideration is the material and not the technique by which that particular material has been applied to the substrate surface. Various techniques have been used to create self-cleaning surfaces such as sol-gel processing [161], self-assembly/layer-by-layer method [162], electrospinning [163], wet chemical reaction [164], hydrothermal reactions [165], electrochemical deposition [166], lithography methods (such as photolithography [167], electron beam lithography [168], X-ray lithography [169], soft lithography [170], and so on), etching [171], chemical vapour deposition [172], electrospraying [173] and sand-blasting [174]. In this section, a brief account of the materials used to create self-cleaning surfaces is given.

Hydrophobic and superhydrophobic surfaces can be created by two techniques: a) making a rough surface from a low surface energy material; b) modifying a rough surface with a material of low surface energy.

Low surface energy materials that are usually modified morphologically to provide hydrophobic/superhydrophobic behaviour are silicone-based materials such as polydimethylsiloxane (PDMS) [175] and PS [176]. PDMS belongs to a group of organosilicone compounds. The intrinsic deformability and hydrophobicity of the PDMS material allows using it as a low surface energy material. A blend of PS-PDMS [177] has also been used to achieve superhydrophobicity. Other silicone materials that have been used for the same purpose are POSS [178], polymerized perfluoroalkyl ethyl methacrylate [179] and PMMA [180].

Fluorocarbons [181] are also emerging materials because of their extremely low surface energies. An example is Teflon. Fluorocarbons exhibit a superhydrophobic property due to the presence of fibrous crystals with large fractions of void space on the surface. However, fluorocarbons are limited by their solubility, so they are not used directly but linked with the other rough materials to make superhydrophobic surfaces.

Inorganic materials such as zinc oxide (ZnO) [182] and TiO_2 [183] have also been used to create surfaces with reversibly switchable wettability. When the inorganic films are exposed to UV irradiation, electron-hole pairs are generated. The electrons in the conduction band react with the lattice metal ions (Zn^{2+}) to form Zn^+ defective sites (also called surface trapped electrons). The holes in the valence band react with the lattice oxygen (O^{2-}) to form surface oxygen vacancies O^{1-}. When a water droplet comes into contact with a UV irradiated ZnO surface, it reacts with the oxygen vacancy sites which causes dissociative adsorption of the water molecules on the surface. The oxygen defective sites are more favourable for the hydroxyl group which promotes increased water adsorption on the irradiated ZnO surface. This water adsorption on the surface tends to reduce the water contact angle, thus the surface exhibiting hydrophilicity. When the ZnO surface is not irradiated, water adsorption does not occur, thus, the surface exhibits hydrophobicity.

Hydrophilic/superhydrophilic coatings can also help in self-cleaning of surfaces. TiO_2 is one of the most common materials that is used to form superhydrophilic coatings. Other materials that are used for the same purpose are tungsten oxide, ZrO_2, ZnO, cadmium sulphide and polyoxometallates.

TiO_2 was first commercialized as a self-cleaning coating by Pilkington in 2001 [184], for fenestration systems. The operating principle of TiO_2 as a self-cleaning material is based on photocatalysis, a natural process that has been well studied in the field of botany. When UV irradiation falls on TiO_2, a photocatalysis process is initiated by absorbing sunlight which allows breaking of organic and dust particles present on the surface of the film. Similar to the photo-activation process of ZnO, the absorption of the photon leads to a charge separation creating electron hole pairs. Electrons combine with oxygen to produce negative oxygen ion and holes combine with water to produce hydroxyl radicals. When organic matter comes into contact with the TiO_2 coating, it combines with the negative oxygen ions and hydroxyl radicals, and converts into CO_2 and water [185]. The hydroxyl radical promotes water adsorption on the surface which imparts superhydrophilicity to TiO_2. The superhydrophilic nature of TiO_2 causes the water to create a sheeting effect and wash away the dirt [186]. TiO_2 is advantageous for outdoor systems since it is cost-effective, non-toxic, and easy to coat in a thin film form and chemically inert in the absence of sunlight. It also allows the decomposition of many organic pollutants such as aromatics, polymers, dyes and surfactants.

However, the refractive index of TiO_2 ($n > 2$) is greater than that of glass, which causes a reduction in optical transmission. This makes optimization difficult in solar applications where the efficiency is dependent in incident light intensity. Therefore, efficient structural morphology on the surface of glass is required which not only provides antireflection effect but a self-cleaning effect as well, but without introducing any foreign coating on its surface. The next chapter will discuss the fabrication of nanostructured glass and the concepts behind the tool used to fabricate and characterize the nanostructured glass.

3. Experimental and Computational Techniques

3.1 Introduction

As discussed in chapter 2, numerous thin-film based single and multi-layer coatings have been developed for broadband and omnidirectional transmission applications but they suffer from short lifetime, reliability and delamination issues. Light trapping nanostructured surfaces have also been developed with porous materials using self-assembly and colloidal lithography and lithographic techniques such as electron beam lithography, and interference lithography but these techniques are expensive, time consuming and suffer from low throughput and incompatibility to industrial production standards. Nanoimprint lithography offers high throughput and scalability to create nanostructured surfaces, but its use is limited by the requirements of the mold, intermediate materials, and limited nanostructure dimensions affecting the performance of the fabricated nanostructures.

In this thesis, an alternative non-lithographic fabrication process was developed to create nanostructures (sub-wavelength features) on the external air-glass interface to impart antireflection properties to the planar glass substrates. This fabrication process does not create a foreign coating on the surface of glass, rather creates a nanostructural morphological change on the top surface of glass. The fabrication process is advantageous since it is less time consuming, easy and scalable. The fabrication process uses a metal assisted nanoparticle template which is created using dewetting of a thin metal film.

Dewetting is a thermally assisted process in which a thin metal film is agglomerated into nanometer or micrometer sized islands using flash heating either using a rapid heating oven [193] or a laser [194]. The metal film is deposited on the glass substrates using electron beam evaporation which is then dewetted using rapid thermal annealing (RTA) to create a metal assisted nanoparticle template. Dewetting of metal films can be carried out using laser heating, but rapid thermal annealing processes are cheaper and industrially viable. Subsequently, glass substrates with metal assisted nanoparticle template are subjected to etching using inductively coupled plasma reactive ion etching (ICP-RIE) to create nanostructures on their surface.

This chapter focuses on explaining the principles of operation and concepts behind the computational, fabrication and characterization techniques used in the course of study to fabricate and characterize nanostructured glass substrates. The optical design of nanostructured glass was simulated using the FDTD software RSOFT. As discussed before, the nanostructured glass substrates were fabricated using a three step fabrication method using electron beam evaporation, RTA oven and ICP-RIE tools. Various optical, I-V and surface morphology characterizations were carried out for nanostructured glass and subsequently fabricated mini solar modules using a UV-Visible spectrophotometer, solar simulator (I-V Tester), goniophotometer, scanning electron microscope (SEM), and EQE tool.

3.2 Computation Method

3.2.1 Finite Difference Time Domain Method

The FDTD method, proposed by Kane Yee in 1966, is one of the simplest methods to implement full wave techniques to solve problems in the field of electromagnetic theory. Yee proposed a discrete solution to Maxwell's equations based on central difference approximations of the spatial and temporal derivatives of the curl equations. His work proved to be a novel approach, staggering the electric and magnetic fields in both space and time to obtain second order accuracy.

The fundamentals of the FDTD algorithm can be explained using a three dimensional Yee cell as shown below where neighbouring grid points are spaced Δx, Δy and Δz in the *x*, *y* and *z* directions, respectively. The electric field components are defined in the middle of the edges whereas the magnetic components are at the centre of the faces.

Maxwell's curl equations can be represented in Cartesian coordinates as six scalar equations. Two such equations have been listed here:

$$\frac{\partial H_x}{\partial t} = -\frac{1}{\mu}\left(\frac{\partial E_y}{\partial z} - \frac{\partial E_z}{\partial y}\right) \qquad \text{Equation 3.1}$$

$$\frac{\partial E_y}{\partial t} = -\frac{1}{\varepsilon}\left(\frac{\partial H_x}{\partial z} - \frac{\partial H_z}{\partial x}\right) \qquad \text{Equation 3.2}$$

The other four equations are symmetrical to the above equations and are obtained by cyclic exchange of *x, y* and *z* subscripts and derivatives. It can be seen from the above equations that a temporal change in the electric (E) field

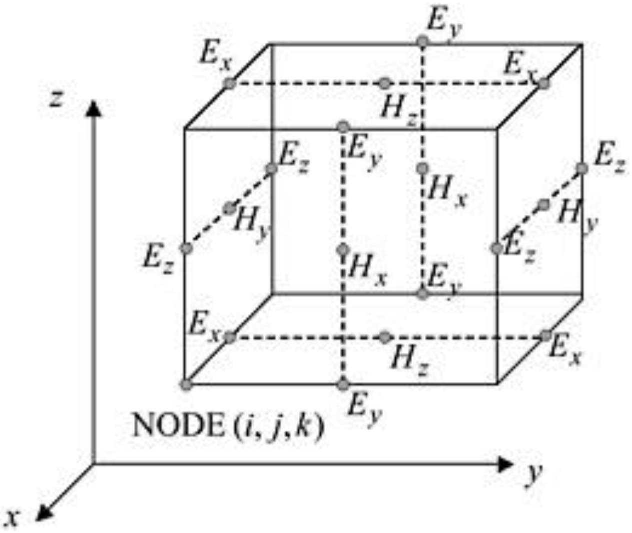

Figure 3.1 Schematic of a Yee cell [196].

is dependent on a spatial change in the magnetic (H) field, and vice versa. The FDTD method solves these equations based on Yee's algorithm stated above by first discretizing the equations via central difference approximation method and then solving the subsequent equations numerically. The *E* and *H* fields are computed at grid points in Yee's mesh. Moreover, the time component is broken into integral time steps representing the computational time. For instance, the *E* field at a time $t = n\Delta t$ is equal to the *E* field at $t = (n\text{-}1)\Delta t$ plus an additional term computed by the spatial change in the *H* field at time *t*.

The numerical computation of Maxwell's curl equations using Yee's mesh results in six equations that can be used to compute the field at a desired grid point, denoted by integers *i*, *j* and *k*. Two example equations are shown below:

$$H^{n+1/2}_{x(i,j,k)} = H^{n-1/2}_{x(i,j,k)} + \frac{\Delta t}{\mu\Delta z}\left(E^{n}_{y(i,j,k)} - E^{n}_{y(i,j,k-1)}\right) - \frac{\Delta t}{\mu\Delta y}\left(E^{n}_{z(i,j,k)} - E^{n}_{z(i,j-1,k)}\right)$$

Equation 3.3

$$E^{n+1}_{x(i,j,k)} = E^{n}_{x(i,j,k)} + \frac{\Delta t}{\varepsilon\Delta y}\left(H^{n+1/2}_{z(i,j,k)} - H^{n+1/2}_{z(i,j,k)}\right) - \frac{\Delta t}{\varepsilon\Delta z}\left(H^{n+1/2}_{y(i,j,k+1)} - H^{n+1/2}_{y(i,j,k)}\right)$$

Equation 3.4

These equations are solved iteratively in a leapfrog manner, alternating between computing E and H fields at subsequent $\Delta t/2$ intervals.

In order to perform a simulation in FDTD based software, a few numerical parameters have to be specified in order to get the good results. They are listed as follows:

1. **Material Properties**: Most simulation software has pre-defined internal material libraries where the name of the material under investigation can be specified. However, if the desired material is not defined, the material properties can be defined, usually in terms of refractive index (n).
2. **Electromagnetic Field Excitation**: The excitation field is a function of spatial and temporal excitation. It can be classified into slab mode, fiber mode, Gaussian, rectangular and multimode in terms of spatial field profile, and continuous wave, pulse and impulse in terms of temporal field profile.
3. **Finite Computation Domain** and **Boundary Condition(s)**: The computational domain is the boundary defined around the device under investigation including source and flux monitors. The boundary conditions are usually defined at the spatial edges of the computational domain and are often categorized into perfect matching layer (PML) and periodic boundary conditions. The PML is an absorbing boundary that does not allow any outward propagating field that hits the limits of the computational domain. It absorbs all the energy impinging on it without inducing any back reflections. On the other hand, periodic boundary conditions are mostly applicable to periodic structures where the simulation domain is an infinite multiple of computational domains repeated in all dimensions.

4. **Spatial Grid Sizes (*Δx, Δy* and *Δz*)** and **Computational Time Step (*Δt*)**: The spatial grid size should be defined carefully to obtain an accurate simulation result and should be small enough to resolve the smallest feature of the simulation domain. The grid size parameters usually depend on the wavelength to be resolved in the materials. The grid spacing must be able to resolve the wavelength in time, and therefore must be ~λ/10 where λ is not the free space wavelength, but rather the wavelength in the material. To define the computational time step, the Courant condition must be adhered to, which relates the spatial and temporal step size:

$$\boldsymbol{c\Delta t} = \frac{\mathbf{1}}{\sqrt{\left(\frac{1}{\Delta x^2}+\frac{1}{\Delta y^2}+\frac{1}{\Delta z^2}\right)}} \qquad \text{Equation 3.5}$$

where c is the velocity of light, and grid sizes represent the smallest grid size in the simulation.

3.2.2 RSOFT Simulation

RSOFT is licensed software, owned by developer Synopsys' Optical Solutions Group. This particular software is used in industry to address challenging problems ranging from physics of component design to the business implications of planning wired and wireless networks [197]. The software works with a CAD environment. In our case, the FULLWAVE module of RSOFT software has been used to compute the transmission flux spectra of planar and nanostructured glass substrates at normal and oblique angles of incidence. The advantage of this software is that it has a graphical user interface which allows the user to specify and set the required simulation parameters easily. Details about the simulation domain and components will be provided in Chapter 4.

3.3 Nano-Texturing of Planar Glass

The glass cover is an important component of a PV module. It is an optically transparent and thermally stable material which provides a protective covering to the solar modules. It has already been discussed in Chapter 2 that this protective covering of solar modules suffers from reflection loss. Thus, a non-lithographic method has been adopted in this thesis to create nano-textured glass.

In this section, a summary of the working principles of fabrication equipment used to fabricate nano-textured glass will be discussed.

3.3.1 Electron Beam Evaporation

Electron beam evaporation is a physical vapour deposition technique which is used to produce uniform high-purity films and optical coatings. This deposition technique allows deposition of a wide variety of materials including refractory metals (such as tungsten), low vapor pressure metals (such as platinum), and alloys [198].

Figure 3.2 shows the apparatus of an electron beam evaporator. The material to be deposited is placed in a water-cooled hearth; meanwhile the material to be coated is shown as the substrate. The substrate is rotated at a constant speed so that the coating material is deposited uniformly over the

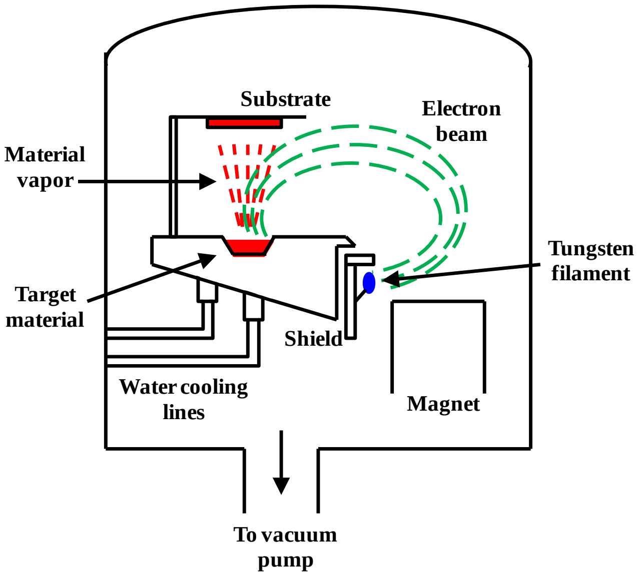

Figure 3.2 Schematic of an electron beam evaporator [199].

substrate. The process of evaporation takes place in a high vacuum environment to allow evaporated material particles to move freely in the chamber and deposit on the substrate.

The working principle of electron beam evaporation is divided into two stages:

1. Thermionic emission of electrons: Thermionic emission is a process of discharging of electrons from a heated material, in this case, a hot tungsten filament. The tungsten filament, held at a high negative potential, is supplied with enough energy for the electrons to overcome the attractive force that holds them. Once the electrons are excited, they are free to move.

2. Deposition of material on the substrate: Electrons leaving the filament are magnetically focused and then deflected 270° by an integral permanent magnet. The electron beam is then accelerated into the evaporant material contained within a water-cooled, grounded crucible. The beam strikes the evaporant material with a spot of approximately 1/8" diameter and an intensity of approximately 25 kW/cm^2 [200]. The electrons are swept across the evaporant material contained in the crucible by an electro-magnetic system, with either manual or automatic controls. The rate at which source materials may be evaporated is dependent on power input, charge shape, and the characteristics of the material to be evaporated [200]. The highest evaporation rates are obtained with materials that have low evaporation temperatures and low thermal conductivity [200]. The evaporator system operates at a vacuum pressure of 10^{-6} mbar. This low pressure allows the evaporant particles to move towards the substrate. The pressure, which normally increases during evaporation, depends on the pumping capacity of the system and the cleanliness of the evaporant material. This pressure increase is minimized by the high thermal efficiency of the source. There is minimal outgassing of surrounding surfaces because only the evaporant is heated.

Advantages: The electron beam evaporator provides advantages over its counterparts such as CVD and sputtering, that the tool offers lower process risk and usually the materials are cheaper. It also offers high deposition rate and creates less surface damage from the impinging atoms as the film is being formed.

Disadvantages: Maintenance cost of the equipment is higher and requires constant changes of tungsten filaments since they are operated at high currents. It is hard to obtain a uniform step coverage as compared to sputtering techniques. The tool also generates X-rays which might be harmful for the substrate.

In this thesis, electron beam evaporation is employed as a first process step for fabrication of nanostructured glass substrates. 10 nm of Ni has been deposited on glass substrates.

3.3.2 Rapid Thermal Processing

Rapid thermal processing (RTP) is a key fabrication technique for the semiconductor device fabrication industry where it has replaced the conventional furnace processing (CFP) technique employing hot quartz tubes. Common applications of RTP are formation of ultra-thin gate dielectrics, activation of ion-implanted dopants and formation of metal silicides [201].

In CFP, convective and conductive heat flow play an important role, whereby there is a thermal equilibrium between the wafer and the surrounding quartz tube. However, the heating principle in case of RTP is based on optical energy transfer where the wafer is not in thermal equilibrium with its surroundings. The most basic requirement of heating a wafer rapidly in an RTP chamber is that the wafer should have a non-zero absorption coefficient "α" over a wide range of wavelengths. When a wafer is irradiated in an RTP chamber, α increases rapidly with processing temperature. Thus, when impinging photons have energies higher than the bandgap energy of the wafer

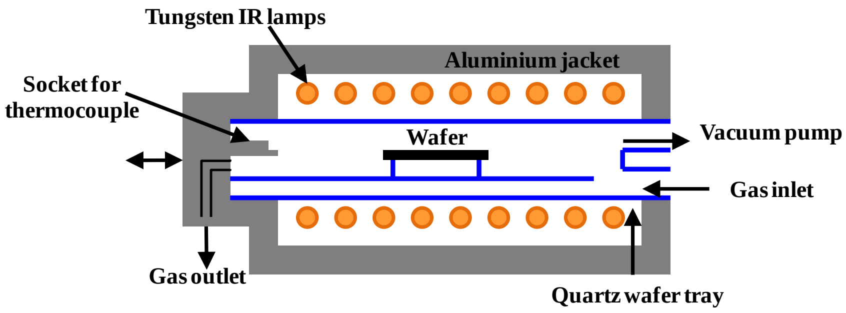

Figure 3.3 Schematic of rapid thermal annealing oven.

material, they are absorbed and hence, heat is transferred. Due to this, the energy spectrum of the source should feature a significant proportion of high energy photons when rapidly heating materials from room temperature.

Figure 3.3 shows a schematic of the RTP chamber used in this thesis. In the chamber, the wafer to be processed is placed on a quartz tray. The chamber can hold at maximum a 4-inch wafer. The wafer can be heated from both sides by 18 tungsten halogen lamps of 1 kW electric power each, default being heating from below. The vacuum and gas inlet are behind the quartz tray, where the processing gas is subjected to laminar flow by distribution plates (not shown here). The chamber is covered by an aluminium jacket which is surrounded by water-cooled walls. In this RTP, the wafer temperature is measured using a K-type thermocouple.

Advantages: RTP enables the applicable of fast ramp-up and ramp-down cycles which cannot be met by CFP. In a CFP, heating is restricted by high thermal mass of the system as well as the method by which heat energy is transferred to the wafers. For example, when large numbers of wafers have to be heat treated in conventional tube furnaces, they have to be pushed in slowly (10-15 cm/sec), otherwise wafer breakage may occur due to induced heat stress. This stress is caused by inhomogeneous heating of the wafers from the edge to the centre. In contrast, RTP allows uniform heating of the sample because each wafer is heated individually and uniformly. RTP also offers a fast method of transferring energy to and away from the wafer.

Disadvantages: RTP allows a fast method of transferring energy but a single chamber RTP can only handle a single wafer at a time which increases manufacturing time and cost. In-line RTPs are available in the market but they add an additional cost to manufacturing line and suffer from cross chamber contamination.

In this thesis, RTP is employed for annealing Ni coated glass substrates at a temperature of 600°C for 5 minutes. The rapid annealing of the Ni film caused the thin film to break into nano-islands/nanoparticles which are used as a mask for a subsequent etching process. The breaking of a thin film of Ni into nanoparticles is due to a dewetting mechanism which will be summarized in Chapter 5.

3.3.3 Inductively Coupled Plasma Reactive Ion Etching

The plasma etching process is an important process in the semiconductor fabrication industry. High density ion fluxes generated by low pressure plasmas can be employed to generate anisotropic etching of a wide variety of materials. Common applications of ICP-RIE are integrated circuits [202], microelectromechanical systems [203], photonic crystals [204], waveguide fabrication [205], etc. ICP-RIE systems combined with mass spectrometers are even used in the oil and gas industry to characterize different elements in new fossil fuels [206].

The key parameter in an ICP-RIE system is the control of the plasma density and momentum imparted to the ions.

Alone, RIE uses chemical reactive plasma to etch materials. The plasma is generated in a vacuum environment by a radio-frequency (RF) electromagnetic source (shown as RIE generator in figure 3.4) at 13.56 MHz. A dark sheath is formed around the wafer to be etched. Due to the potential difference across the sheath region, the ions get accelerated and impinge at

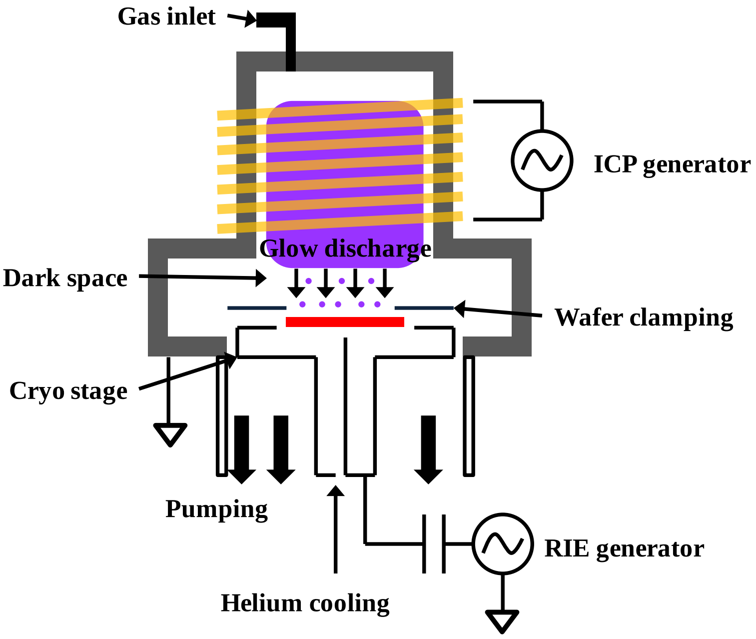

Figure 3.4 Schematic of an ICP-RIE.

high energy on the wafer causing the etching process. Since the energetic ions impinge on the wafer in a vertical direction, RIE produces anisotropic etch profiles in contrast to isotropic profiles generated by wet etching methods.

However, ICP has an added advantage when used with RIE. The ICP causes excitation using a time varying RF source which is delivered inductively via a coil wrapped around the RIE discharge region. This generates a magnetic field which in turn causes an electric field (according to the Maxwell-Faraday equation) that tends to circulate plasma in parallel to RIE plates. Thus, there is an increase in the plasma density by increasing the ICP power which reduces the processing time. Thus, in an ICP-RIE combination, the ICP controls the number of ions reaching the wafer to chemically etch whereas RIE controls the momentum of the ions (due to potential difference) reaching the wafer.

In this thesis, ICP-RIE is employed for etching planar glass with Ni nanoparticles as the etching mask using SF_6/Ar plasma. The etching depth is controlled by etching time which varies from 1-8 minutes. Common plasma chemistries used to etch glass samples are CHF_3/SF_6, CHF_3/CF_4 and SF_6/Ar. The glass substrates usually consist of metallic impurities which often generate non-volatile compounds such as AlF_3 and NaF during the etching process. Since Ni metal masks have been employed here for etching, non-volatile compounds will be generated. These non-volatile compounds inhibit the formation of perfectly straight sidewalls but it is not of concern to this work, since the application studied here requires tapered structures.

In this work, a fluorine based plasma (SF_6/Ar) is generated by using the following conditions in an ICP-RIE chamber (SLR-770, Plasma Therm): 10 mTorr pressure, 20 sccm SF_6, 4 sccm Ar, 100 W RIE RF power and 500 W ICP RF power.

3.4 Characterization Techniques

This section discusses various characterization techniques employed for morphological and optical studies of planar and nanostructured glass samples. I-V measurements are conducted for solar modules where planar and nanostructured glass substrates are used as their packaging covers.

3.4.1 Scanning Electron Microscope

The SEM technique is a fast and convenient imaging method for nanoscale structures. The SEM was developed by a British scientist, Prof. Charles Oatley in 1952. It employs an accelerated and focused beam of electrons (carrying significant amount of kinetic energy. These electrons are impinged on the sample under imaging, where these incident electrons decelerate in the solid sample. The electron-sample interaction produces various signals which provide topographical and chemical information for the materials such as surface texture, chemical composition, crystalline structure and structure orientation of the materials. The schematic diagram for SEM equipment is shown in figure 3.5.

The electron source for an SEM can be thermionic or field emission source. The thermionic sources such as tungsten filaments are heated up to emit electrons whereas in field emission sources, electrons are emitted from a sharp tungsten tip by applying an electric field. This field emission gun requires an ultra high vacuum system with a pressure of 10^{-8} Pa, provides higher brightness, higher current density and longer lifetime as compared to the thermionic sources.

The emitted electrons from the sharp tungsten tip are accelerated by applying a voltage up to 30 keV to an anode along the microscope column. Magnetic lenses are used to focus the accelerated electrons to a beam that raster scans the area of interest. When the accelerated electrons hit the specimen under imaging, they are scattered both elastically by the electrostatic interactions with the atomic nuclei and inelastically due to interactions with the atomic electrons.

The signals generated by the electron-specimen interactions are summarized in the figure 3.6 below. Backscattered electrons are defined as the emitted electrons due to inelastic scattering of the primary electrons. These backscattered electrons are a function of the atomic number, where the image

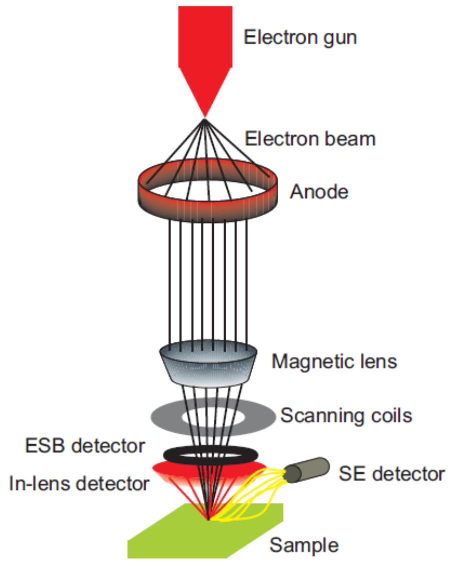

Figure 3.5 Schematic of a field emission SEM [207].

contrast increases for a material with higher atomic number. The secondary electrons are emitted electrons generated by collisions of primary electrons with the outer shell electrons. These electrons are emitted with a wide range of energy depending on the binding energies of the outer shell electrons in the atom.

Different detectors are employed to reveal different information depending on the type of radiation emitted from the sample. The backscatter electrons are a function of the atomic number of the specimen; therefore, they give information about the material contrast of the specimen. The secondary electrons usually provide topographical information where the brightness of the signal received depends on the generated secondary electrons.

An SEM also has the ability to provide analytical data in addition to topographical information. As the primary electrons impinge on the surface of the specimen, they interact with the surface atoms to yield greater signal than

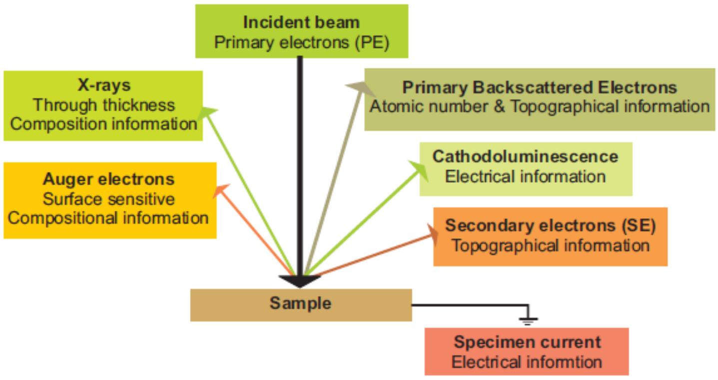

Figure 3.6 Summary of the signals that can be measured using an SEM [207].

secondary and backscattered electrons. Among them are Auger electrons and characteristic X-rays. The X-rays have discrete energy values, characteristic for the atomic structure of the atom from which they are emitted. Energy dispersive X-ray analysis is a process where emitted X-rays are collected and their inherent energies are analyzed. As a result, combining the scan information from secondary and Auger electrons, together with the X-ray information allows the complete mapping of surfaces on a nanometer scale.

The requirement of SEM is that the sample under imaging should be conductive. In case of non-conductive samples such as glass (being used in this thesis), a thin layer of gold or platinum (10 nm) needs to be coated to avoid build up of charges on the surface of the sample. Sometimes, a thin metal layer is insufficient to dissipate charging effect, therefore, an extra copper or aluminium tape should be used for this purpose.

In this thesis, scanning electron microscopy was conducted to study the effect of annealing temperature on the dewetting characteristics of a Ni metal thin film. It was also used to conduct cross-section imaging of etched glass samples after the ICP-RIE process.

3.4.2 UV-Visible Spectrophotometer

A UV-Visible spectrophotometer (SolidSpec 3700, Shimadzu) has been used to study the hemispherical transmission spectra of planar and nanostructured glass samples. The spectrophotometer shown in figure 3.7 consists of an arrangement of a white light source (50 W halogen lamp), monochromator, and reflecting mirrors and an integrating sphere (inner diameter of 60 mm) with $BaSO_4$ lining in it for perfect reflections and zero absorption.

The monochromator is used to generate a single wavelength light which is then irradiated on the sample under measurement. A white light source is focused and collimated by a series of lenses and mirrors into a monochromator. Then, the collimated white light enters a diffraction grating in the monochromator, thus producing one particular wavelength at a time. The diffraction grating rotates to cover wavelengths from 240-1200 nm. The wavelength range can be selected by the users. The wavelengths generated by the monochromator are then guided by a series of mirrors to irradiate the measurement sample.

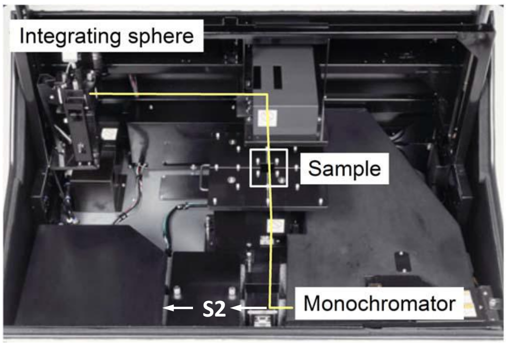

Figure 3.7 Optical path for the measurement of hemispherical transmission in a spectrophotometer using an integrating sphere. S2 is the sample under measurement (for example, glass in this experiment).

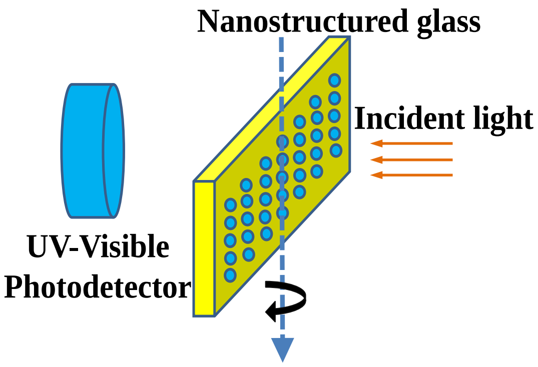

Figure 3.8 Measurement of specular optical transmission at oblique angles of incidence.

The transmitted light through the measurement sample is then collected by integrating sphere detectors. The integrating sphere is a hollow cavity with a diffused and reflective white coating. Finally, the light collected in the integrating sphere is measured by the attached detector. Two types of detectors are used to measure the wide range of spectrum. A photomultiplier Si detector is used for the visible spectrum (240-760 nm) and an indium gallium arsenide detector for the near-infrared spectrum (760-1200 nm). The detectors are switched automatically to detect the required wavelengths.

Specular transmission has also been measured at oblique angles of incidence using the direct mode of UV-Visible spectrophotometer (figure 3.8). In the direct mode of measurement, the light after passing through the monochromator is not deflected to the sample stage as shown in figure 3.7. It travels straight through the samples marked S2 to the detectors behind them. In direct mode measurement, the detector is 150 mm away from the sample, so it measures only the light transmitted through the sample in the center whereas it is unable to measure the scattered or diffused portion of the transmitted light.

A haze measurement was carried out at normal incidence of light for planar and nanostructured glass samples using the integrating sphere in the spectrophotometer. This provides information regarding the scattering properties of the glass samples. Figure 3.9 shows the measurement procedure where the integrating sphere is used in different configurations. In measurement T1, a transmission measurement is carried out in air medium without any sample in the light path, thus giving 100% transmission at all wavelengths. In T2, a similar transmission measurement is carried out with the sample in the light path. T2, actually measures the transmission. In measurement T3, the sample is removed and the port opposite to the input port is opened to allow the incident light to escape. Therefore, the light collected by the integrating sphere is about 0-1% due to the small size of the port. In measurement T4, the sample is introduced in the light path. When light is incident on the sample, the detector measures only the scattered portion of the transmitted light, and the specular portion escapes through the open port. Then, the haze is computed by a mathematical expression given as:

$$\boldsymbol{Haze} = \left(\frac{\boldsymbol{T4}}{\boldsymbol{T2}} - \frac{\boldsymbol{T3}}{\boldsymbol{T1}}\right) \times \mathbf{100}\% \qquad \text{Equation 3.6}$$

In this thesis, UV-Visible spectrophotometer has been used for specular and hemispherical transmission measurements of planar and nanostructured glass samples. Specular transmission measurements have also been carried out at oblique angles of incidence.

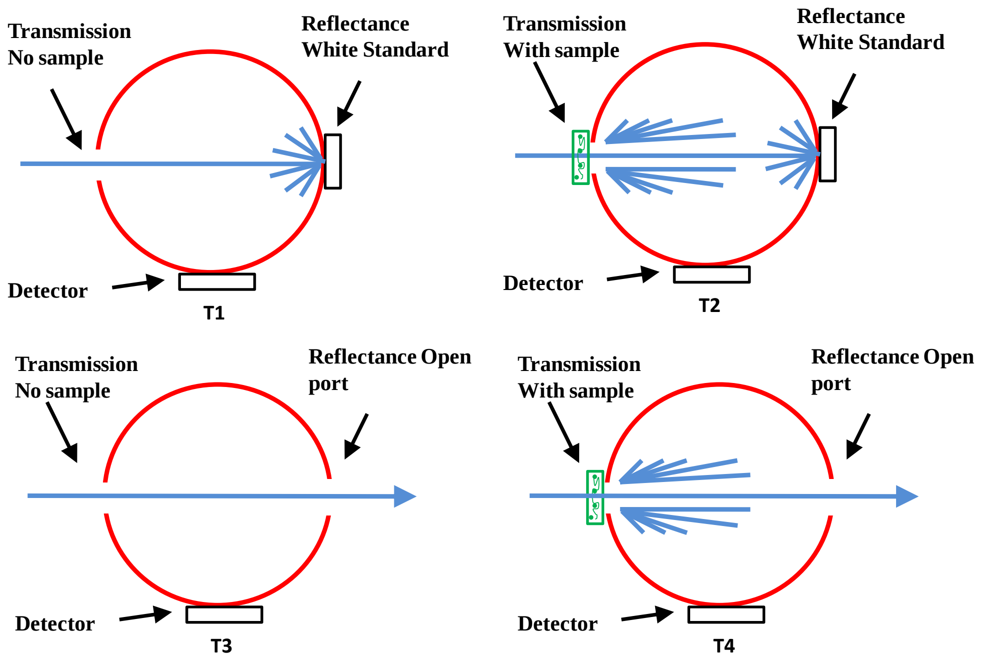

Figure 3.9 Measurement configurations to compute haze using a spectrophotometer [232].

3.4.3 I-V Testing of Solar Modules (Solar Simulator)

A solar simulator is a piece of laboratory equipment which replicates the solar spectrum. It is used to measure the measure the I-V characteristics of solar cells and solar modules in a controlled environment. The schematic diagram for a solar simulator tool is shown in figure 3.10.

The xenon arc lamp is the heart of the device which emits a blackbody-like spectrum. The ellipsoidal reflector around the xenon lamp allows efficient beam collimation and no loss of the emitted light to the surroundings. The combination of mirrors, optical integrator, spectral mismatch filters and a collimating lens allows a continuous output of a uniform collimated beam with a solar like spectrum. The filters used in the tool depend on the PV application. Usually an AM 1.5 filter is used for standard solar cell

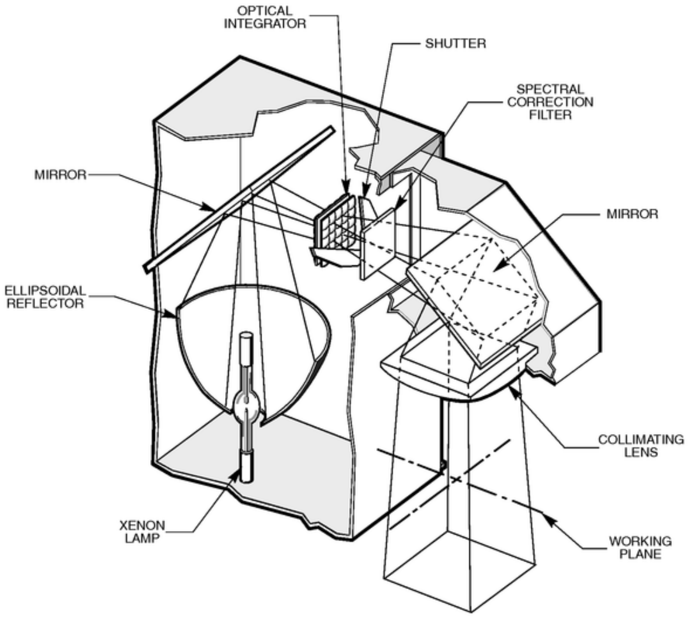

Figure 3.10 Schematic of a solar simulator [208].

applications which modifies the visible and UV portions of the xenon lamp spectrum to match the standard solar spectrum.

Standard spectra have been developed for solar simulators based on publications of The American Society for Testing and Materials, known as AM 0, AM 1.5 Direct, and AM 1.5 Global for the 37° tilted source as shown in figure 3.12. These are a representative of average conditions in the 48 contiguous states of the United States of America. These published spectra have also been certified by the Committee Internationale d’Eclaraige (CIE), the world authority on radiometric and photometric nomenclature and standards.

The absorption and scattering levels in the atmosphere are variable, resulting in changes in the radiation received at the earth’s surface. Seasonal variations and trends in the ozone level also have a tremendous effect on the terrestrial UV level. The irradiation at the earth’s surface also depends on the earth-sun distance (elevation), time of day and solar rotation which all change the absorption and scattering path lengths. With the sun overhead, the direct radiation that reaches the surface after passing through the atmosphere is termed “Air Mass 1 Direct” radiation. The global radiation with the sun overhead is similarly called “Air Mass 1 Global”. Since there is no air mass above the atmosphere, the solar radiation is termed as the “Air Mass 0” spectrum. The atmospheric path for any zenith angle is described with respect to the overhead air mass. That is how Air Mass 1.5 and Air Mass 2.0 have also been defined.

Commonly used solar simulators or I-V testers consist of filter lenses which duplicate the AM 1.5 spectra. They employ a xenon arc lamp which has an excellent spectral match to the AM 0 or terrestrial spectrum. The solar simulator can be operated in either continuous or pulsed mode depending on the application. The beam collimation by the filter lenses simulates the direct terrestrial beam and allows the characterization of solar cells and solar modules.

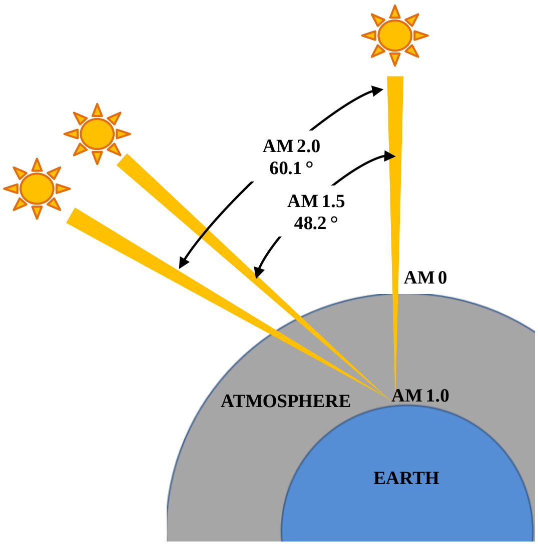

Figure 3.11 Schematic of AM standards set by ASTM.

)

In this thesis, I-V testing has been conducted on solar modules with planar and nanostructured glass samples as their packaging covers.

3.4.4 Contact Angle Measurement

Surface energy is a key parameter when defining properties of surfaces. One of the best methods to measure surface energy of a solid surface is a contact angle measurement. The theory of contact angles has already been summarized in Chapter 2.

The contact angle is measured for solid surfaces using the sessile drop method. The equipment required for this measurement is called an optical tensiometer. The schematic of the optical tensiometer is shown in figure 3.12. It consists of an automated water droplet system for dispensing water droplet, stage to hold the sample under measurement, light source and a charged coupled device (CCD) camera to capture the image of a water droplet resting on the sample surface.

The automated water droplet system enables the users to vary the type and volume of the liquid depending on experimental preferences. The contact angle measurement software analyses the image of a water droplet on the

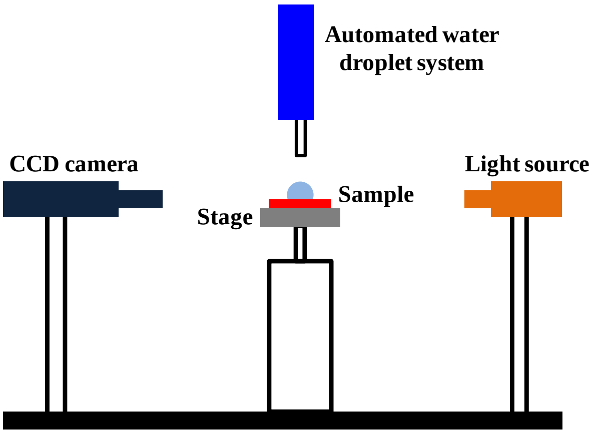

Figure 3.12 Schematic of contact angle measurement.

sample and measures the contact angle by calculating the slope of the tangent line to the drop at the liquid-solid-vapor interface line.

In this thesis, contact angle measurements have been conducted on planar and nanostructured glass samples before and after outdoor exposure.

3.4.5 Angle Resolved Scattering Measurement

The angle resolved scattering of textured samples is an important measurement since it provides information on the diffused component of light when it strikes the surface of the samples.

Scattering measurements are usually carried out in the field of thin film solar cells where transmitted diffused light created by texturing of front glass plays an important role. Generally, spectral and bidirectional optical scattering are reported and measured by a device called a goniophotometer. These devices have been used widely in the fenestration system industry [209] as well to assess bidirectional optical properties of fenestration systems.

The word “gonio” is derived from Greek meaning angle and “photometer” is an instrument which measures light. Thus, a goniophotometer is an instrument that measures the transmission or reflection of radiation by objects and materials at different angles. Goniophotometers have been widely used to study the optical properties of light emitting devices [210], lamps [211], ground surfaces and ground textures [212], and natural materials such as wood [213].

Goniophotometers measure the photometric bidirectional transmission (reflection) distribution function BT(R)DF, as defined by CIE, which can be described mathematically [214] as follows:

$$\boldsymbol{BT(R)DF_V\left(\theta_{t(r)},\varphi_{t(r)},\theta_i,\varphi_i\right)=\frac{L_V\left(\theta_{t(r)},\varphi_{t(r)},\theta_i,\varphi_i\right)}{E_V(\theta_i)}} \qquad \text{Equation 3.7}$$

- $(\theta_{t(r)},\varphi_{t(r)})$ are the zenithal and azimuthal angles of emergence of transmitted (or reflected radiation)
- (θ_i,φ_i) are the angles of incidence on incoming radiation illuminating a sample,
- L_V is the luminance of transmitted (reflected) light,
- E_V is the illuminance of incoming radiation.

The units of BT(R)DF are inverse steradians (sr^{-1}). Important parameters to know before measuring BT(R)DF are the angle of incoming radiation (θ_1, φ_1), the total illuminance on the sample (shown as $L_1*d\omega_1*cos\theta_1$), and measurements of the transmitted (or reflected) luminance L_2 transmitted in the direction (θ_2, φ_2).

The three main components of a scanning goniophotometer (figure 3.13) are illumination lamp which can be a halogen lamp or a xenon lamp, a detector head and a sample stage.

A configurable lamp shines at the sample placed at the sample holder, which can be rotated along two axes to vary the incident angle (φ_i, θ_i) of the light. The detector head performs continuous rotational movement around the sample center taking different paths to complete an entire sphere. At specific time intervals defined by the user, the location of the detector head and the radiance detected (by CCD camera attached to detector head) are recorded. The resolution of the scan is defined by the time interval and density of scan paths. The result of the scan is a set of varying densities on an imaginary spherical surface with the associated luminance readings. A reference beam

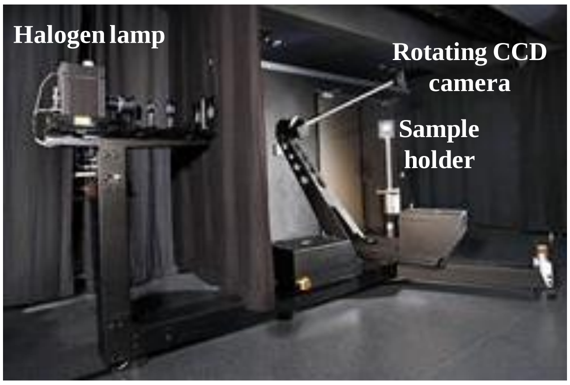

Figure 3.13 System setup of a goniophotometer system [214].

consisting of the unobstructed beam of the lamp is measured followed by another beam with the sample in the path of incident beam of light. Application of suitable reflection or transmission models results in a complete description of BT(R)DF of the sample.

In this thesis, a goniophotometer is used to measure the scattering properties of planar and nanostructured glass substrates.

3.4.6 External Quantum Efficiency Measurement

Spectral photocurrent response measurements yield the number of electrons that are collected per incident photon at each wavelength. Hence, it is called external quantum efficiency (EQE), or collected electron flux to incident photon flux. The spectral responsivity (SR) of a solar cell is an important factor to be considered, given by amperes generated per watt of incident light. Ideally, SR increases with wavelength. However, at short wavelengths, cells cannot use all the energy in the photons, whereas at long wavelengths, the photon energy becomes less than the bandgap and none are absorbed. SR can be calculated as follows:

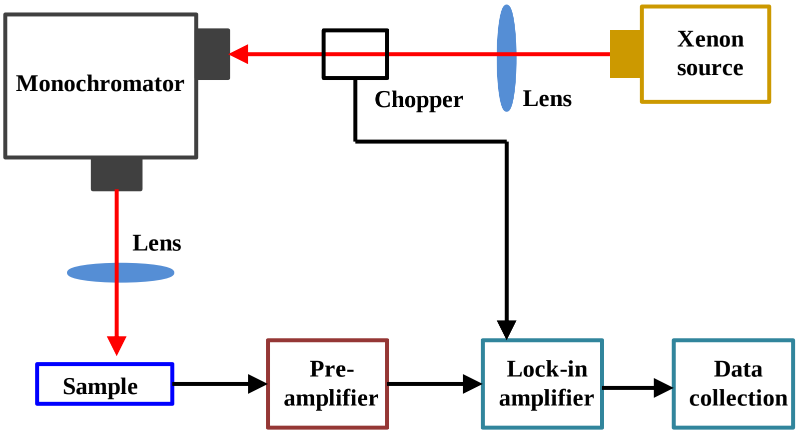

Figure 3.14 Schematic of an EQE measurement setup.

$$SR = \frac{I_{sc}}{P_{in}(\lambda)} = \frac{q \times n_e}{\frac{hc}{\lambda} \times n_{ph}} = \frac{q\lambda}{hc} EQE \qquad \text{Equation 3.8}$$

where n_e is the number of photoelectrons collected, per unit time, and n_{ph} is the number of incident photons (of wavelength λ) per unit time, P_{in} is the incident light power and EQE is the external quantum efficiency which is the ratio of the collected electron flux to the incident photon flux. Figure 3.14 shows the schematic diagram of an EQE measurement setup.

EQE is measured under illumination from a xenon lamp passing through a monochromator. The incident beam is chopped at a certain frequency and focused on the sample surface. If the output signal is low, it is generally amplified using a trans-impedence amplifier and then detected with a lock-in amplifier. It is always important to use a calibrated crystalline Si solar cell for reference before each measurement. A lock-in amplifier has a high signal-to-noise ratio, which is important in achieving accurate EQE data.

3.5 Conclusions

This chapter discussed the non-lithographic fabrication technique employed in this thesis to fabricate nanostructured glass samples. The chapter further discussed various fabrication and characterization techniques employed to fabricate nanostructured glass and test their performance indoors. However, before a device is actually fabricated, simulations should be carried out in order to determine the parameters that would be essential for a working device. Therefore, simulations of nanostructured glass samples with different feature size are described in the next chapter. Their performance has been compared to that of planar glass and thin film coatings on glass.

4. Optical Design of Nanostructured Glass

4.1 Simulation model

The focus of this chapter is to calculate the optical transmission of planar and nanostructured glass surfaces and study the feature sizes that can affect their optical transmission property. Additionally, 3D simulations are also presented which can provide some insight into the practical results. Figure 4.1 shows the 2D schematic diagram of the structure or model used for simulation.

The simulation model consists of an electromagnetic Gaussian broadband source whose angle of incidence changes from 0° to 70° to study the omnidirectional transmission of the simulated nanostructures. The simulation structure has been constructed to be wider in the x axis than the z axis to minimize absorption of light at both sidewalls. The grid size of the simulations has been chosen to be as small as possible to resolve the incoming electromagnetic light. The refractive index of air is 1 and that of glass is dispersive where the refractive index changes with wavelength of incident light. The simulations are computed in the transverse electric (TE) polarization but effect of the transverse magnetic (TM) polarization has also been presented for one of the simulation cases. This has been done because the incident light in real-life conditions is partially polarized and consists of both TE and TM polarizations. The simulation domain is terminated on the left and right side with a periodic boundary layer to reflect the light back into the simulation domain. The direction normal to the propagation direction has

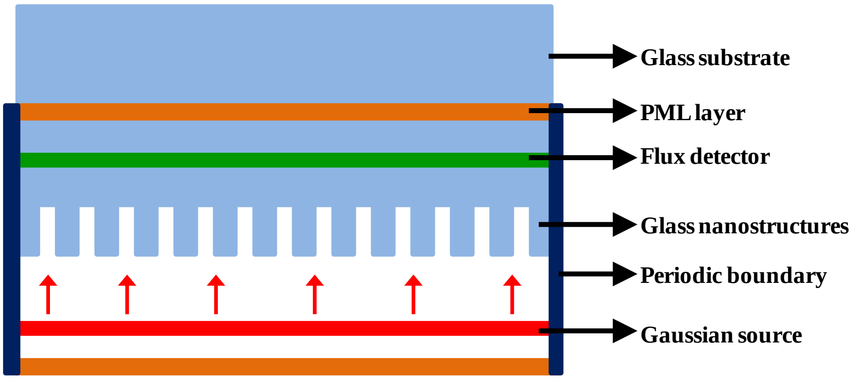

Figure 4.1 Schematic of 2D simulation.

PML layers at the end of simulation domain to avoid any reflections and interaction with the source. The antireflection sub-wavelength structures are defined as stacks of cylinders (rectangles in two dimensions) with different diameters, heights and spacings.

The refractive index of air is chosen to be $n_o = 1.0$ and $n_g = 1.52$ for glass. In addition, the transmission values of transverse-electric and transverse-magnetic polarized waves has been neglected and the source has been assumed to be like non-polarized sun source similar to the measurement techniques used later for characterization.

4.2 Comparison between planar glass, thin film single dielectric layer and nanostructured coating

Planar glass suffers from 4% reflection loss at the primary air/glass interface. As stated earlier in chapter 2, homogeneous single layer dielectric coatings were proposed to minimize the reflection of light at surfaces of quarter wavelength thickness and refractive index equal to the geometric mean of the refractive index of the substrate and the surrounding medium.

The maximum transmittance can be obtained when the thickness of this dielectric layer satisfies the following relation:

$$\boldsymbol{d = \frac{\lambda}{4n}} \qquad \text{Equation 4.1}$$

where d is the thickness of the homogeneous single dielectric layer, λ is the wavelength of light, and n is the refractive index of the dielectric layer. The refractive index of the thin dielectric layer for an air-glass medium would be 1.22. Therefore, assuming the wavelength of incident light to be 550 nm, for the refractive index of dielectric layer to be 1.22, the thickness of the single dielectric layer should be 112.7 nm.

Figure 4.2 shows a comparison between the optical transmission of planar glass and a single layer coating on glass at several angles of incidence. It can be seen from the figure 4.2 (c) and 4.2 (f) that the single layer dielectric film shows an improvement in the optical transmission as compared to that of the planar glass. As designed for a wavelength of 550 nm, the dielectric film shows maximum transmission around this wavelength (comparing figures 4.2 (e) and (f)). Additionally, an improvement was also noticed at oblique angles of incidence but only around the wavelength ~550 nm, thus showing the single wavelength limitation of thin film coatings. Due to partial polarization of light in real-life conditions, TM simulations have been carried out. It can be seen from figure 4.2 (b) and 4.2 (d) that TM simulations for planar glass and thin film coating present a significant increase in the optical transmission at higher angles of incidence, precisely after 40°. This sudden increase in the optical transmission is in agreement with the Fresnel equations for TE and TM polarization modes where maximum transmission should be observed near the

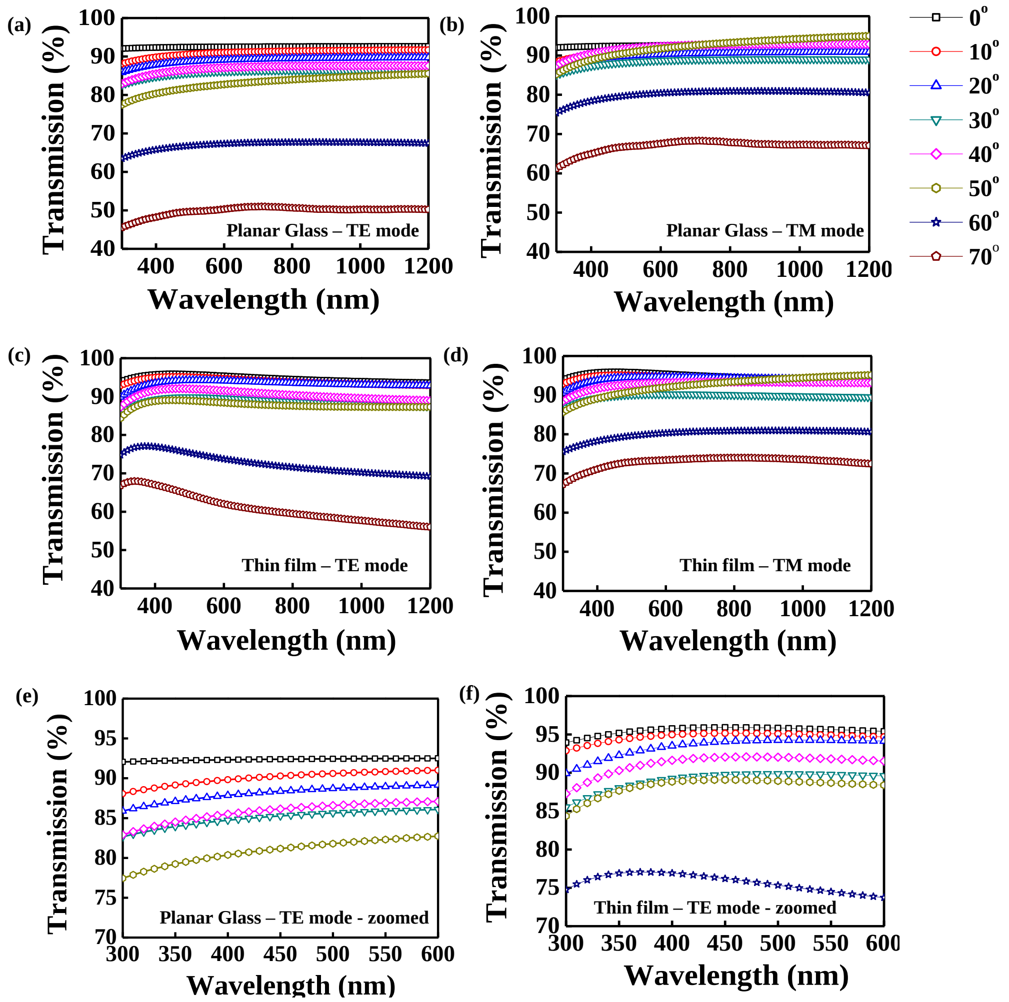

Figure 4.2 Optical transmission of (a) planar glass (TE mode), and (b) planar glass (TM mode), (c) thin film single dielectric layer on glass (TE mode), (d) thin film single dielectric layer on glass (TM mode), (e) Zoomed graph of (a), and (f) Zoomed graph of (b), for several angles of incidence of light.

Brewster angle (air/glass interface = 56.31°).

Taking inspiration from nature, nanostructured surfaces were employed to improve the omnidirectional and broadband transmission behavior of planar glass for increasing the power output of solar modules. In this section, a layer with cylindrical structures is simulated instead. The dimensions of these structures are less than the wavelength of the incident light and the structure has a uniform filling fraction along the thickness. Assuming the height of the structures is 200 nm with a diameter of 100 nm (from the experimental data of

Chapter 5, shown later), the spacing needs to be calculated to give the correct effective index. For nanostructured layers, the effective refractive index is given as

$$\boldsymbol{n_{eff} = \left[f n_s^q + (1-f) n_{air}^q\right]^{\frac{1}{q}}} \qquad \text{Equation 4.2}$$

where q = 2/3 [215], and f is the filling fraction. The value of q is chosen such that it satisfies the effective medium theory for the glass material [59, 233]. Substituting n_{eff} = 1.22 and value of q, f can be calculated as 40%. If f = 40% and diameter of cylinders is 100 nm, the spacing between subsequent cylinders would be 250 nm. Therefore, simulations were performed at normal and oblique angles of incidence with nanostructures of dimensions 200 nm height, 100 nm diameter and a pitch/spacing of 250 nm.

The optical transmission of a nanostructured layer on glass is shown in figure 4.3 (a) for several angles of incidence. It can be clearly seen that there is a dramatic improvement in the transmission as compared to planar glass and a thin dielectric layer of quarter wavelength thickness. At normal incidence, the nanostructured layer shows up to a 3% improvement in optical transmission for a broad range of wavelengths, as evident from figure 4.3 (a). The omnidirectional effect of the nanostructured layer is quite evident from figure 4.3(b) where an increase in transmission is observed up to a 70° angle of incidence. The reason behind such an increase is the gradient change in the refractive index offered by nanostructured layer as compared to thin dielectric

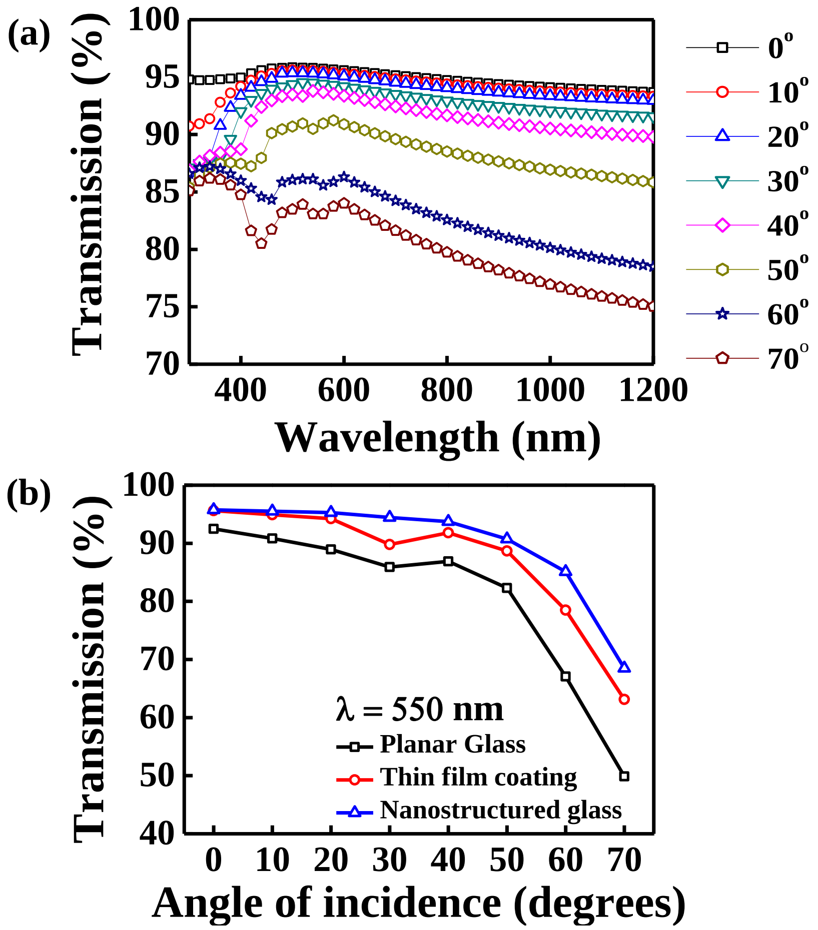

Figure 4.3 (a) Optical transmission of a nanostructured layer at normal incidence, (b) Comparison of optical transmission between planar glass, thin film coating and nanostructured layer at a wavelength of 550 nm for several angles of incidence.

layer, which allows more light to be transmitted. As seen in figure 4.3(a), there is a decrement in the transmission spectrum in the lower wavelength regions.

Here, the period between the features (= 250 nm) becomes comparable to the grating equation defined before, which leads to scattering or reflection of incoming light. On the other hand, for other wavelengths, the period always satisfies the grating equation, thus providing an increased transmission of light.

4.3 Effect of Dimensional Parameters

The dimensions of the nanostructured layer must now be optimized to determine the final parameters which can provide maximum transmission both at normal and oblique angles of incidence.

Therefore, in this section, two different studies are described.

1) The effect of the height of the nanostructures on optical transmission (keeping the diameter constant as 100 nm and pitch as 250 nm).
2) The effect of the filling fraction of the nanostructures on optical transmission (keeping the diameter constant as 100 nm and height depending on the result from the previous study)

The effect of the height of nanostructures on the optical transmission of planar glass was also investigated. The height of nanostructure was taken to be 100 nm, 200 nm, 400 nm and 800 nm to cover a wide range of heights. Figure 4.4 shows the results.

It can be seen from figure 4.4(a) that planar glass shows an optical transmission of ~ 92% over a wide range of wavelengths. Nanostructured glass with 200 nm height nanostructures shows a maximum improvement of ~93.5-95% over the entire wavelength range. However, nanostructures with height 100 nm and heights 400 nm and 800 nm show reduced transmission and interference patterns respectively which might be due to scattering of the incident light. This effect of scattering reduces the effective transmission of nanostructured surfaces.

Figure 4.4(b) presents the transmission behaviour of nanostructured layers of different heights at a wavelength of 550 nm. This particular wavelength is chosen because it has the highest number of useful photons in the solar spectrum for silicon solar cells. It can be clearly seen that nanostructures of height 200 nm present an omnidirectional improvement in transmission of planar glass. In addition, nanostructures of 400 nm height also exhibit improvement where their transmission behaviour is quite near to the nanostructures of 200 nm height. Therefore, 200-400 nm would be an optimized height of nanostructures for antireflection behaviour in planar glass.

Following these results, the effect of filling fraction on the optical transmission of planar glass was studied. In this case, the height of

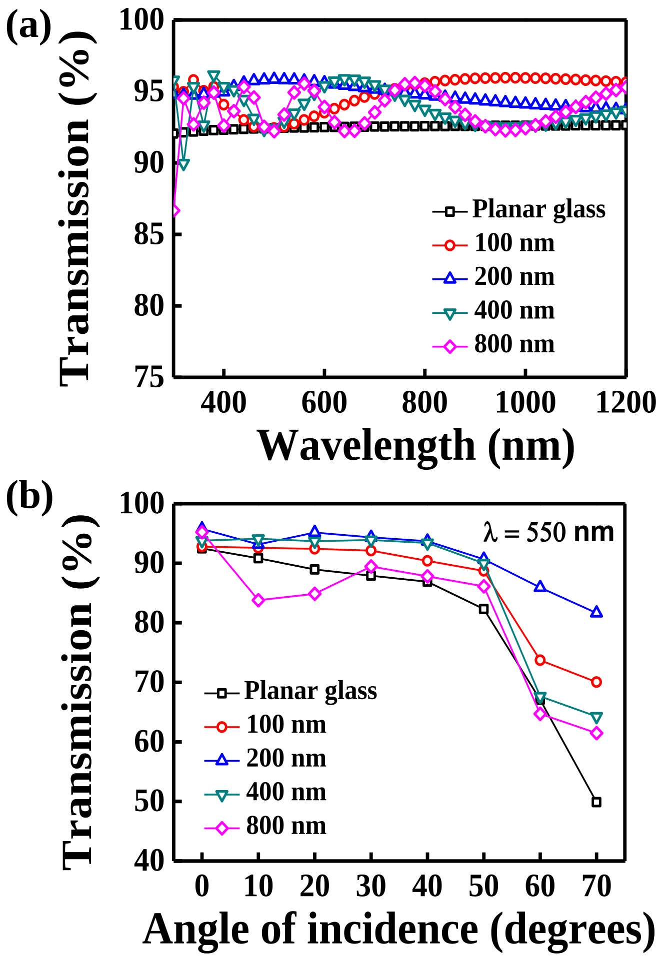

Figure 4.4 (a) Optical transmission of nanostructured layer with different heights of nanostructures, (b) Optical transmission of nanostructured layer with different heights of nanostructured at several angles of incidence for a wavelength of 550 nm.

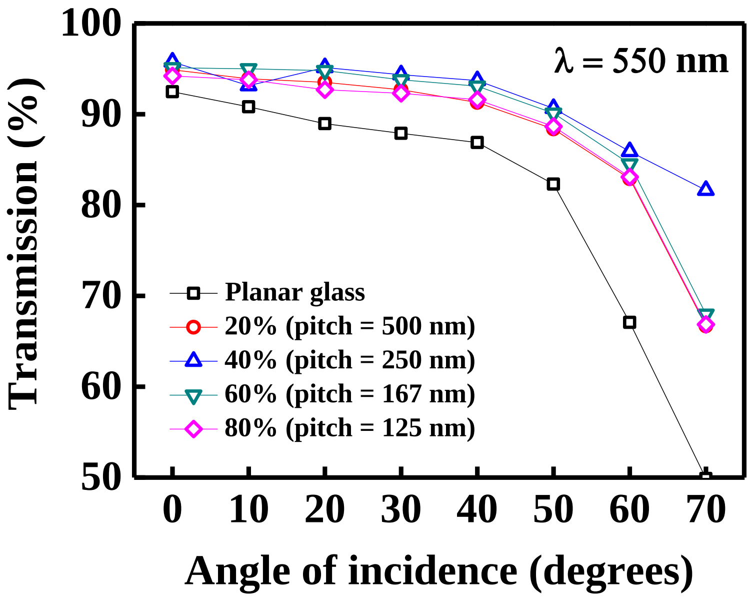

Figure 4.5 Optical transmission of planar glass and nanostructured surface with fixed height and diameter of 200 nm and 100 nm respectively with varying filling fraction.

nanostructures and diameter of nanostructures were kept fixed at 200 nm and 100 nm respectively. However, the change in filling fraction changes the spacing between the adjacent nanostructures. Therefore, filling fraction of 20%, 60% and 80% were considered in addition to a 40% filling fraction already studied before for nanostructures of height 200 nm where the pitch was 250 nm.

Figure 4.5 presents the transmission behaviour of 200 nm height nanostructures with different filling fractions for a wavelength of 550 nm.

It can be seen from the figure above that the nanostructures of height 200 nm exhibit maximum transmission behavior with a 40% filling fraction, i.e. with a spacing of 250 nm. However, a 60% filling fraction also provides improvement in optical transmission which is quite close to 40%.

Therefore, optimum parameters for nanostructured layer to provide antireflection properties in planar glass are the height = 200-400 nm, the diameter = 100 nm and the pitch = 167-250 nm.

4.4 3D Simulation of Nanostructured Glass

It is essential to conduct simulations in 3D since it gives a better description of the behaviour of the structure. In this section, 3D simulations of nanostructures on planar glass are carried out. The dimensional information has been set according to the experimental data which will be discussed in Chapter 5 (figure 5.2(d)). Previously, periodic nanostructures have been considered in simulation, but this section takes random nanostructures into consideration. The randomness is in the spacing and diameter of the nanostructures but the height remains fixed.

It has been observed in the experimental data after dewetting of Ni nanoparticles, that the average diameter of nanoparticles and hence nanostructures is 100 nm with an average spacing of 80-200 nm. The distribution profile of the diameter follows a Maxwell-Boltzmann distribution. Following this data, a stochastic structure with nanostructures on glass was simulated as shown in figure 4.6 which follows the same distribution as that measured experimentally.

Figure 4.7 presents the optical transmission of stochastic nanostructures with fixed heights of 200 nm and 400 nm.It can be seen from figure 4.6 that planar glass exhibits an optical transmission of ~92% as was seen with 2D simulations also. The stochastic nanostructures also show improvement in optical transmission when simulated with 200 nm height nanostructures showing a clear improvement over the wide range of wavelengths. There is suppression of transmission at lower wavelengths which may be due to the scattering effects. Hence, stochastic nanostructures also provide improvement

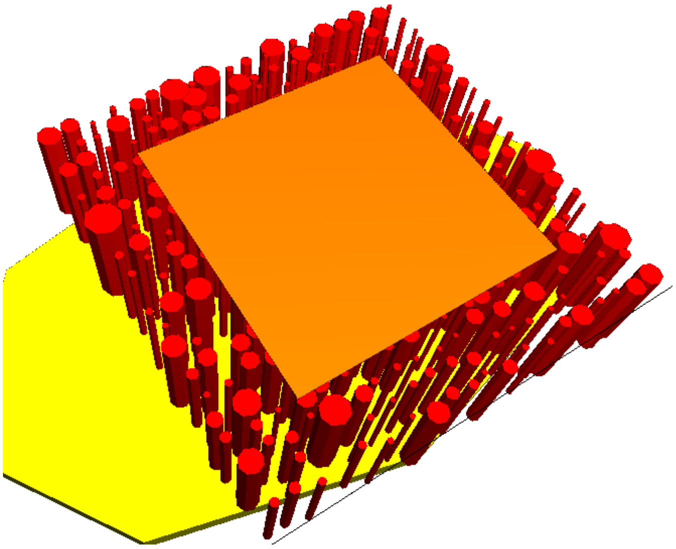

Figure 4.6 Stochastic structure (in diameter and spacing) with fixed height on planar glass for 3D simulations. The yellow base represents the glass substrate and red cylinders represent the sub-wavelength structures. The dark yellow coloured rectangular box represents the Gaussian source. The detector is directly below the source and cannot be seen in this figure.

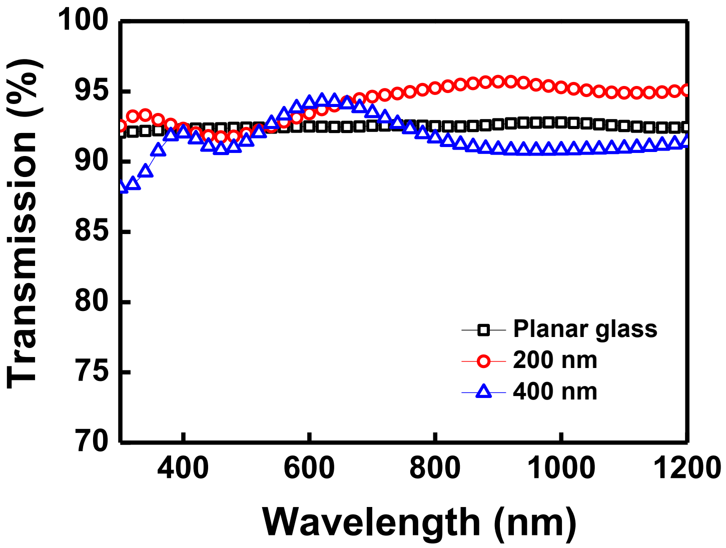

Figure 4.7 Optical transmission of planar glass and nanostructured glass of heights 200 nm and 400 nm, all simulated as 3D structures.

in transmission similar to periodic structures, thus potentially lowering fabrication costs.

4.5 Conclusions

Simulations have been performed to confirm the broadband and omnidirectional effects of nanostructures. According to effective medium theory, the nanostructures or sub-wavelength structures can be considered as a homogeneous media with an effective refractive index, which is determined by the filling fraction. The advantage of nanostructures over single layer coatings has been shown. Additionally, the effects of nanostructure height and filling fraction have also been studied. It has been shown that optimum dimensions of nanostructures for excellent antireflection effect are those with height = 200-400 nm, diameter = ~100 nm and pitch = 167-250 nm. Moreover, the simulations have also been carried out in 3D, giving an insight into the practical results that can be obtained. The simulations showed that stochastic nanostructures also provided superior transmission performance similar to the periodic structures. Therefore, the development of nano-fabrication techniques must be explored to realize the sub-wavelength structures with graded index profiles. This is the subject of the next chapter.

5. Improvement in Omnidirectional Transmission

5.1 Introduction

Stochastic nanostructured surfaces have shown similar improvement as the periodic nanostructured surfaces to enhance the optical transmission of planar glass. This chapter focuses on the creation of stochastic nanostructures on a glass substrate and then a study has been carried out to understand their omnidirectional behaviour to improve overall efficiency of solar modules.

Borosilicate glass (Borofloat 33, Schott Glass) of area 40 cm^2 was used for various experiments in this thesis. This particular glass from Schott is a transparent colourless glass with low iron content. Its excellent transparency in a wide electromagnetic spectrum has made this glass ideal as a front cover for many types of floodlights, high-power spotlights and sunbeds. Borofloat 33 glass also exhibits low inherent fluorescence [216] combined with low roughness surface quality and homogeneity which has allowed using this particular glass for optics, optoelectronics, photonics and analytical equipment.

The first step towards fabricating any device in the semiconductor industry is to clean the substrate on which the device is being fabricated. The cleaning recipe of borosilicate glass substrates is summarized below:

1) The glass substrates were immersed in HNO_3 for nearly 15 minutes to remove the metallic and non-metallic impurities from their surfaces.

2) The glass substrates were then immersed in deionized (DI) water for 5 minutes to neutralize the acid from their surfaces.

3) Then the glass substrates were ultrasonicated in acetone and isopropyl alcohol IPA for 10 minutes each.

4) After ultrasonication, the glass substrates were washed with a streaming jet of DI water and blown dry using a nitrogen gun. Once the glass substrates were dry, they were placed in an oven at a temperature of 100 °C for 10 minutes to allow evaporation of any water droplets still on the surface.

The fabrication process of creating nanostructures on glass has been discussed in chapter 3 with different experimental parameters stated in every section of fabrication and characterization tools. Figure 5.1 summarizes the fabrication process. A thin film of Ni (10 nm) was deposited on the glass substrate using an electron beam evaporator. Then, the Ni coated glass substrate was subjected to annealing at 600 °C for 5 mins using RTP. The rapid annealing of the Ni film caused the thin film to break into nano-islands/nanoparticles which were used as a mask for the subsequent etching process. The breaking of the thin film of Ni into nanoparticles was due to dewetting. ICP-RIE was employed later to etch the glass substrates to achieve nanostructures of desired height, and the remaining Ni nanoparticles were removed using HNO_3.

5.2 Fabrication results

Thin films when deposited by physical vapour deposition tools are generally metastable in the as-deposited state and usually break into an array of islands when subjected to heat. This phenomenon of breaking of the film or agglomeration of thin film after heating is known as dewetting. Dewetting can occur well below the film's melting temperature while the film remains in the solid state. The physical principle behind dewetting is the minimization of the

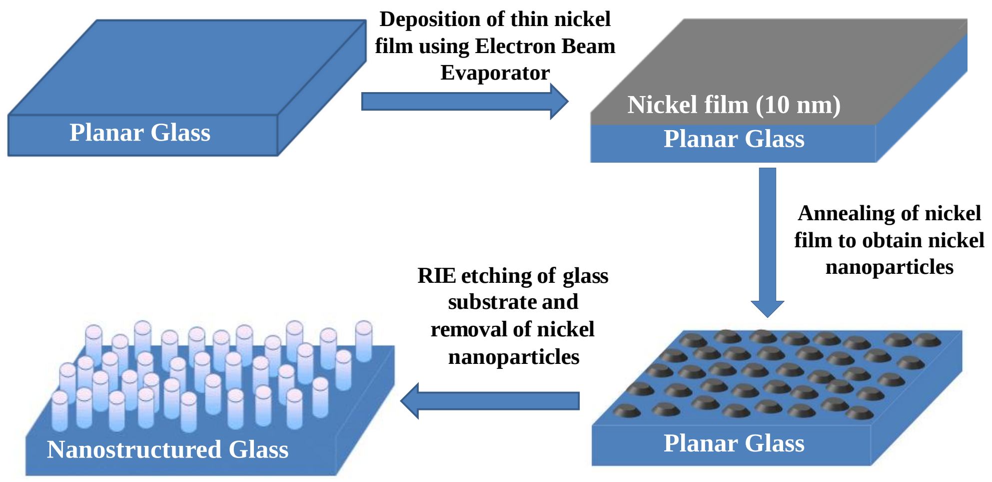

Figure 5.1 Schematic of the fabrication process of nanostructured glass.

total energy of the free surfaces of the film and substrate, or of the film-substrate interface. The thickness of the thin film determines the dewetting rate and usually it increases with decreasing film thickness [217].

Dewetting of thin films has its own advantages and disadvantages. Dewetting has been a great issue for the integrated circuits industry where dewetting of metal silicides and silicon-on-insulator has been of particular concern [218]. Dewetting also leads to the failure of many microdevices, especially when high-temperature operation is required. On the other hand, dewetting has been advantageous where it has been purposely employed to make particles and interconnected structures [219]. Dewetting is used to make particle arrays in sensors and for use as catalysts for growth of carbon nanotubes [220] and semiconductor nanowires [221]. It has also been used to form elements in electrical memory devices [222] and also has potential applications for creating nanocrystals for optical and magnetic devices.

The surface energy of the deposited film, substrate and interface between the film and substrate also plays a role in defining the dewetting property. Thin films are formed under conditions for which atomic motion is limited and non-equilibrium structures are obtained. This is generally true for films formed through vapour deposition techniques, thus, the films formed are unstable, or at best metastable. This leads to a lower interfacial adhesion between the film and substrate. Since these films are in a non-equilibrium energy state, they tend to stabilize when heated and spontaneously dewet to form islands at certain heating or annealing temperatures. The process of dewetting either occurs at pre-existing holes or at film edges or requires formation of new holes. These holes in the deposited film initiate the dewetting process, thus, breaking the film into islands. Because, dewetting requires atomic transport, the rate of dewetting is strongly temperature dependent.

A simple explanation of dewetting can be provided by the Young-Laplace equation based on the concept of surface energy. For islands with isotropic surface energy per unit area γ_f, on a rigid substrate with surface energy per area, γ_s, energy minimization for a fixed volume is given by Young-Laplace equation,

$$\boldsymbol{\gamma_s = \gamma_i + \gamma_f \cos\theta} \qquad \text{Equation 5.1}$$

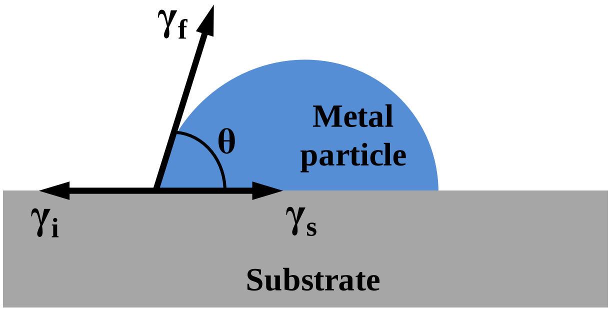

Figure 5.2 Schematic illustration of equilibrium film morphology when the equilibrium contact angle is non-zero.

where γ_i is the energy per unit area of the island-substrate interface and θ is the equilibrium contact angle. Two cases arise from this equation which determines the resulting dewetting process.

1) If $\gamma_s > \gamma_i + \gamma_f$, the deposited film is stable and will not dewet.
2) If $\gamma_s < \gamma_i + \gamma_f$, the deposited film will be in an unstable state, and will dewet to achieve the nearest equilibrium state depending on the rates of the necessary kinetic process.

Moreover, the dewetting of thin films is also governed by thermal strain [223]. As discussed before, thin films are always in a state of mechanical stress. When heated on substrates, thin films will experience a strain due to thermal mismatch, which is given as

$$\boldsymbol{\epsilon_T = \int_{T_0}^{T} (\alpha_s - \alpha_f) dT + \varepsilon_0 \approx (\alpha_s - \alpha_f) \Delta T + \varepsilon_0} \qquad \text{Equation 5.2}$$

where α_s and α_f are the thermal expansion coefficients of the film and substrate, respectively, and ΔT is the change in temperature from the temperature at which the strain was ε_0.

The main goal of this fabrication process was to create nanostructures on the surface of glass substrates. To create such structures, a metal template was required in the form of a nanoparticle mask. This mask could be created using any metal film depending on its adhesion to the glass substrate which depends on the surface energy of metal and glass materials as well as the interaction between the two materials. The higher the surface energy, the greater the molecular attraction and vice versa.

The table below lists the surface energy of various metals that were taken into consideration while designing this fabrication process.

Table 1 Summary of surface energy values of different metals and glass.

Name of metal	**Surface energy (mJ/m^2)**
Lead (Pb)	458
Tin (Sn)	526
Magnesium (Mg)	642
Zinc (Zn)	753
Silver (Ag)	1250
Gold (Au)	1500
Copper (Cu)	1830
Titanium (Ti)	2100
Chromium (Cr)	2300
Nickel (Ni)	2450
Glass (SiO_2)	250-500

Depending on adhesion conditions, Ni was the most suitable metal since it has the highest surface energy and can form a stable thin film on glass. To create a nanoparticle mask on glass, a metal with a high surface energy was required but with a low melting temperature so that the nanoparticle mask could be created with rapid thermal annealing in a reasonable period of time. Nickel provided a lower melting temperature (1455 °C) than Ti (1668 °C) and Cr (1907 °C). Therefore, Ni was chosen for this fabrication process.

Adhesion of the film over time also depends on the oxygen affinity of the metal since it governs bonding with glass. A study was conducted by Benjamin and Weaver [234] where the adhesion of different metal films was studied over time using a load test (a scratch test). It was seen that Ni formed oxides readily and had good bonding with glass.

While in the process of testing Ni films in this thesis work, Ag and Au films were also tried. It was seen that their adhesion to glass was poor when thin and these films delaminated after the deposition process. These were not investigated further.

As stated before, the Ni thin film was subjected to a temperature of 600°C for 5 minutes which agglomerated the film into numerous nano-islands on the surface of the glass substrate. Figure 5.3(a) shows the dewetted Ni film.

Figure 5.3(b) shows the nanostructures etched into glass by the RIE etching process. It can be seen that the nanostructures are of equal height and distributed uniformly across the sample. The nanostructures had an average diameter of 100 nm with a pitch varying from 80-150 nm. Figure 5.3(a) is processed using MATLAB to calculate the diameter of every particle by calculating the pixel count in every particle. The pixel count is then converted

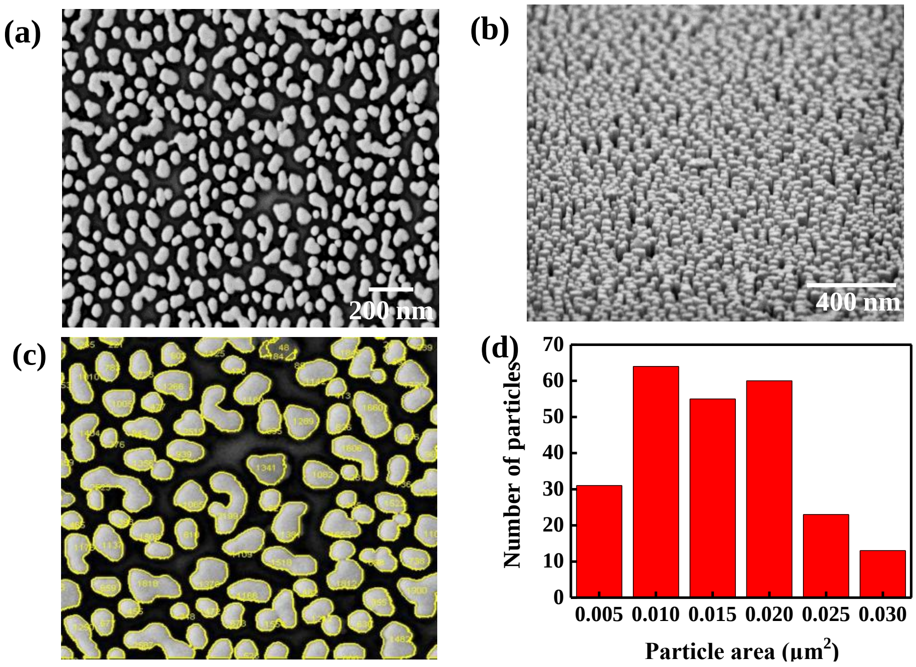

Figure 5.3 (a) SEM image of nickel nanoparticles on glass after annealing, (b) Cross-section view of nanostructures on glass after etching and Ni removal, (c) Zoomed view of MATLAB processed image of (a), (d) Particle distribution.

into the particle diameter by offsetting it against the pixel dimensions of the scale bar of SEM image. Figure 5.3(d) shows the particle diameter distribution. It can be seen that the distribution follows the Maxwell-Boltzmann distribution. This distribution was used to simulate the transmission of a 3D structure in chapter 4.

5.3 Spectral Transmission of Nanostructured Glass Samples

Optical transmission measurements were conducted on the nanostructured glass substrates to understand their antireflective and omnidirectional characteristics.

Figure 5.4 shows the specular transmission of planar and nanostructured glass samples as a function of the wavelength. It can be observed that nanostructured glass with 200-nm high nanostructures exhibits a maximum transmission of ~95.5% at normal incidence in comparison to planar glass which has an optical transmission of nearly 92%. The other nanostructured glass samples also proved to be efficient in comparison to planar glass. This is in agreement with the simulation results reported in Chapter 4. The transmission is seen to drop at lower wavelength regions during direct transmission measurement which is attributed to the scattering of incident light due to sub-wavelength structures as explained in section 3.4.2 in chapter 3. This scattered portion of light is the diffused transmission component which has been studied in chapter 7.

The simulation results shown in Chapter 4 also concluded that nanostructures were also efficient at oblique angles of incidence. Similar results can also be observed in experimental results. Figure 5.5 shows the optical transmission for planar and nanostructured glass substrates as a function of angle of incidence at a 550-nm wavelength. It is observed that nanostructured glass with 200-nm high nanostructures exhibits superior performance up to a 60°-65° incident angle.

Figure 5.6 shows optical transmission of the planar and nanostructured glass samples as a function of wavelength and angle of incidence. The contour lines show different levels of optical transmission (%). The dotted lines represent the value of the incident angle above which the specular transmission reduced for the planar glass sample.

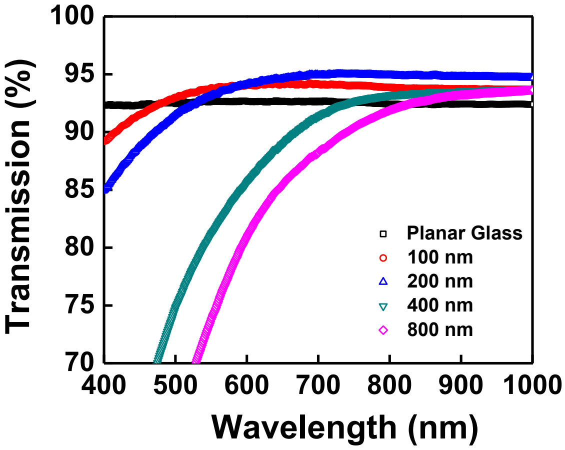

Figure 5.4 Optical specular transmission at normal incidence (0°) for nanostructured glass with nanostructures of varying height vs. Wavelength spectrum (400-1000 nm).

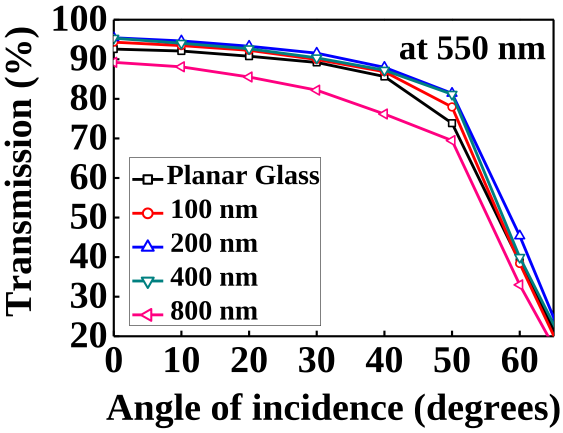

Figure 5.5 Optical specular transmission for nanostructured glass with nanostructures of varying height at a 550-nm wavelength vs. Angle of incidence.

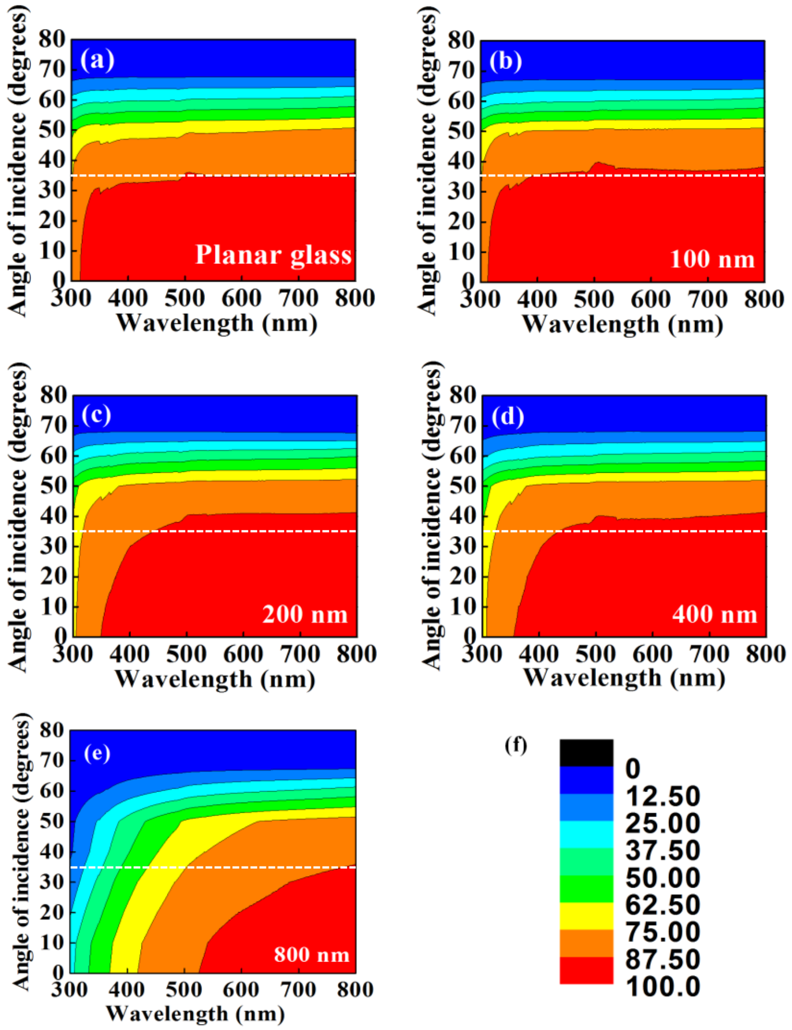

Figure 5.6 (a-e) Contour images of optical specular transmission as a function of wavelength and incidence angle of planar glass and nanostructured glasses of different heights. Figure 4(f) shows the contour map value (%) for different colour scales.

It can be seen in figure 5.6 that planar glass shows an optical transmission greater than 87.5% up to a 30°-35° angular range, and it drops quickly below 10% at 80°. The range of maximum optical transmission (> 87.5%) is extended beyond 35° (< 40°) for 100-nm nanostructures. 200-nm nanostructures show transmission greater than 87.5% up to 40° of angular incidence, and the level of 75-87.5% transmission is extended up to 55° (< 60°), over the whole 300-800 nm spectral range. The 400-nm nanostructured glass sample also exhibits similar characteristics as the 200-nm sized nanostructured glass sample, with optical transmission greater than 87.5% up to a 40° incident angle but the transmission is reduced at greater angles of incidence. These fabricated nanostructured glass samples exhibit maximum transmission for large oblique angles of incident light, thus, promising superior photocurrent generation over an entire day.

For Figure 5.6(e), transmission decreases at short wavelengths and the plateau of maximum transmission shifts towards longer wavelengths showing the limitations of nanostructure height in the visible range, due to scattering at short wavelengths.

5.4 Nanostructured Glass as Packaging Cover of Solar Modules

To further understand the effect of nanostructured module glass on the underlying solar cells, mini modules were prepared and were tested in a solar simulator with 1 sun AM 1.5G illumination. Figure 5.7(a) shows a photograph of the mini solar modules fabricated for this study. The solar cells were encapsulated using an industrial laminator system at Solar Energy Research Institute of Singapore (SERIS). The planar glass and nanostructured glass substrates were used as a superstrate in the encapsulation process. The solar cell was sandwiched between two layers for the encapsulant. EVA, an industrially accepted encapsulant was used for making the mini modules. A Tedlar backsheet was used at the non-illuminated or backside of the mini modules and it acts a barrier for humidity and corroding species. Figure 5.7 (b) shows a cross-sectional image of the encapsulated cells. Before conducting I-V testing of the mini solar modules, the white portion of the modules was covered with a black mask in order to avoid any back reflections leading to a significant change in J_{sc}.

The average values of the parameters of the solar cell of 39.75 cm^2 area, measured at 1 sun were as follows: η = 18.5%, V_{oc} = 0.57 V, and J_{sc} = 40.2 mA/cm^2 and fill factor (average) = 74.4 %. Figure 5.8 shows various solar cell parameters (V_{oc}, J_{sc}, P_{mpp}, and η) plotted with respect to nanostructure height, as measured at normal incidence. The J_{sc} of the solar cell with a planar glass cover was 37.5 mA/cm^2 which increased to 38.9 mA/cm^2 for a 200-nm sized nanostructured glass cover. With an increase in the nanostructure height beyond 200 nm, J_{sc} reduced, which is attributed to transmission loss of incident light due to scattering. The solar cell efficiency and the maximum output power also exhibited the same trend.

The power conversion efficiencies of the nanostructured solar modules were higher than those of the planar glass module, with the 200-nm module exhibiting an absolute increase of 1.0 %. It can be noticed from Figure 5.8(d) that the 200-nm sized nanostructured glass module exhibited an efficiency of 16.5% (V_{oc} = 0.569 V, J_{sc} = 38.9 mA/cm^2, FF = 74.41 %) while the planar

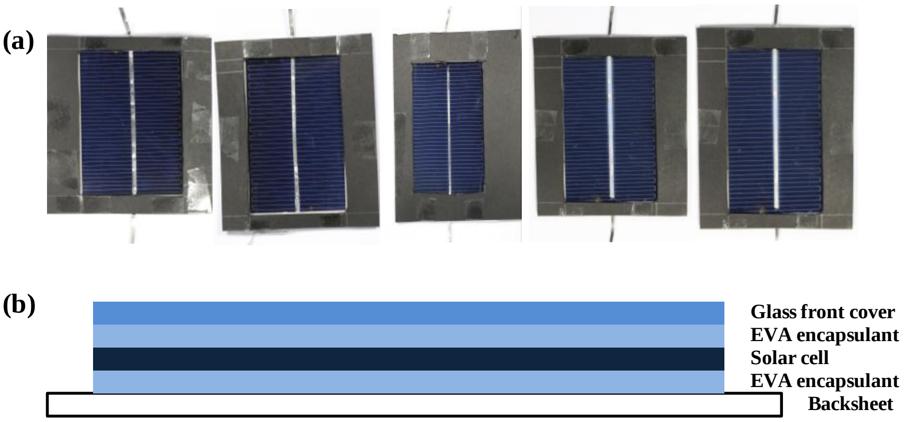

Figure 5.7 (a) Mini solar modules fabricated with planar and nanostructured glasses as their packaging cover, (b) Cross-sectional schematic of the encapsulated solar cells.

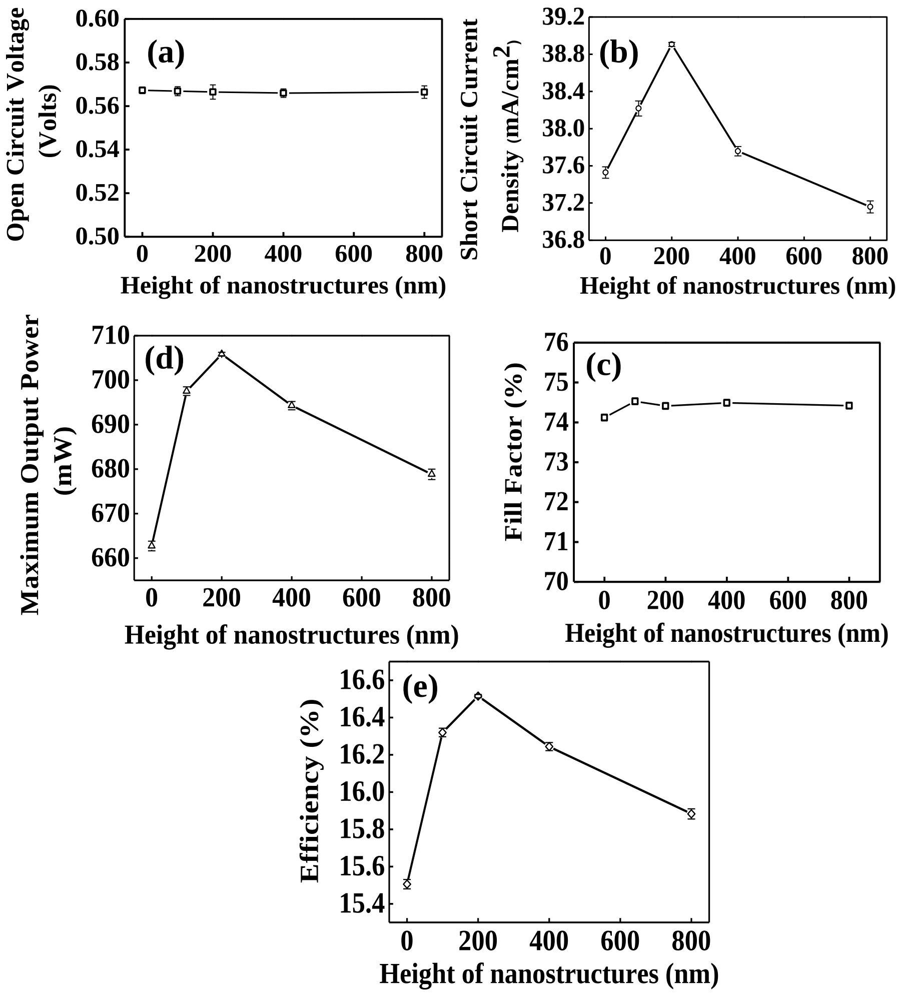

Figure 5.8 Variation of various solar cell parameters (a) open circuit voltage (V_{oc}), (b) short circuit current density (J_{sc}), (c) output power (P_{mpp}), (d) fill factor (FF) and (e) efficiency (η), with the height of nanostructures at normal incidence of light.

glass module exhibited an efficiency of 15.5% (V_{oc} = 0.569 V, J_{sc} = 37.5 mA/cm^2,FF = 74.12 %). The significant improvement in the power conversion efficiency is primarily attributed to an increase in the short circuit current density between the planar glass and nanostructured glass solar modules. The results obtained are agreement with the results reported by Verma et al. [224] and Son et al. [236].

Figure 5.9(a) shows the variation of J_{sc} as a function of angle of incidence for solar modules with planar and nanostructured glasses as their packaging covers. The x-axis shows both the positive and negative angular range of the

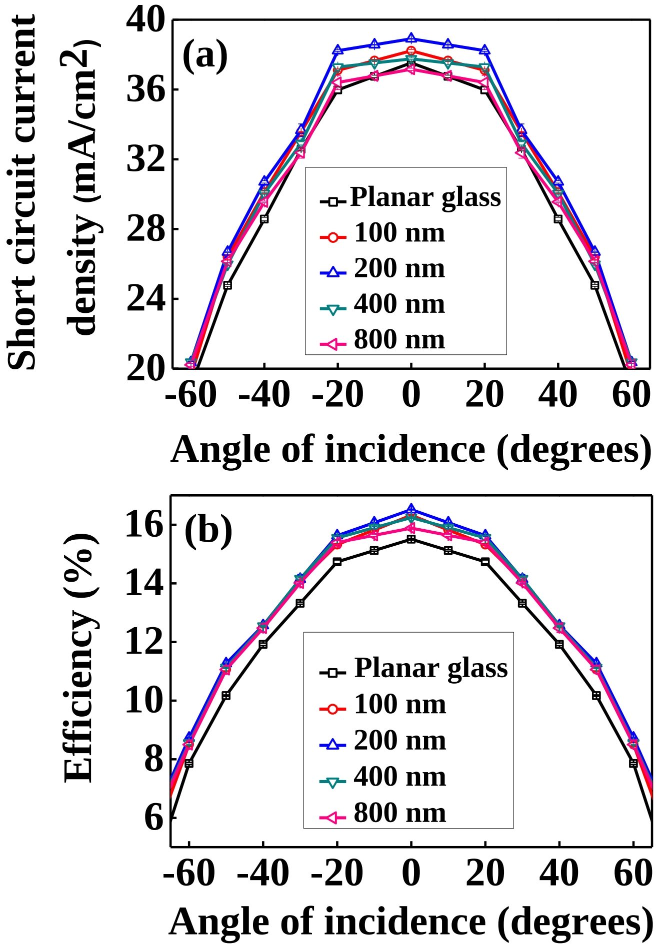

Figure 5.9 (a) Variation of short circuit current density as a function of angle of incident light for solar modules with planar and nanostructured solar as their cover, (b) Variation of efficiency as a function of angle of incident light for solar modules with planar and nanostructured solar as their cover.

sun's movement, using normal incidence of solar radiation as a reference. Similarly, Figure 5.9(b) plots the efficiency of planar and nanostructured solar modules as a function of incident angle. The 200-nm nanostructured solar module gave a maximum absolute increase of 1.0 % at normal incidence and the corresponding gain in J_{sc} was observed over a 120° cone of solar reception. These results are in agreement with the optical transmission measurement taken with the spectrophotometer discussed earlier in Figure 5.6, which showed that a 200-nm nanostructured glass substrate had maximum transmission over a wide spectral and angular range.

5.5 Conclusions

In this chapter, the main aim of studying the antireflective properties of nanostructured glass has been systematically investigated. The nanostructures fabricated via a non-lithographic method exhibited antireflection properties due to a gradient change in the effective refractive index. This allowed them to show an improvement of 3.4% in the optical transmission for 200-nm sized nanostructures at normal incidence of light, see Figure 5.3. A significant improvement has also been observed in solar modules packaged with the nanostructured glass, with a maximum improvement shown with 200-nm sized nanostructures; a power conversion efficiency improvement of 1% (absolute increase) relative to a solar cell module fabricated with standard planar glass was observed. An omnidirectional study showed that this improvement was present over a wide 120° angular range of solar incidence as compared to a planar glass module. Omnidirectional antireflection is important in fixed-mount solar module installations, and promises increased power conversion efficiency over an entire day.

When planar or nanostructured glass covers are used as packaging covers of solar modules, their durability to sustain practical conditions needs to be studied and tested. Therefore, the next chapter discusses outdoor performance of planar and nanostructured glass samples in the tropical weather of Singapore.

6. Outdoor Performance and Durability of Nanostructured Glass

6.1 Experimental Details

The nanostructured glass substrates used for outdoor testing were fabricated with the same non-lithographic process described in Chapters 3 and 5. In order to evaluate the outdoor performance and durability of planar and nanostructured glass samples, outdoor exposure tests were carried out for a testing period of 3 months (12 weeks) on the roof of a 35-m building at the National University of Singapore. Planar and nanostructured glass samples were mounted flat (0°) and also inclined at 10° and 20° so as to simulate the conditions of solar modules operating in equatorial regions. Since it is already known that tilting helps in reducing the dust accumulation on solar modules, it was essential to test the fabricated nanostructured samples at tilted angles.

One of the major concerns when mounting solar panels with thin-film coated or nanostructured glass covers is their durability. The durability of the outdoor mounted samples was assessed after the testing period by carrying out morphological characterization of the nanostructured glass samples with an SEM. Furthermore, performance analysis was carried out by analyzing the dust accumulation on the glass samples using an SEM and an optical microscope. Optical specular transmission measurements were carried out over a spectral range of 400-1000 nm on the outdoor exposed samples. These optical measurements were carried out every 2 weeks at normal incidence with a UV-Visible spectrophotometer. The surface characteristics of the outdoor mounted glass samples were also evaluated using contact angle measurements at room temperature. The values reported are the average of five measurements carried out at different locations on each sample.

Mini solar modules fabricated for omnidirectional measurements discussed in chapter 5 were also tested outdoors. Based on the results obtained from the outdoor exposed glass substrates, the performance of the solar modules was tested for 5 weeks. The inclination angle of the solar modules was chosen based on the best performers from the earlier outdoor exposure experiments on planar and nanostructured glass samples. I-V testing of the solar modules was carried out after every 5 days for a total of 5 weeks.

6.2 Pre-outdoor Exposure Results

A separate set of nanostructured and planar glass samples were fabricated to conduct the outdoor testing. Therefore, it is very important to test their optical transmission before exposing them outdoors. Figure 6.1(a) presents the optical transmission spectrum at normal incidence for planar and nanostructured glass samples. The optical transmission results obtained for these set of samples were similar to the previous set of samples, thus, showing the repeatability of the fabrication process. It is observed that 200-nm high nanostructures exhibited maximum improvement over the whole 400-1000 nm wavelength spectrum, which is in agreement with the results reported in previous chapter.

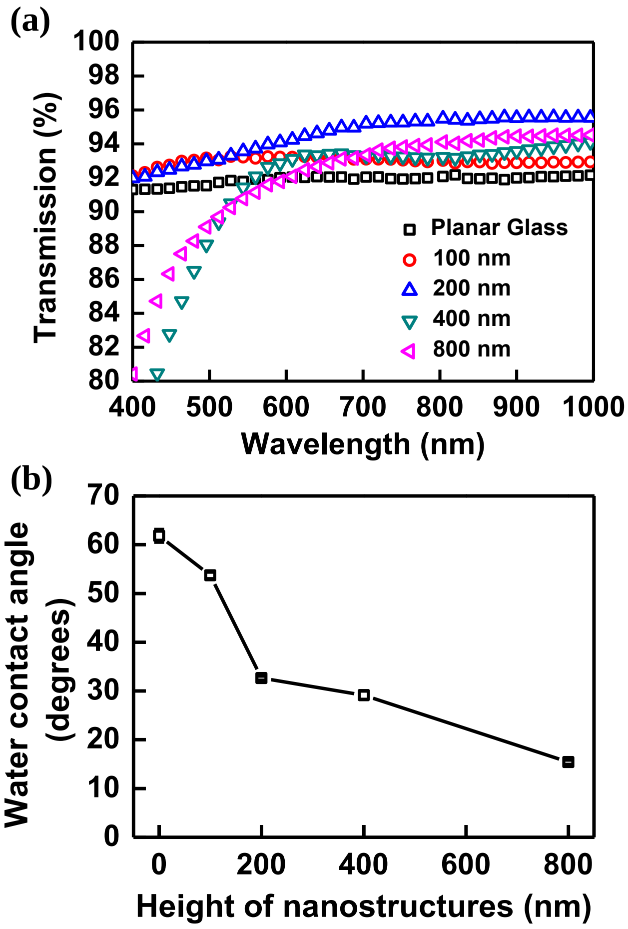

Figure 6.1 (a) Optical transmission spectra for glass samples of different nanostructure heights, and (b) Variation of water contact angle with the height of nanostructures on glass.

The antireflective properties of the nanostructured surfaces have encouraged convergence between self-cleaning structures and antireflective structures. Water contact angles (WCAs) of the planar and nanostructured glasses were measured as shown in Figure 6.1(b). It was seen that planar glass exhibited a WCA ~ 60° whereas the WCA reduced upon nanostructuring. The decrease in WCA became profound with an increase in the height of the nanostructures. Similar results have also been reported in other work [224, 225].

It has been shown in the literature that the WCA should increase with an increase in the roughness of the substrate according to the Wenzel and Cassie-

Baxter wetting models, but the fundamental reason of observing an increase in hydrophilicity (or decrease in WCA) here is the capillary effect [226]. When the water droplet comes into contact with the glass nanostructures, water penetrates into the gaps of two adjacent pillars and a thin solid/liquid composite film is formed which makes the water droplet spread easily.

6.3 Optical and Water Contact Angle Measurements after Outdoor Exposure

In order to test the practical long term performance of the planar and nanostructured glass substrates, they were exposed outdoors for a 3-month period. Figure 6.2 shows a photograph of the planar and nanostructured glass samples mounted flat and at inclined angles (10˚ and 20˚). The backsides of these glass samples were not covered, which might expose them to seeping water or dust. Therefore, before optical transmission measurements were carried out, the backsides of these glass samples were cleaned using a standard procedure with IPA, a cotton bud, DI water and N_2 gas. Figures 6.3(a), (b) and (c) present optical transmission with respect to the exposure time for planar and nanostructured glass samples for flat mounted and oblique mounted samples at a 600-nm wavelength. For flat-mounted samples, it was observed that the optical transmission of planar glass deteriorated from 92.5% to 87%, thus accounting for a ~5% decrease over 3 months.

In comparison, the nanostructured glass samples showed better performance with the best transmission of ~94.5% shown by nanostructured glass with 200-nm high nanostructures. The optical transmission of flat-mounted nanostructured glass samples also decreased after outdoor exposure with the least deterioration of ~2.5% shown by the 200-nm high

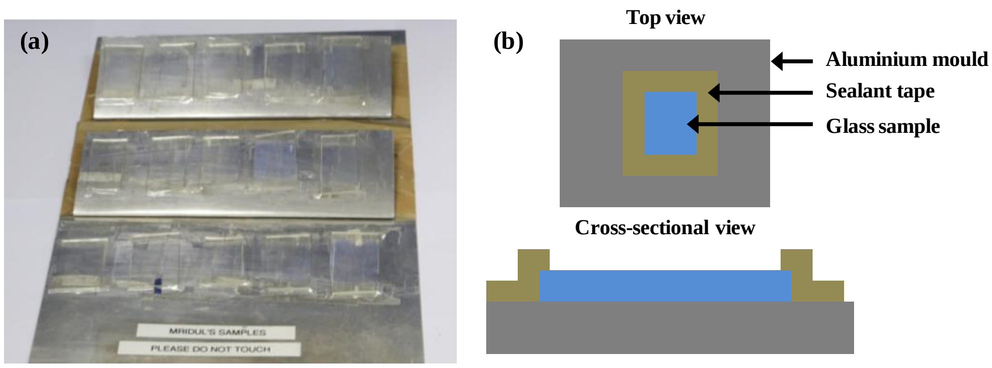

Figure 6.2 (a) Photograph of the planar and nanostructured glass samples mounted flat and at inclined angles, (b) Top view and cross-sectional view of the mounted samples.

nanostructured sample. Thus, the nanostructured glass samples showed a self-cleaning effect as compared to the planar glass sample. An abrupt decrease in the transmission was observed for the flat-mounted samples between weeks 4 and 6 due to less rainfall during this testing period (figure 6.3(e)). The decrease in optical transmission is due to the sticking of dust particles after water droplets evaporate from the surface over time. The effect of accumulation of dust particles on the glass samples can be seen from the variation in the error bar for various points in the transmission data for a particular sample.

The planar glass sample mounted at an inclination of 10° also showed similar deterioration in optical transmission as the flat-mounted planar glass sample. The nanostructured glass samples inclined at 10° showed no improvement in the optical transmission and their behaviour was similar to the flat-mounted control samples.

However, interesting results were obtained with the samples mounted at 20°. The planar glass sample showed similar deterioration in optical transmission as its flat mounted and 10° inclined control samples. However, the nanostructured glass samples showed better performance as compared to their control samples. The trend of decrease in the optical transmission was linear as compared to the flat-mounted and 10° inclined samples with the least deterioration shown by the 200-nm nanostructured sample of ~1.5%. This improvement in the self-cleaning effect can be due to the conditions favoured by the inclination angle.

Inclination has a profound effect on the self-cleaning behaviour which allows the flowing water to provide a sheeting effect, thus carrying the dust particles away more easily during rains. However, solar modules always have a mismatch between their lab tested efficiency and practical efficiency when they are mounted outdoors at the equator. Therefore, the obtained results of optical transmission in figures 6.3(a), (b) and (c) were further analyzed with the results reported in section 5.4 where the efficiency of solar modules was tested at different inclination angles. The inclination of solar modules at 10° and 20° decreases their efficiency by 0.5% and 1% respectively due to less illumination as an effect of different effective area of irradiation. Taking into consideration the offset created by optical transmission loss due to dust accumulation over a long term exposure period, the overall efficiency loss would be 4%, 3% and 2.5% for flat mounted, 10° and 20° inclined solar modules respectively. Thus, the self-cleaning effect provided by the 20° inclined nanostructured glass samples increases the overall efficiency of solar modules.

WCA measurements were also carried out for the planar and nanostructured glass samples every week after beginning outdoor exposure. Figure 6.3(d) presents the variation of WCA versus the exposure time for the flat-mounted and 20° inclined planar glass and 200-nm high nanostructured glass samples. It was seen that the flat-mounted and 20° inclined planar glass samples and 20° inclined nanostructured sample presented a significant variation in the WCA over the testing period. However, the nanostructured sample inclined at 20° presented less fluctuation. The reason behind such fluctuations can be attributed to the capillary effect. The accumulation of dust particles creates a certain roughness on the surface of the sample which leads to a variation in the surface morphology, thus inducing fluctuations in the WCA.

Figure 6.3(f) presents SEM images of 20° inclined nanostructured sample with 200-nm high nanostructures before and after outdoor exposure. It was observed that there was no change in the height of nanostructures which shows that the glass nanostructures are robust and appropriate for outdoor use. The decrease in the optical transmission and changes in WCA were solely due to the accumulation of dust particles on the surface of the samples.

6.4 Dust Accumulation Analysis on Outdoor Exposed Samples

To further understand the reason behind the reduction in the optical transmission for the planar and nanostructured samples, dust analysis was carried out for flat-mounted and 20° inclined planar glass and 200-nm high nanostructured glass samples. SEM and optical microscope images were obtained for them and then the images were analyzed using the free software Image J.

Figures 6.4(a) and 6.4(b) present optical microscope images for 20° inclined planar and 200-nm height nanostructured glass samples, respectively. Figures 6.4(d) and 6.4(e) present SEM images for 20° inclined planar and 200-

nm height nanostructured glass samples, respectively. It can be clearly seen from figures 6.4.1(a) and (d) that the planar glass samples are dirty compared to the 200-nm height nanostructured glass inclined at the same angle. Figures 6.4(c) and (f) present the dust analysis for flat-mounted (SEM and optical microscope images not shown here) and 20° inclined planar glass and 200-nm

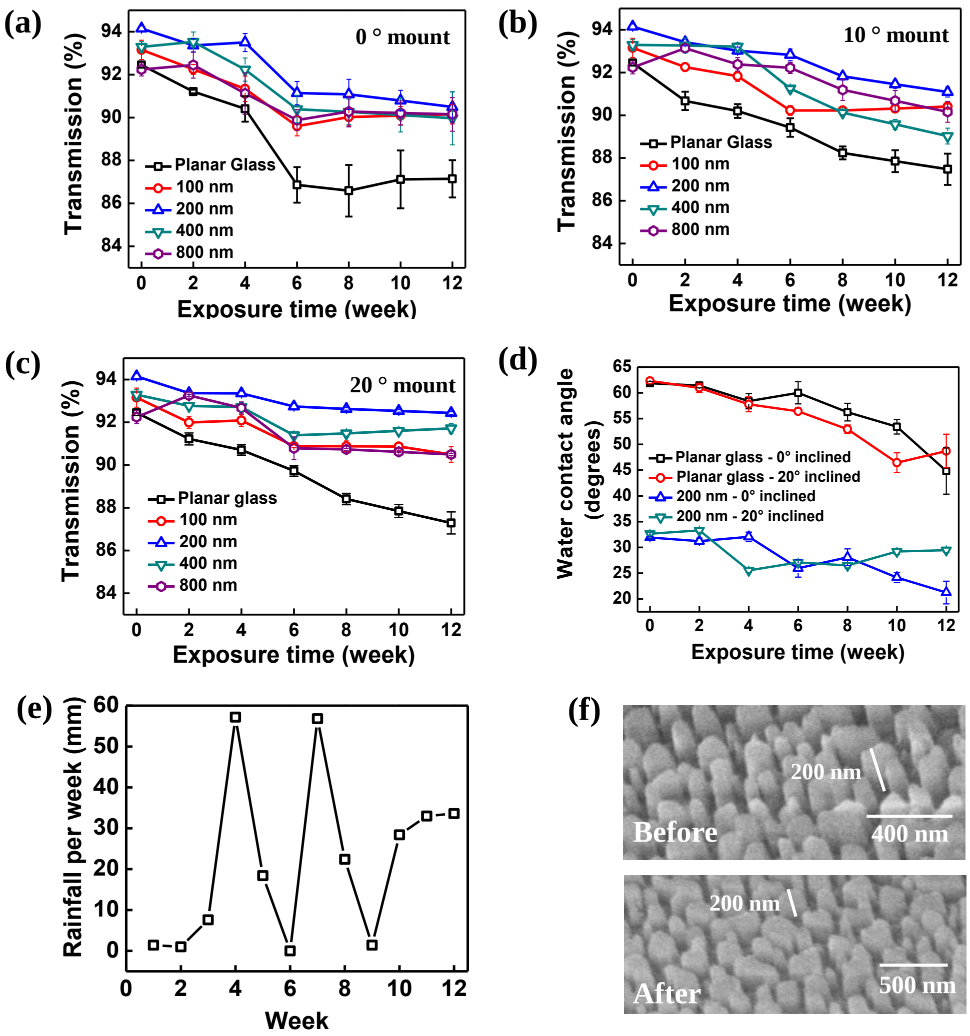

Figure 6.3 (a, b, c) Variation of the optical transmission (at 600-nm wavelength) of flat mounted and inclined planar and nanostructured glass samples with the outdoor exposure time in weeks (d) Variation of water contact angle for flat mounted and inclined planar and nanostructured glass samples with 200-nm high nanostructures, (e) Rainfall per week over the testing period, (f) SEM image of nanostructured glass sample with 200-nm high nanostructures before and after the outdoor exposure, respectively.

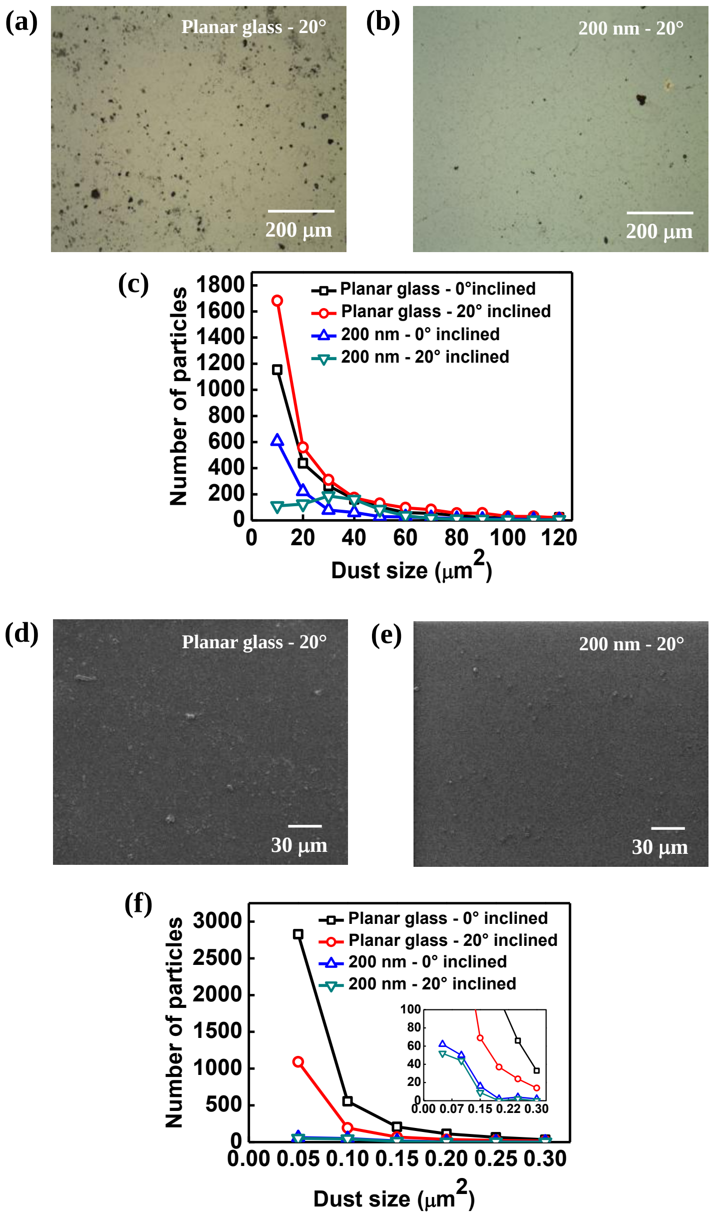

Figure 6.4 (a, b) Optical microscope images for 20° inclined planar glass sample and nanostructured glass sample with 200-nm high nanostructures after the long term outdoor exposure, (c) Number of particles on the surface of the planar glass sample and the nanostructured glass sample with 200-nm high nanostructures versus the particle/dust size in an area of 0.64 mm^2 after the long term outdoor exposure, (d, e) SEM images for 20° inclined planar glass sample and nanostructured glass sample with 200-nm high nanostructures captured after the long term outdoor exposure, (f) Number of particles on the surface of the planar glass sample and nanostructured glass sample with the 200-nm high nanostructures versus the particle/dust size in an area of 6400 μm^2 after the long term outdoor exposure.

height nanostructured glass, respectively. It can be clearly observed that the planar glass samples are affected more by the accumulation of dust compared to nanostructured glass sample which accounts for the deterioration of their optical transmission behaviour over long term outdoor exposure.

The phenomenon of deterioration of optical transmission can be explained on the basis of Mie scattering and Rayleigh scattering [227, 228]. The pattern of scattering depends on the wavelength of light and the particle size. It can be seen from figure 6.4(f) that the size of dust particles on the flat-mounted and the 20° inclined planar glass samples is mainly distributed around 0.05 μm^2 (~ 250 nm in diameter).

Rayleigh scattering is applicable to small nanometer-sized particles, scattering light in the forward and backward directions, whereas Mie scattering has no size effect and converges to the limit of geometric optics for large particles, thus scattering light mostly in the forward direction; forward scattering increasing with particle size. Since the dominant particle size on the planar glass samples is in the nanometer range, light is scattered according to the Rayleigh criterion, thus reducing the optical transmission for planar glass samples. On the other hand, large sized particles are predominant on the nanostructured glass samples which scatter light mostly in the forward direction according to Mie scattering. In this manner, the optical transmission of the nanostructured glass samples is less affected compared to planar glass samples.

6.5 Outdoor Exposure of Solar Modules

The planar and nanostructured glass samples exposed outdoors at an inclination of 20° exhibited less dust accumulation on their surfaces owing to their self-cleaning ability. Therefore, the solar modules were tested outdoors at an inclination of 20° (best performance from optical transmission results) as well.

Figures 6.5(a, b) represent the variation of the short circuit current density and efficiency of the solar modules with different packaging covers respectively as a function of the exposure time. It can be seen that the short circuit current density of the planar glass solar module reduces prominently by

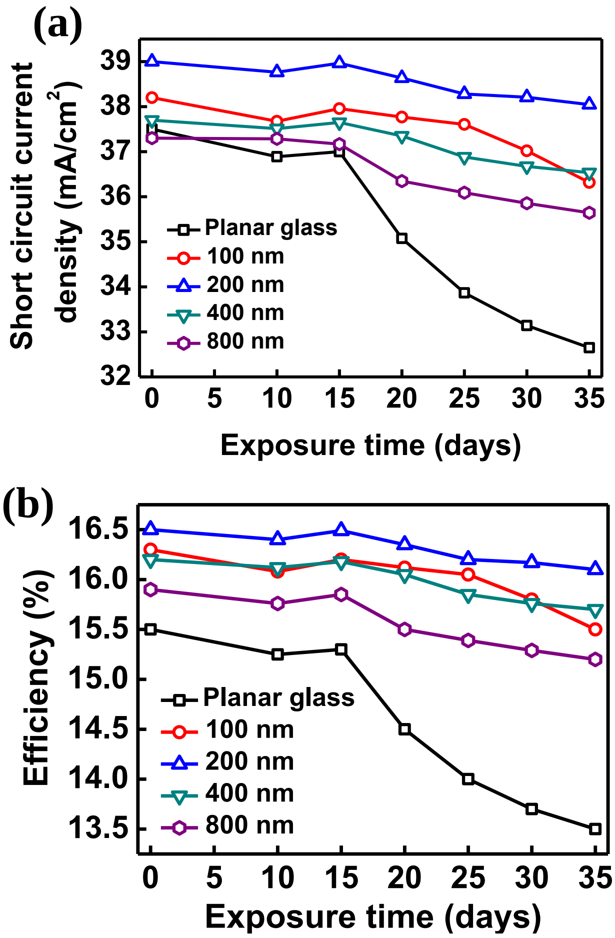

Figure 6.5 (a) Variation of short circuit current density with exposure time for planar and nanostructured glass solar modules, (b) Variation of efficiency with exposure time for planar and nanostructured glass solar modules.

~5 mA/cm^2 after an outdoor exposure of 5 weeks. A significant drop of ~2% (absolute) was also observed in the efficiency.

This reduction in the solar module parameters is obviously due to the accumulation of dust particles on the planar packaging glass. In comparison, the nanostructured glass solar modules showed better performance. Among the nanostructured samples, the best performance was observed for the nanostructured glass solar module with 200-nm high nanostructures on the packaging glass cover with a reduction in short circuit current density and efficiency by 1 mA/cm^2 and 0.3% respectively; thus providing self-cleaning and antireflective effects with increased power conversion efficiency for the underlying solar cell.

6.6 Conclusions

In this chapter, a successful and systematic study of the self-cleaning behavior, outdoor performance and durability of planar and nanostructured glass samples have been reported over an outdoor exposure period of 12 weeks. It was observed that inclination was required for the hydrophilic nanostructured glass samples for low dust accumulation and self-cleaning effect. The nanostructured glass sample with 200-nm high nanostructures on its surface provided superior antireflective and self-cleaning effects compared to a planar glass sample over the testing period. This particular nanostructured glass sample also provides the best performance when tested as the packaging cover of a solar module, with reduction in efficiency by only 0.3% over a testing period of 5 weeks. Thus, this practical demonstration of the self-cleaning and antireflective performance of nanostructured glass samples can find potential applications in outdoor optoelectronic devices such as solar modules without any application of chemical treatment or coatings to the system.

The nanostructured glass samples have shown a superior antireflective and self-cleaning performance as compared to planar glass. However, the nanostructured glass samples also suffer from optical transmission losses in the short wavelength region. This loss has been attributed to scattering but it would be appropriate if this phenomenon were studied in a systematic manner. This is the subject of the next chapter where scattering properties of planar and nanostructured glass samples are studied to determine the reason for the loss of incoming photons in the short wavelengths regime.

7. Optical Scattering by Nanostructured Glass

7.1 Introduction

In the field of PV, scattering studies are generally carried out for light-trapping structures especially for thin film solar cells [229]. These studies have been carried out for nanostructured and microstructured surfaces to understand the effect of their surface morphologies on the optical absorption in thin film solar cells fabricated on these textured glass substrates. However, such studies are not reported for crystalline solar modules where textured glass superstrates are used with texturing at the air/glass interface. It would be interesting to carry out scattering studies for these textured glass superstrates unlike glass/silicon interface of thin film solar modules, since it would allow a better understanding to guide more light into the underlying commercial textured solar cells. This would allow a better optimization of the design of textures on glass superstrates for crystalline solar modules.

In this chapter, scattering behaviour of stochastically arranged nanostructures on glass is reported experimentally by measuring the optical haze and angular resolved scattering. In addition, nanostructured glass substrates are employed as front covers of multicrystalline silicon solar modules and their external quantum efficiency (EQE) is measured and compared to that of planar glass covers.

7.2 Experimental Details

Figure 7.1 presents the SEM images of nanostructured glass substrates with 200-nm, 400-nm and 800-nm height nanostructures. It can be observed

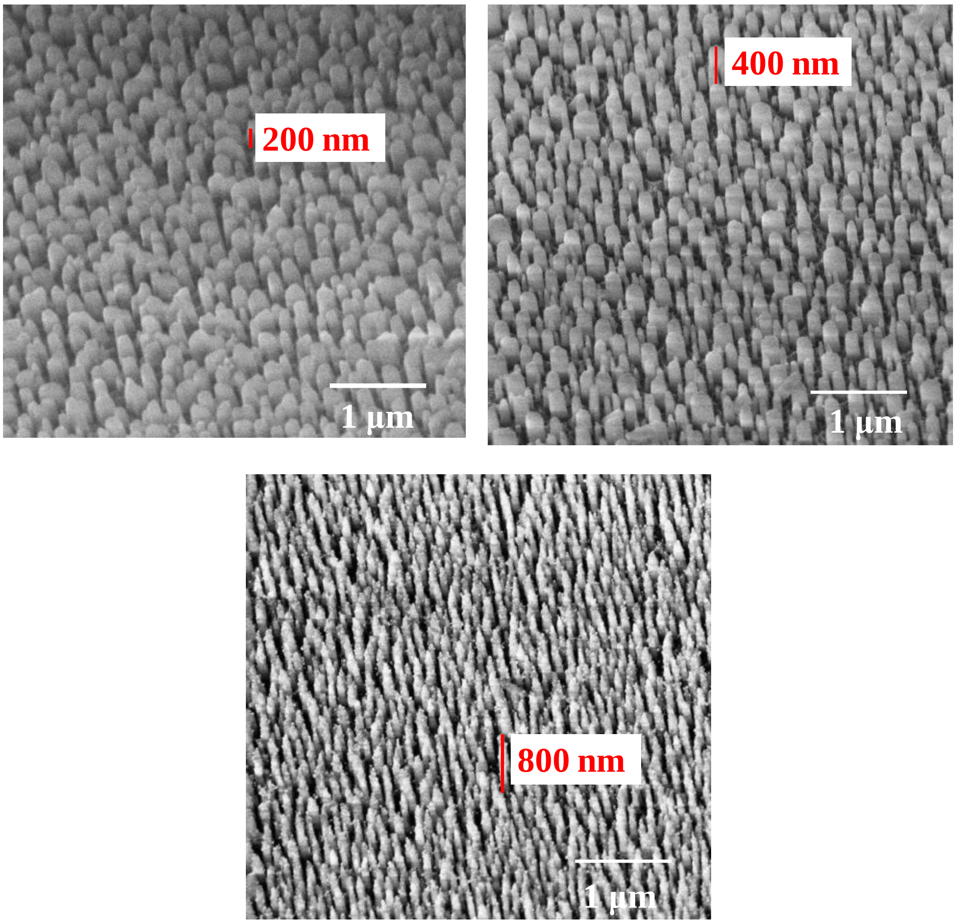

Figure 7.1 SEM images of nanostructured samples with heights of 200 nm, 400 nm and 800 nm.

that these nanostructured samples have a uniform height across the sample but varying diameter and pitch. It can also be seen that as the etching height increases, the structures attain a tapered shape and the pitch also increases.

In order to study the scattering properties of the fabricated nanostructures, haze and angular resolved scattering (ARS) are the most common methods of characterization. In this chapter, these measurements have been carried out for light at normal incidence. The optical properties, including transmission haze of planar and nanostructured glass substrates were measured using a UV-Visible spectrophotometer with an integrating sphere, using double beam method. The same method was also employed to characterize similar properties for textured glass in thin film solar cell modules. Angle resolved scattering was measured for transmission through planar and nanostructured glass samples using a scanning goniophotometer. The EQE of solar modules with planar and nanostructured glass packaging covers was measured using a standard system.

7.3 Optical Measurements

7.3.1 Specular and Hemispherical Transmission Measurements

Figure 7.2(a) and figure 7.2 (b) present the measured specular and hemispherical transmission profiles, respectively, for planar and nanostructured glass samples. It can be observed from figure 7.2(a) that nanostructured glass with 200-nm high nanostructures exhibits the maximum transmission compared to planar glass and nanostructured glass substrates of other heights, which is in agreement with the results reported for the previous samples in Chapters 5 and 6.

The nanostructured glass sample with 100-nm high nanostructures showed reduced transmission compared to the 200-nm nanostructured glass sample due a less optimized effective refractive index of the nanostructure features which is a function of the aspect ratio (ratio of height of nanostructure feature to the spacing/pitch between two adjacent nanostructures) of the etched nanostructures. However, when the etching height increases to 400-nm and 800-nm, there is a reduction in the optical specular transmittance over the measured wavelength spectrum. This phenomenon can be explained by effective medium theory, which describes the interaction between the effective refractive index of the fabricated nanostructures and the incident light.

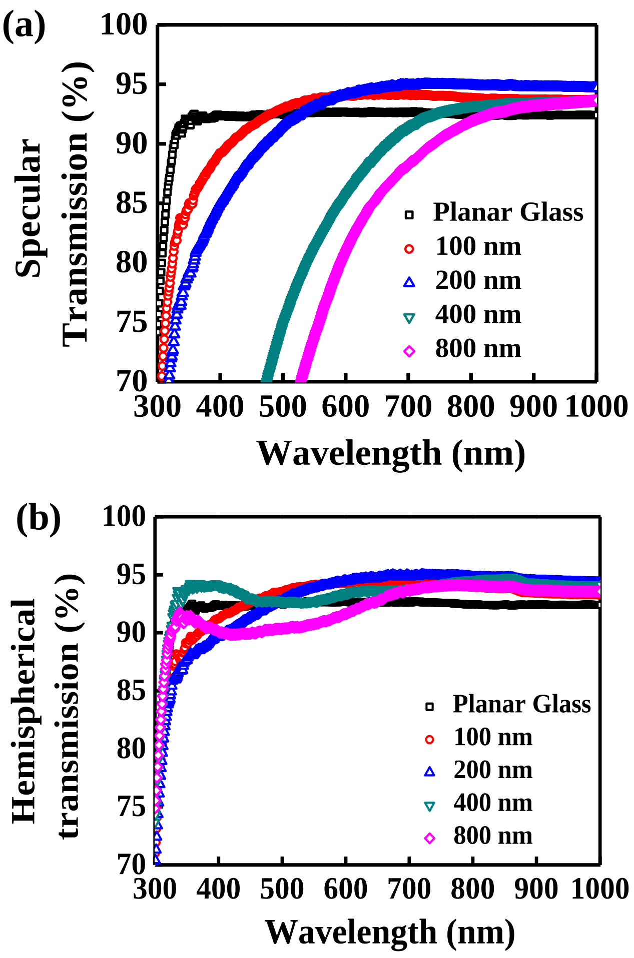

Figure 7.2 (a) Specular transmission and (b) Hemispherical transmission of planar and nanostructured glass samples.

As the etching height increases, there is a reduction in the sidewall morphology of the etched nanostructures. It can be seen from the SEM images in figure 7.1 that 800-nm height nanostructures have become thinner as compared to 200-nm and 400-nm high nanostructures. This change in morphology reduces the effective filling factor (the area ratio of nanostructures to the total substrate surface) of the structures over the substrate surface. According to EMT, the effective refractive index increases with the filling factor [235]. We hypothesize that the 200-nm high nanostructures have an optimum filling factor, hence providing maximum improvement in optical transmission. To verify this hypothesis, planar SEM

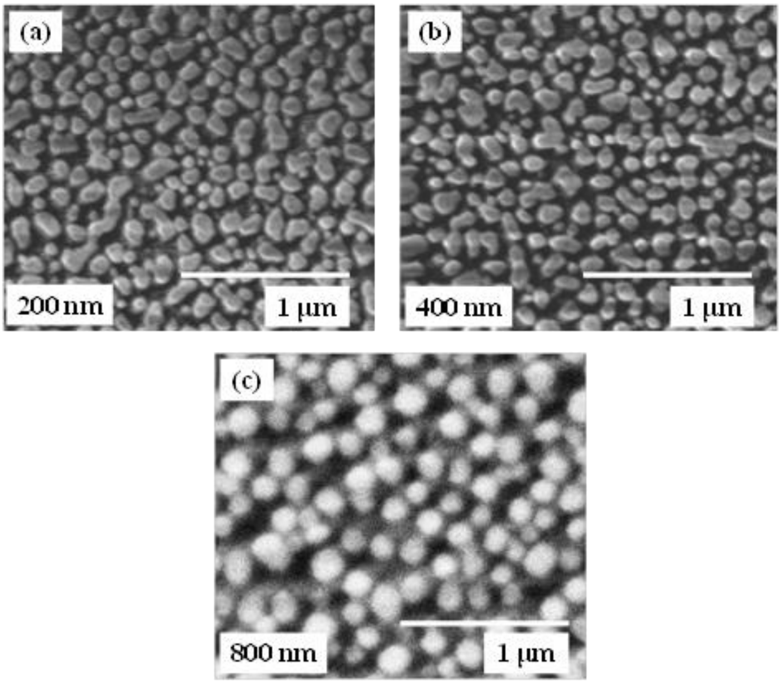

Figure 7.3 Planar SEM images of nanostructured glass samples with heights (a) 200 nm (etched for 2 mins), (b) 400 nm (etched for 4 mins), and (c) 800 nm (etched for 8mins).

Table 2 Summary of the parameters calculated from the planar SEM images of nanostructured glass substrates.

Parameters Height	Pitch/Spacing (nm)	Filling Factor(%)	Effective refractive index (n_{eff})
100 nm	157.56 ± 12.5	87.4 ± 0.9	1.433 ± 0.0049
200 nm	162.14 ± 18.1	87.5 ± 1.04	1.436 ± 0.0052
400 nm	186.9 ± 32.6	80.56 ± 1.45	1.397 ± 0.0078
800 nm	243.28 ± 41.5	72.8 ± 1.79	1.357 ± 0.0093

was carried out for the etched glass substrates in order to calculate the filling factor and pitch (average spacing) of the nanostructures after the etching process. Figure 7.3 (a, b, c) present the planar SEM images for the nanostructured samples of heights 200-nm, 400-nm and 800-nm respectively. Table 2 summarizes the filling factor measured from these SEM images. Based on the values of filling factor, the effective refractive index was also calculated using Equation 4.2. It can be seen from Table 2 that as the height of the nanostructures increases, the filling factor reduces. This supports the EMT theory where a reduction in optical transmission is observed with a reduction in the filling factor, as seen in the case of 800-nm nanostructured glass sample.

Now, comparing the measured specular (direct) and hemispherical transmission profiles, it can be observed that there is a drop in the specular transmission in the visible wavelength regime with an increase in the height of nanostructures. This reduction in direct transmission can be attributed to the scattering of light by the nanostructures. This scattered portion of the transmission spectrum which is not observed in the specular transmission profile is called diffuse transmission. This effect can be explained on the basis of the optical transmission measurement tool as follows: In the specular transmission mode (figure 7.4), the spectrophotometer detector measures only a direct beam of transmitted light through the nanostructured glass and does

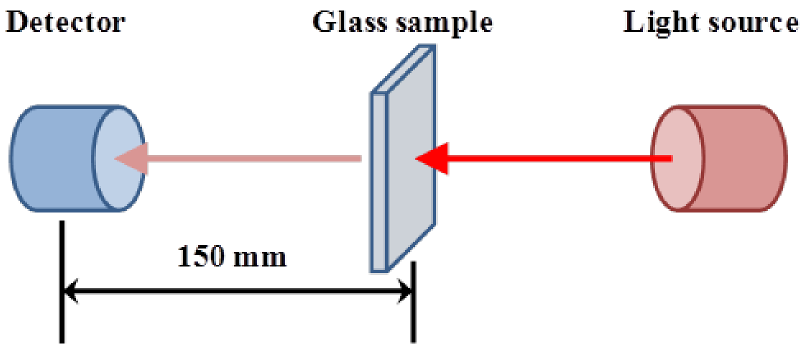

Figure 7.4 Schematic of the specular transmission measurement setup in a spectrophotometer.

not measure scattered light, due to the design of the spectrophotometer where the detector is ~150 mm away from the sample. However, hemispherical transmission was measured using an integrating sphere and it was noticed that taller nanostructures also provided an antireflection effect in the visible region in comparison to planar glass. However, there was a reduction in transmission observed in figure 7.2(b) for 400-nm and 800-nm nanostructured glass samples in the visible region which can be attributed to the scattered reflection from the surface of the sample due to a change in the aspect ratio of the structures because of increased etching time.

7.3.2 Haze Measurement

To understand the scattering behaviour of nanostructured glass samples, transmission haze was measured using an integrating sphere. Transmission haze quantifies the transmitted light that diffusely scatters when a beam of light impinges on a sample. Figure 7.5 presents the transmission haze measured for planar and nanostructured glass samples over a wavelength spectrum of 300-1000 nm.

The transmission haze for a particular sample depends on the feature dimensions of corrugations or texture on the sample surface [230]. It is well known that haze increases with the rms roughness of the texture [230] which is evident in figure 7.5 where rms roughness of the surface increases with the height of nanostructures. In figure 7.5, it is seen that the haze for planar glass is almost zero since the planar glass surface has a very low inherent surface roughness.

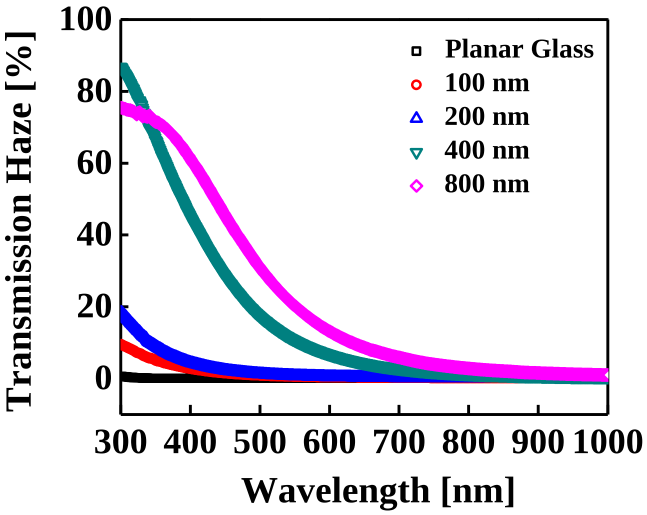

Figure 7.5 Transmission haze of planar and nanostructured glass samples.

For low aspect ratio nanostructured glass samples (100-nm and 200-nm), sample transmission is higher as seen in figures 7.2(a, b), due to low reflection losses. The other reason is the smooth variation in the refractive index of the sub-wavelength structures that are small compared to the wavelength. A similar situation is also seen in figure 7.5 for these samples where the transmission haze (scattering) is almost zero from 450-1000 nm. For shorter wavelengths (300-450 nm), there is a drastic increase in the scattering of light which is caused by near-field optical interactions with individual features, which make the air-nanostructure interface behave like a rough surface (Mie scattering). In this case, spacing between two adjacent nanostructures also plays a role, where minute surface reflections also occur.

The high aspect nanostructures (400-nm and 800-nm), also provide an antireflection effect in the long wavelength region as seen in figures 7.2(a,b) and low scattering as observed in figure 7.5. However, the specular transmission is drastically reduces and scattering (transmission haze) drastically increases for wavelengths equal to and less than 700 nm. This was again due to the aspect ratio and pitch of the nanostructures where the incident wavelength approached the feature size of the nanostructures.

Therefore, the transmission haze measurements demonstrate that diffuse scattering is an important phenomenon to be considered for wavelengths ≤ feature size, and that an increased specular transmission, by itself, is not a useful indicator of good antireflection performance.

7.3.3 Angle Resolved Scattering (ARS) Measurements

To further confirm the transmission haze behaviour of planar and nanostructured glass samples, ARS was measured for the samples at normal incidence of light using a goniophotometer. Figure 7.6(a) shows the transmission scattering intensity which is a planar section deduced from the angular resolved scattering result. It can be clearly seen in figure 7.6(a) that planar and nanostructured glass samples have a sharp transmission peak at normal incidence of light (at 0°). But the transmission peaks at normal incidence do not provide comparable results to the optical transmission measurements obtained in figure 7.2. Therefore, the ARS curves were integrated along the wavelength spectrum of the incident light source and absolute integrated values of transmission were obtained as plotted in figure 7.6(b). The integrated values of transmission present the same trend as the specular optical transmission curves obtained in figure 7.2.

The transmitted scattered light collected by the detector at oblique angles of incidence provide a clear understanding of the scattering behaviour of planar and nanostructured glass samples. It can be seen that planar glass has almost zero scattering behaviour whereas the scattering increases with the

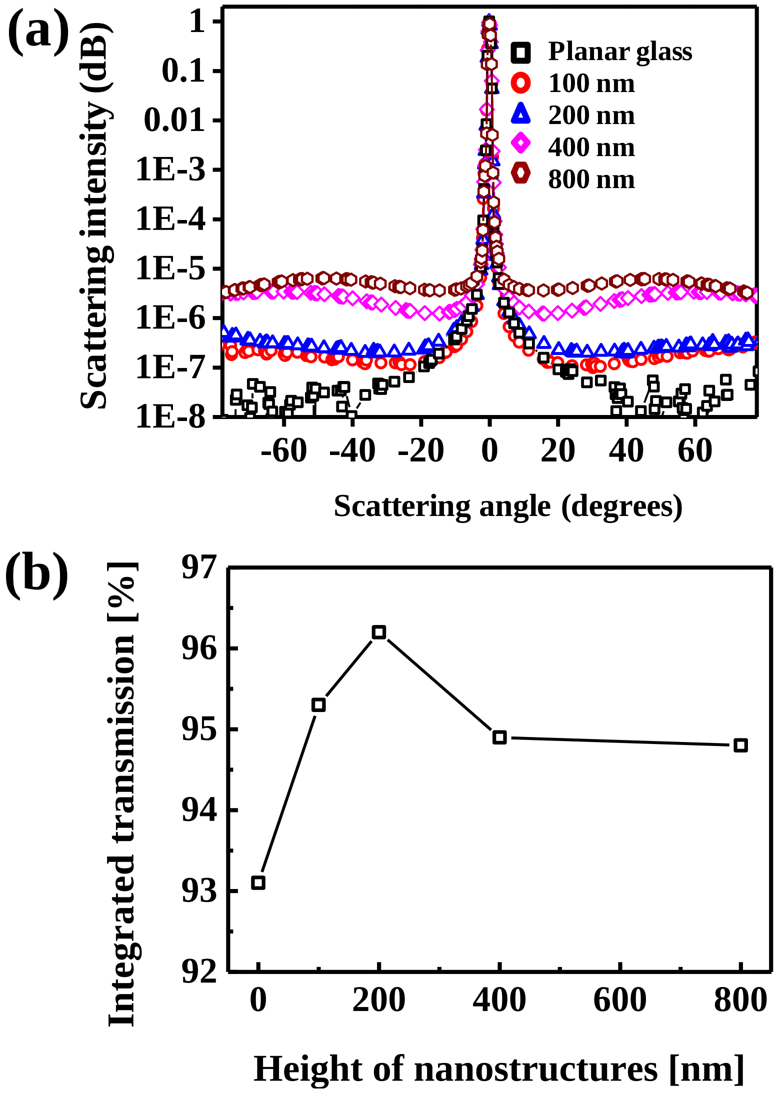

Figure 7.6 (a) Transmission scattering intensity and (b) Integrated transmission for planar and nanostructured glass samples.

height of nanostructures or aspect ratio. Therefore, these results are in agreement with the transmission haze results.

7.4 External Quantum Efficiency Measurements

According to reported work in the field of thin film solar cells, higher haze value should lead to higher short circuit current density for solar modules and hence higher external quantum efficiency. Therefore, to confirm this behaviour, a separate set of mini solar modules was prepared with planar and nanostructured glass samples as their packaging covers. The external quantum efficiency of these solar modules was measured so as to see the effect of their glass covers on their performance. Figure 7.7 presents the measured EQE of planar and nanostructured glass solar modules, and the total reflection of the solar modules was measured by an integrating sphere. Here, the EQE has been measured starting from 360 nm because the Pyrex lens on the light source absorbs the UV spectrum of the light source.

The results obtained from EQE measurements are in agreement with the optical transmission results discussed before. It can be seen that the planar glass module exhibits the lowest EQE over the measured wavelength spectrum

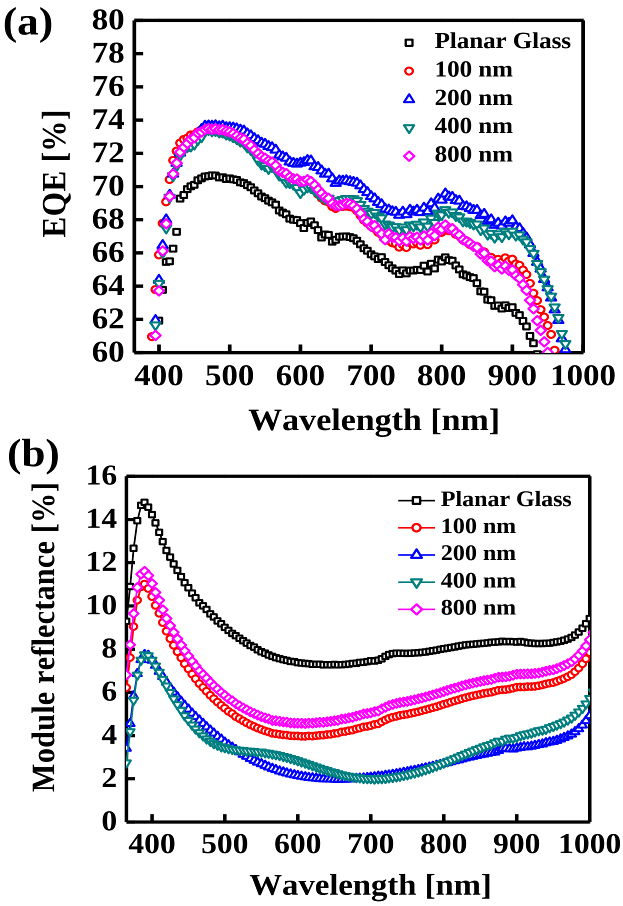

Figure 7.7 (a) External quantum efficiency and (b) Module reflectance of solar modules with planar and nanostructured glass substrates as their packaging covers.

due to surface reflections at the air/glass and glass/Si interfaces. However, an increase in the EQE was observed with nanostructured glass samples as the packaging covers of these solar modules.

A maximum increase was observed for the 200-nm nanostructured solar module which is consistent with the optical transmission results followed by 400-nm nanostructured solar module. Since 800-nm nanostructured glass had the lowest optical transmission performance, the same behaviour was also evident in the EQE data, whereas the 100-nm nanostructured glass solar module showed a lower performance despite the fact that 100-nm nanostructured glass had a better optical transmission performance. When light enters a solar module and is reflected back from the underlying silicon solar cell, some of it re-enters the air through the glass cover. In the case of planar glass, the reflected light from the cell largely escapes the front glass into air. However, the reflected light undergoes multiple reflections between the adjacent nanostructures in the case of nanostructured glass covers. This allows the light to enter the solar module again, hence, contributing to an enhancement in the EQE for 200-nm and 400-nm nanostructured glass modules.

It is very important to correlate the transmission haze data and EQE data. It was noticed from transmission haze measurements that nanostructures with high aspect ratios (400-nm and 800-nm) provide higher forward scattering as compared to low aspect ratio features. High aspect ratio features also scatter the light over a wider area as seen from data in figure 7.6(a). However, the EQE for high aspect ratio samples is lower. This phenomenon can be attributed to the absorption capability of the underlying solar cell at varied angles of incident light. Since 800-nm nanostructured glass sample scatters more light over a wider solid angle, light incident on a solar cell might not get absorbed, but can get reflected of the silicon surface which is due to the textural features on commercial silicon solar cell. Hence, a higher EQE is observed for low aspect ratio features.

Now, justifying the data in figure 7.7(a) and 7.7(b), it can seen that a planar glass solar module suffers a reflection loss of 9.5% in comparison to a 4% loss for a 200-nm nanostructured glass solar module at a wavelength of 500 nm. Assuming the transmission to be zero at this wavelength, light absorbed by the underlying solar cell is 90.5% and 96% for planar glass module and 200-nm module, respectively. Therefore, the absorption capability of a nanostructured solar module with 200-nm high features increases by an absolute 5.5% compared to a planar glass module. Taking into account the EQE of the bare silicon solar cell which is 76%, the increase in EQE of solar module employing nanostructured glass cover is ~4% which is similar to the increase seen in the data of figure 7.7(a).

Hence, nanostructured glass covers, due to their antireflection properties, provide an improvement in the device performance of solar modules.

7.5 Conclusions

The optical transmission and scattering behaviour of randomly arranged sub-wavelength features fabricated on borosilicate glass substrates have been studied. The sub-wavelength features exhibited improvement in optical transmission as compared to planar glass due to an effectively graded refractive index profile. However, the scattering properties of these nanostructures varied depending on their aspect ratios where low aspect ratio features provided lower scattering of light as compared to high aspect ratio features. The EQE of solar modules with planar and nanostructured glass packaging covers was also measured. In this case, low aspect ratio features of height 200-nm provided the maximum improvement in the EQE of solar module whereas high aspect ratio features of 800-nm provided the lowest EQE performance. Therefore, the study of scattering is an important phenomenon to be considered when designing antireflection structures both for the front glass cover and underlying solar cell.

8. Conclusions and Future Work

8.1 Summary and Conclusions

The wide literature available on antireflection, self-cleaning coatings and sub-wavelength structures suggests that there are still gaps to be filled in the present technology. There is a need to develop state of the art methods and knowledge to create surfaces and coatings in order to obtain the ultimate goal of antireflective and self-cleaning glass panels for solar modules.

An extensive amount of work has been done to develop antireflection technology for solar cells where the structures and coatings have been optimized and used in industrial production lines, whereas, little development work has been done to minimize transmission losses for the glass packaging cover. The transmission of the glass packaging cover is further reduced by the accumulation of dust particles when placed outdoors. This also contributes to the reduced performance of solar modules.

Therefore, this thesis discussed the field of antireflection and self-cleaning surfaces for glass packaging covers. This thesis showed a new fabrication method to nano-texture planar glass surfaces. This provided hybrid functionalities to the glass to achieve both antireflective and self-cleaning properties. The nano-textured glass cover was also used as a packaging cover for solar modules, thus increasing efficiency.

Firstly, this thesis provided an insight into the basic concepts of antireflection and self-cleaning followed by the research works reported in this field both for silicon and glass surfaces.

Subsequently, FDTD simulations were performed to design optimized features of antireflection structures for borosilicate glass substrates. The nanostructures were optimized in terms of their height, diameter and filling fraction, to provide broadband and omnidirectional antireflective behaviour. 3D simulations of random nanostructures on glass based on the fabrication process were also performed which were in agreement with the experimental results.

Then, a non-lithographic fabrication method based on dewetting of a metal nanoparticle mask was used to create random nanostructures on the glass surface. The fabrication method was used to create nanostructures of an average diameter of 100-nm with a varying pitch of 80-150 nm. The etching depth of the nanostructures remained uniform over the whole surface. The antireflective behaviour of the nanostructures was studied as a function of the height of nanostructures. It was observed that nanostructures of 200-400 nm height were optimum over a broad range of wavelengths. These optimized antireflection features also provided a significant improvement in the omnidirectional behaviour over a wide 120° angular range of solar incidence as compared to planar glass. These nanostructured glass samples also provided an improvement in the performance of solar modules when used as packaging covers. An absolute increase of 1.0 % in the power conversion efficiency was observed for 200-nm sized nanostructured glass solar module in comparison to a standard planar glass solar module.

For further analysis of these fabricated nanostructures, self-cleaning behaviour of planar and nanostructured glass substrates was evaluated. This study also provided an insight into the durability of these nanostructures. The planar and nanostructured glass substrates were exposed outdoors in the tropical climate of Singapore for 3 months during the rainy season. The glass substrates were mounted flat and at inclinations of 10° and 20°. The nanostructured glass samples provided a hydrophilic behaviour due to the Wenzel effect, and it was found that inclination was required for these hydrophilic nanostructured glass samples to exhibit lower dust accumulation and a self-cleaning effect. The sample with 200-nm high nanostructures again provided superior antireflective and self-cleaning behaviour after an exposure of 3 months outdoors. Solar modules with planar and nanostructured glass packaging covers were also mounted outdoors at an inclination of 20° and a reduction of only 0.3% efficiency was observed for a nanostructured glass module with 200-nm high nanostructures over a testing period of 5 weeks, in comparison to 2% drop for a planar glass solar module.

Thus, this demonstration of antireflective and self-cleaning performance of nanostructured glass samples can potentially find applications in other optoelectronic devices operating both indoors and outdoors, without any applications of chemical treatments or coatings to the system.

The scattering properties of planar and nanostructured glass samples was also studied, where the scattering performance gave an insight into the reduction of specular optical transmission for nanostructured glass samples. A correlation was seen between the aspect ratio of nanostructures and their scattering behaviour where low aspect ratio nanostructures provided lower scattering of light and vice versa. The EQE of the solar modules with planar and nanostructured glass packaging covers was also studied. It was observed that 200-nm nanostructured solar module exhibited improved EQE due to a superior effective graded refractive index profile and low aspect ratio, whereas improvement was also observed for high aspect ratio nanostructures of height 400-nm. This improvement with 400-nm high nanostructures is a function of the aspect ratio and filling fraction. However nanostructures of heights 100-nm and 800-nm provided reduced EQE performance compared to nanostructures of heights 200-nm and 400-nm.

Therefore, a smart, optimized surface was imparted to the glass samples which made them antireflective and self-cleaning. The fabrication and research in this thesis are limited to transparent materials such as glass, but such processes of fabrication and characterization can be applied to any surface which requires such properties.

8.2 Suggestions for Future Work

This thesis has provided a way to create a nanostructured glass sample with multifunctional properties which can be successfully applied as a packaging cover to improve the performance of solar modules. However, the fabrication process of this nanostructured glass poses high fabrication costs and problems of scalability to industrially sized glass packaging covers. Therefore, it needs industrial expertise and further examination. Chemical coatings can also potentially be applied to the surface of nanostructured glass substrates in order to tune the wetting properties. Some suggestions for future research and development are provided below:

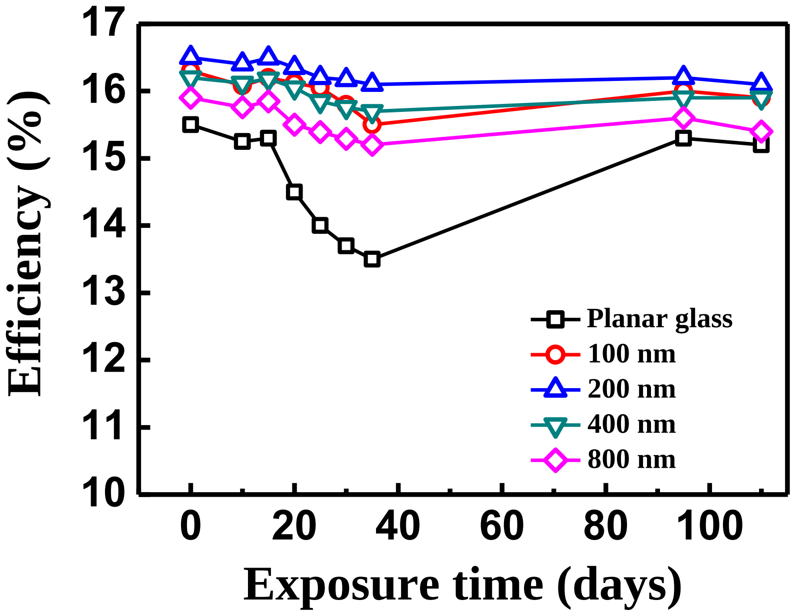

Figure 8.1 Present status of the outdoor measurements on mini solar modules.

1) Chapter 7 presented outdoor testing results for nanostructured glass substrates and mini solar modules with nanostructured glass packaging covers for 12 weeks and 5 weeks respectively. The degradation of the optical transmission or efficiency depends on the weather conditions such as high/low rainfall, dust and heat in a particular week or month. The change in weather may cause wide variations in the output which is evident from the obtained results. The measurements for the mini solar modules were not carried out after 35 days due to resource constraints. Figure 8.1 shows a glimpse of the measurement carried out again at day 95. It was observed that the performance of the modules improved, with planar glass module showing an improvement to the tune of 1.8%. It is intended to continue this work further as the resources become more consistently available. Under such a study, long term measurements could be reported.

2) The performance of the solar modules with nanostructured glass packaging covers can be improved by tuning the feature dimensions of the solar cells for

further reduction of reflection losses at the glass/silicon interface, thus improving the conversion efficiency and providing effective photon manipulation.

3) One of the best examples in nature exhibiting superior wetting behaviour is the lotus leaf, providing a superhydrophobic behaviour. The use of chemical coatings based on the lotus effect can help to reduce optical losses incurred on the surface of solar modules by accumulation of dust particles. Another idea which has been tried and is still under development is to provide electrical charges at the surface of a glass cover using metal electrodes embedded near the glass surface [231] to repel accumulated dust particles. This is an effective method in dry arid regions but is costly. Fluorine based coatings can also be a helpful agent to achieve self-cleaning behaviour in dry regions. One of the examples which is used in daily cookware is Teflon, which acts as an anti-stiction coating for water and dust. But optimization of the thickness of a Teflon coating is required.

4) The outdoor testing for planar and nanostructured glass substrates was carried out in the tropical weather of Singapore for 3 months. However, it is recommended to test similar samples for over a year so as to evaluate their performance over a longer period and in other climates as well. The glass samples should be exposed outdoors to dry arid regions, such as found in Kuwait, and cold region such as those found in the United States of America or Canada in winter.

Bibliography

[1] International Energy Agency (IEA), “Energy Poverty”, Available: http://www.iea.org/topics/energypoverty/

[2] UN News Centre, “World population projected to reach 9.6 billion by 2050 – UN report”, Available: http://www.un.org/apps/news/story.asp?NewsID=45165#.Utq2NtKwrDc

[3] N. S. Lewis and D. G. Nocera, “Powering the planet: Chemical challenges in solar energy utilization”, in Proceedings of the National Academy of Sciences of the United States of America, vol. 103, pp. 15729-15735, August 2006.

[4] John Miller (2013, April 17), “Which Government Policies and Other Factors Have Reduced U. S. Carbon Emissions”, The Energy Collective, Available: http://theenergycollective.com/jemillerep/211171/government-policies-and-other-factors-have-reduced-us-carbon-emissions

[5] Roger Boyd (2013, November 8), “Economic Growth: A Social Pathology”, Resilience, Available: http://www.resilience.org/stories/2013-11-07/economic-growth-a-social-pathology

[6] N. S. Lewis, “Powering the Planet”, Presentation, Available: http://www.jhuapl.edu/ClimateAndEnergy/Presentations/2010/Lewis_PoweringThePlanet.pdf

[7] “Solar Thermal Energy – an Industry Report”, Available: http://www.solar-thermal.com/solar-thermal.pdf

[8] G. W. Crabtree and N. S. Lewis, “Solar energy conversion”, Feature Article, Physics Today, March 2007.

[9] A. Harriman, “Prospects of conversion of solar energy into chemical fuels: the concept of a solar fuels industry”, Philosophical Transactions of The Royal Society A, vol. 371, pp. 20110415-20110430, August 2013.

[10] P. Mints, “The history and future of incentives and the photovoltaic industry and how demand is driven”, Progress in Photovoltaics: Research and Applications, vol. 20, pp. 711-716, September 2012.

[11] Stephen Lacey (2013, August 23), “Here’s How Chinese Firms Will Produce Solar for 36 Cents per Watt”, GreenTechSolar, Available: http://www.greentechmedia.com/articles/read/solar-cost-reduction-drivers-in-2017

[12] W. L. O. O. Izuchukwu, “A Comparitive Study on Solar Photovoltaic Industrial Development in Germany, China and USA”, Journal of Economics and Sustainable Development, vol. 4, 2013.

[13] C. Breyer and A. Gerlach, “Global Overview on Grid-Parity Event Dynamics”, Proceedings of the 25th European Photovoltaic Solar Energy Conference and Exhibiton, pp. 5283-5304, September 2010.

[14] E. Becquerel, “Memoire sur les effets electriques produits sous l’influence des rayons solaires”, Comptes Rendus, vol. 9, pp. 561-567, 1839.

[15] D. M. Chaplin, C. S. Fuller, and G. L. Pearson, “A new silicon p-n junction photocell for converting solar radiation into electrical power”, Journal of Applied Physics, vol. 25, pp. 676-677, May 1954.

[16] Dow Corning, “Solar Energy 101: Introduction to Solar Energy”, Available: http://www.dowcorning.com/content/solar/solarworld/solar101.aspx

[17] Canada Mortgage and Housing Corporation, “Photovoltaic Systems”, Available: http://www.cmhc-schl.gc.ca/en/co/grho/grho_009.cfm

[18] PVEDUCATION.ORG, “Open Circuit Voltage”, Available: http://pveducation.org/pvcdrom/solar-cell-operation/open-circuit-voltage

[19] Green Rhino Energy, “Energy Yield and Performance Ratio of Photovoltaic Systems”, Available: http://www.greenrhinoenergy.com/solar/technologies/pv_energy_yield.php

[20] D. L. King et al. “Field experience with a new performance characterization procedure for photovoltaic modules”, 2nd World Conference and Exhibition on PV Solar Energy Conversion, Vienna, Austria, July 1998.

[21] W. B. Stine and M. Geyer, “The Sun’s Energy”, Title in their book “Power from the Sun”, Available: http://www.powerfromthesun.net/book.html

[22] A. Y. Al-Hasan, “A new correlation for direct beam solar radiation received by photovoltaic panel with sand dust accumulated on its surface”, Solar Energy, vol. 63, pp. 323-333, November 1998.

[23] M.I. Safar and Kuwait Meteorological Department Climatological Section, Frequency of dust in day-time summer in Kuwait, Kuwait: Directorate General of Civil Aviation, Meteorological Department, Climatological Section, 1980.

[24] M.I. Safar and Kuwait, Meteorological Department, Dust and duststorms in Kuwait, Kuwait: State of Kuwait, Directorate General of Civil Aviation, Meteorological Department, 1980.

[25] S. Biryukov, “An experimental study of the dry deposition mechanism for airborne dust”, Journal of Aerosol Science, vol. 29, pp. 129-139, January-February 1998.

[26] M. Mani and R. Pillai, “Impact of dust on solar photovoltaic performance: Research status, challenges and recommendations”, Renewable and Sustainable Energy Reviews, vol. 14, pp. 3124-3131, December 2010.

[27] D. Goossens and E. Van Kerschaever, "Aeolian dust deposition on photovoltaic solar cells: the effects of wind velocity and airborne dust concentration on cell performance", Solar Energy, vol.66. pp. 277-289, July 1999.

[28] J. Z. Casanova et al., "Analysis of dust losses in photovoltaic modules", World Renewable Energy Congress, Linkoping, Sweden, May 2011.

[29] D. C. Jordan, and S. R. Kurtz, "Photovoltaic degradation rates – an analytical review", Progress in Photovoltaics: Research and Applications, vol. 21, pp. 12-29, January 2013.

[30] T. Townsend and L. Powers (2012, June 15), "Solar Winter Output Assessment: Measuring Snow-related Losses", Available: http://www.renewableenergyworld.com/rea/news/article/2012/06/wrap-up-solar-winter-output-assessment

[31] R. E. Hanitsch, D. Schulz, and U. Siegfried, "Shading effects on output power of grid connected photovoltaic generator systems", Rev. Energ. Ren. : Power Engineering, pp. 93-99, 2001.

[32] A. R. Parker and H. E. Townley, "Biomimetics of photonic nanostructures", Nature Nanotechnology, vol. 2, pp. 347-353, June 2007.

[33] T. McKeag (2009, September 02), "How Termites Inspired Mick Pearce's Green Buildings", GreenBiz.com, Available: http://www.greenbiz.com/blog/2009/09/02/how-termites-inspired-mick-pearces-green-buildings

[34] C. Suddath (2010, June 15), "A Brief History of: Velcro", Time U.S., Available: http://content.time.com/time/nation/article/0,8599,1996883,00.html

[35] T. Hamilton (2008, March 6), "Whale Inspired Wind Turbines", MIT Technology Review, Available: http://www.technologyreview.com/news/409710/whale-inspired-wind-turbines/

[36] Airbus, "Biomimicry", Available: http://www.airbus.com/innovation/eco-efficiency/design/biomimicry/

[37] National History Museum (2008, August 15), "Olympic swimsuit mimics shark skin", Available: http://www.nhm.ac.uk/about-us/news/2008/august/olympic-swimsuit-mimics-shark-skin18219.html

[38] L. Wright (2003, March 3), "Lotus Leaf Inspires Waterproofing Scheme", Scientific American, Available: http://www.scientificamerican.com/article.cfm?id=lotus-leaf-inspires-water

[39] B. Bhushan, “Biomimetics: lessons from nature – an overview”, Philosophical Transactions of The Royal Society A, vol. 367, pp. 1445-1486. 2009.

[40] A. R. Parker, “A vision for natural photonics”, Philosophical Transactions of the Royal Society A: Mathematical, Physical and Engineering Sciences, vol. 362, pp. 2709-2720, December 2004.

[41] K. Yu et al., “Biomimetic optical materials: Integration of nature’s design for manipulation of light”, Progress in Materials Science, vol. 58, pp. 825-873, March 2013.

[42] A. E. Rawlings, J. P. Bramble, and S. S. Staniland, “Innovation through imitation: biomimetic, bioinspired and biokleptic research”, Soft Matter, vol. 8, pp. 6675-6679, April 2012.

[43] T. Lenau (2013, September 17), “Bio-inspired design – Biomimetics”, The Biomimetic Project, Available: http://polynet.dk/bionik/

[44] M. Burrows and G. Sutton, “Interacting gears synchronize propulsive leg movements in a jumping insect”, Science, 341, pp. 1254-1256, September 2013.

[45] F. Priolo et al., “Silicon nanostructures for photonics and photovoltaics”, Nature Nanotechnology, 9, pp. 19-32, January 2014.

[46] W. H. Miller, A. R. Moller and C. G. Bernhard, “The functional organization of the compound eye”, Pergamon Press, Oxford, 1966.

[47] C.G. Bernhard, Editor, International symposium on the functional organization of the compound eye, International symposium series Wenner-Gren Center; 7, Oxford: Pergamon, October 1965.

[48] C. G. Bernhard, “Structural and functional adaptation in a visual system”, Endeavour, 26, pp. 79-84, March 1968.

[49] AskNature (2012, August 3), “Corneal gratings reduce adhesion: moth and fly”, Available: http://www.asknature.org/strategy/ab26d22f288884e77c012efc91a0db77

[50] Janet Fang (2012, July 16), “Moth eye radiation-reducing materials”, SMARTPLANET, Available: http://www.smartplanet.com/blog/rethinking-healthcare/moth-eye-inspires-radiation-reducing-materials/

[51] Bored Panda, “Looking at the world through a microscope (part I)”, Available:http://www.boredpanda.com/looking-at-the-world-through-a-microscope-part-i/

[52] M. Berger (2008, October 28), “Moth eyes inspire self-cleaning antireflection nanotechnology coatings”, nanowerk, Available: http://www.nanowerk.com/spotlight/spotid=7938.php

[53] A. Yoshida et al. “Antireflective nanoprotuberance array in the transparent wing of a hawkmoth, Cephonodes hylas”, Zoological Science, vol. 14, pp. 737-741, May 1997.

[54] A. Yoshida et al., “Nanoprotuberance array in the transparent wing of a hawkmoth, Cephonodes hylas”, Zoological Science, vol. 13, pp. 525-526, May 1996.

[55] A. Yoshida et al., “Antireflective nanoprotuberance array in the transparent wing of a hawkmoth, Cephonodes hylas”, Zoological Science, 14, pp. 737-741, May 1997.

[56] “Biology 210 – Scanning Electron Microscopy”, Available: http://www.trincoll.edu/~alehman/photobiol210_03.htm

[57] A. R. Parker, Z. Hegedus, and R. A. Watts, “Solar-absorber antireflector on the eye of an Eocene fly (45 ma)”, Proceedings of the Royal Society B, vol. 265, pp. 811-815, May 1998.

[58] C. G. Bernhard, W. H. Miller and J. Sallstrom, “Comparative ultrastructure of corneal surface topography in insects with aspects of phylogenesis and function”, Journal of Comparative Physiology A: Neurothology, Sensory, Neural and Behavioural Physiology, vol. 67, pp. 1-25, March 1970.

[59] D. G. Stavenga et al., “Light on the moth-eye corneal nipple arrays of butterflies”, Proceeding of the Royal Society, vol. 273, pp. 661-667, December 2006.

[60] A. K. Sood et al., “Design considerations using APD detectors for high resolution UV imaging applications”, Proceedings of SPIE, vol. 7419, pp. 74190V1-8, August 2009.

[61] M. J. Cohen et al., “InGaAs sensor/focal plane arrays for SWIR applications”, Proceedings of SPIE, vol. 5406, pp. 38-45, 2004.

[62] A. K. Sood et al., “Development of low dark current SiGe-detector arrays for visible-NIR imaging sensor” Proceedings of SPIE, vol. 7298, pp. 72983D1-11, 2009.

[63] M. Davis et al., “Advanced InSb FPA sensor development at CMC Electronics”, Proceedings of SPIE, vol. 5563, pp. 62-73, 2004.

[64] A. K. Sood et al., “Multispectral EO/IR sensor model for evaluating UV, visible, SWIR, MWIR, and LWIR system performance”, Proceedings of SPIE, vol. 7300, pp. 73000H, 2009.

[65] P. W. Norton et al., “Commercialization of uncooled infrared technology”, Proceedings of SPIE, vol. 5563, pp 55-61, 2004.

[66] A. K. Sood et al., “EO/IR sensors development using zinc oxide and carbon nanostructures”, Proceedings of SPIE, vol. 7318, pp. 731804, 2009.

[67] A. K. Sood et al., “Development of high performance radiation hardened antireflection coatings for LWIR and multicolour IR focal plane arrays”, Proceedings of SPIE, vol. 6206, pp. 620615, 2006.

[68] K. Koch, B. Bhushan and W. Barthlott, “Diversity of structure, morphology, and wetting of plant surfaces”, Soft Matter, vol. 4, pp. 1943-1963, May 2008.

[69] K. Koch, B. Bhushan, and W. Barthlott, “Multifunctional surface structures of plants: an inspiration for biomimetics”, Prog. Mater. Sci., 54, pp. 137-178, February 2009.

[70] K. Koch, B. Bhushan, and W. Barthlott, “Functional plant surfaces, smart materials. In Springer handbook of nanotechnology (ed. B. Bhushan), 3rd edn. Heidelberg, Germany: Springer.

[71] G. Romer (2009, October 26), “Ultra short pulse laser generated surface textures for anti-ice applications in aviation”, Laser Institute of America, Available: http://www.lia.org/blog/2009/10/ultra-short-pulse-laser-generated-surface-textures-for-anti-ice-applications-in-aviation/

[72] M. Barberoglou et al. (2009, January 19), “Laser structuring of water-repellent biomimetic surfaces”, SPIE Newsroom, Available: http://spie.org/x33323.xml?pf=true&ArticleID=x33323/

[73] Dr. Bharat Bhushan, Nanoprobe Laboratory for Bio- and Nanotechnology and Biomimetics, Institute of Materials Research, Ohio State University, Available: http://imr.osu.edu/research/facilities/nanoprobe-laboratory-for-bio-and-nanotechnology-and-biomimetics-nlbb/

[74] B. Bhushan and Y. C. Jung, “Wetting, adhesion and friction of superhydrophobic and hydrophilic leaves and fabricated micro/nanopatterned surfaces”, Journal of Physics: Condensed Matter, vol. 20, pp. 225010-225033, April 2008.

[75] M. Nosonovsky and B. Bhushan, “Multiscale dissipative mechanisms and hierarchical surfaces: friction, superhydrophobicity, and biomimetics”, Heidelberg, Germany: Springer, 2008.

[76] M. Nosonovsky and B. Bhushan, “Roughness induced superhydrophobicity: a way to design non-adhesive surfaces”, Journal of Physics: Condensed Matter, vol. 20, pp. 225009-2250038, 2008.

[77] M. Nosonovsky and B. Bhushan, “Biologically inspired surfaces: broadening the scope of roughness”, Advanced Functional Materials, 18, pp. 843-855, March 2008.

[78] B. Bhushan, “Principles and applications of tribology”, New York, NY: Wiley, 1999.

[79] B. Bhushan, “Introduction to tribology”, New York, NY: Wiley, 2002.

[80] Green tribology: principles, research areas and challenges, rsta.royalsocietypublishing.org.

[81] M. Qu, J. He and J. Zhang, Superhydrophobicity, Learn from the Lotus Leaf", Intech, Available: http://www.intechopen.com/books/biomimetics-learning-from-nature/superhydrophobicity-learn-from-the-lotus-leaf

[82] Green tribology: principles, research areas and challenges, rsta.royalsocietypublishing.org

[83] X.F. Gao and L. Jiang, "Biophysics: water repellent legs of water striders", Nature, vol. 432, pp. 36, November 2004.

[84] A.K. Kota, and A. Tuteja, "Superoleophobic surfaces", Advances in Fluorine containing polymers, Chapter 11, pp. 171-185.

[85] E. Hecht, "Optics", Addison Wesley, 2002.

[86] N. White and S. Beeby, Editors, "Energy harvesting for autonomous systems", Artech House, 2010.

[87] A. Antonini, "Chapter 2: Photovoltaic Concentrators – Fundamentals, Applications, ‚Market and Prospective", Solar Collectors and Panels, Theory and Applications, Available: http://www.intechopen.com/download/get/type/pdfs/id/12218

[88] H. A. Macleod, "Thin film optical filters", 3rd Edition, Book, Institute of Physics Publishing, London, United Kingdom.

[89] S. Duttagupta et al., "Optimized antireflection coatings using silicon nitride on textured silicon surfaces based on measurements and multidimensional modelling", Energy Procedia, vol. 15, pp. 78-83, March 2012.

[90] J. Kim et al., "Double antireflection coating layer with silicon nitride and silicon oxide for crystalline silicon solar cell", Journal of Electroceramics, vol. 30, pp. 41-45, April 2013.

[91] S. Fujihara, M. Tada and T. Kimura, "Preparation and characterization of MgF_2 thin film by a trifluoroacetic acid method", Thin Solid Films, vol. 304, pp. 252-255, July 1997.

[92] T. Yoshida, K. Nishimoto, K. Sekine, and K. Etoh, "Fluoride antireflection coatings for deep ultraviolet optics deposited by ion-beam sputtering", Applied Optics, vol. 45, pp. 1375-1370, March 2006.

[93] H. J. Hovel, "TiO_2 antireflection coatings by a low temperature spray process", Journal of the Electrochemical Society, vol. 125, pp. 983-985 1978.

[94] B. S. Richards et al., “TiO_2 DLAR coatings for planar silicon solar cells”, Progress in Photovoltaics: Research and Applications, vol.11, pp. 27-32, January 2003.

[95] G. S. Liou et al., “Highly flexible and optical transparent 6F-PI/TiO_2 optical hybrid films with tunable refractive index and excellent thermal stability", Journal of Materials Chemistry, vol. 20, pp. 531-536, November 2009.

[96] C. Martinet et al., “Deposition of SiO_2 and TiO_2 thin films by plasma enhanced chemical vapor deposition for antireflection coating”, Journal of Non-Crystalline Solids, vol. 216, pp. 77-82, August 1997.

[97] J. Stone and L.W. Stulz, “Reflectance, transmittance, and loss spectra of multilayer Si/SiO_2 thin film mirrors and antireflection coatings for 1.5 μm”, Applied Optics, vol. 29, pp. 583-588, February 1990.

[98] S.L. Diedenhofen et al., “Broadband and omnidirectional antireflection coatings based on semiconductor nanorods”, Advanced Materials, vol. 21, pp. 973-978, January 2009.

[99] K. Tadanaga, N. Katata, and T. Minami, “Super-water repellent Al_2O_3 coating films with high transparency”, Journal of the American Ceramic Society, vol. 80, pp. 1040-1042, April 1997.

[100] M.H. Asghar et al., “Study of thin film structure based on MgF_2, CeO_2 and Al_2O_3 layers for optical applications”, International Journal of Materials Research, vol. 99, pp. 322-328, March 2008.

[101] S. Chattopadhyay et al., “Antireflecting and photonic nanostructures”, Materials Science and Engineering: R: Reports, vol. 69, pp. 1-35, June 2010.

[102] M. Buchanan, J.B. Webb and D.F. Williams, “Preparation of conducting and transparent thin films of tin-doped indium oxide by magnetron sputtering”, Applied Physics Letters, vol. 37, pp. 213-215, July 1980.

[103] F. Rubio et al., “Sputtered Ta_2O_5 antireflection coatings for silicon solar cells”, Thin Solid Films, vol. 90, pp. 405-408, April 1982.

[104] M. Mazur et al., “TiO_2/SiO_2 multilayer as an antireflective and protective coating deposited by microwave assisted magnetron sputtering”, Opto-Electronics Review, vol. 21, pp. 233-238, June 2013.

[105] B. Tripathi et al., “Influence of optical properties of ZnO thin-films deposited by spray pyrolysis and RF magnetron sputtering on the output performance of silicon solar cell”, IOP Conference Series: Materials Science and Engineering, vol. 43, pp. 012002-012006, 2013.

[106] L. J. He, C. Li, and X. Z. Liu, “The optical properties of alumina films prepared by electron beam evaporation at oblique angles”, Materials Letters, vol. 101, pp. 1-4, 2013.

[107] S. P. Huber et al.,“Engineering optical constants for broadband single layer antireflection coatings”, Proceedings of SPIE, vol. 8848, pp. 884814-884817, September 2013.

[108] E.R. Klobukowski et al., “Atmospheric pressure chemical vapor deposition of high silica SiO_2-TiO_2 antireflective thin films for glass based solar panels”, Journal of Materials Chemistry C, vol. 1, pp. 6188-6190, August 2013.

[109] R. Yang, T. Buonassisi, and K.K. Gleason, “Thin films: Organic vapor passivation of silicon at room temperature”, Advanced Materials, vol. 25, pp. 2077, April 2013.

[110] D. Hocine et al., “Improved efficiency of multicrystalline silicon solar cells by TiO_2 antireflection coatings derived by APCVD process”, Materials Science in Semiconductor Processing, vol. 16, pp. 113-117, June 2013.

[111] H.K. Raut et al., “Fabrication of highly uniform and porous MgF2 antireflective coatings by polymer based sol-gel processing on large area glass substrates” Nanotechnology, vol. 24, pp. 505201-505208, November 2013.

[112] X.X. Zhang et al., “Template free sol-gel preparation of superhydrophobic ORMOSIL films for double wavelength broadband antireflective coatings” Advanced Functional Materials, vol. 23, pp. 4361-4365, September 2013.

[113] L. Ye et al., “Sol-gel preparation of SiO_2/TiO_2/SiO_2-TiO_2 broadband antireflective coating for solar cell cover glass”, Solar Energy Materials and Solar Cells, vol. 111, pp. 160-164, April 2013.

[114] W. M. Chiu et al., “Characterization of antireflective coatings on poly(methyl methacrylate) substrate by different process parameters”, Journal of Applied Polymer Science, vol. 129, pp. 2411-2417, January 2013.

[115] C.S. Thompson, R.A. Fleming, and M. Zou, “Transparent self-cleaning and antifogging silica nanoparticle films”, Solar Energy Materials and Solar Cells, vol. 115, pp. 108-113, August 2013.

[116] S. Choudhary, M. Singh, and R.K. Kale, “Surfactant-catalyzed SiO_2 thin films preparation and characterization”, Journal of Adhesion Science and Technology, vol. 27, pp. 2629-2641, May 2013.

[117] R. Prado et al., “Development of multifunctional sol-gel coatings: Antireflection coatings with enhanced self-cleaning capacity”, Solar Energy Materials and Solar Cells, vol. 94, pp. 1081-1088, June 2010.

[118] Y.M. Song, and Y.T. Lee, “Investigation of geometrical effects of antireflective subwavelength grating structures for optical device applications”, Optical and Quantum Electronics, vol. 41, pp. 771-777, August 2009.

[119] J. Fraunhofer, *Joseph von Fraunhofer Gesannekte Schrifen*, Munich, Germany, 1888.

[120] A. A. Daniyan, L. E. Umoru, and B. Olunlade, “Preparation of Nano-TiO_2 thin film using spin coating method”, Journal of Minerals and Materials Characterization and Engineering, vol. 1, pp. 138-144, July 2013.

[121] D. Rathee, S.K. Arya, and M. Kumar, “Preparation and characterization of TiO_2 and SiO_2 thin films”, World Journal of Nano Science and Engineering, vol. 1, pp. 84-88, 2011.

[122] C.M. Firdaus et al., “Characterization of ZnO and ZnO:TiO_2 thin films prepared by sol-gel spray-spin coating technique”, Procedia Engineering, vol. 41, pp. 1367-1373, August 2012.

[123] K. Peng et al., “Effects of catalyst on the transmittance and stability of SiO_2 antireflective film prepared by sol-gel method”, Advanced Materials Research, vol. 834-836, pp. 462-465, October 2013.

[124] J. Tian, S.K. Deng, and P.Z. Yang, “Optimization of porous SiO_2 antireflective coatings used in encapsulating solar modules”, Advanced Materials Research, vol. 739, pp. 94-100, August 2013.

[125] L. Gao, and J. He, “A facile dip-coating approach based on three silica sols to fabrication of broadband antireflective superhydrophobic coatings”, Journal of Colloid and Interface Science, vol. 400, pp. 24-30, June 2013.

[126] X. Meng et al., “Preparation of the multifunctional antireflective films from a templating composite silica sol with etwining structures”, Surface and Coatings Technology, vol. 236, pp. 518-524, December 2013.

[127] C. Xin et al., “A novel route to prepare weather resistant, durable antireflective films for solar glass”, Solar Energy, vol. 93, pp. 121-126, July 2013.

[128] E.Z. Alejandre et al., “Optical characteristics of silica coatings deposited bt ozone assisted spray pyrolysis technique”, ECS Journal of Solid State Science and Technology, vol. 2, pp. N145-N148, May 2013.

[129] Z.Q. Zhang, “Research progress of self-cleaning architectural coatings”, Advanced Materials Research, vol. 790, pp. 320-323, September 2013.

[130] D.M. Sim et al., “Ultra-high optical transparency of robust, graded index and anti-fogging silica coating derived from Si-containing block copolymers”, vol. 1, pp. 428-433, June 2013.

[131] Prospect Glass ohne Reflexe. Deutsche Spezialglas AG, Grunenplan, FRG.

[132] M.J. Minot, “Single layer, gradient refractive index antireflection films effective from 0.35 to 2.5 μm”, Journal of Optical Society of America, vol. 66, pp. 515-519, June 1976.

[133] T. Minami, “Advanced sol-gel coatings for practical applications”, Journal of Sol-Gel Science and Technology, vol. 65, pp. 4-11, January 2013.

[134] W. Dou et al., “Preparation of single layer antireflective SiO_2 coating with broadband transmittance using PEG-modified sol-gel method”, Journal of Sol-Gel Science and Technology, vol. 68, pp. 302-306, November 2013.

[135] G. S. Vicente, A. Morales, M. T. Gutierrez, “Preparation and characterization of sol-gel TiO_2 antireflective coatings for silicon”, Thin Solid Films, vol. 391, pp. 133-137, July 2001.

[136] Q. N. Zhao et al., “Preparation and characterization of nano-porous SiO_2/TiO_2-SiO_2 thin films on glass substrates by sol-gel method”, Key Engineering Materials, vol. 531-532, pp. 651-654, December 2012.

[137] V. H. L. Caer et al., “Optical and morphological characterization of low refractive index materials for coatings on solar collector glazing”, Renewable Energy, vol. 53, pp. 27-34, May 2013.

[138] P. Spinelli et al., “Al_2O_3/TiO_2 nano-pattern antireflection coating with ultralow surface recombination”, Applied Physics Letters, vol. 102, pp. 233902-233905, June 2013.

[139] T.K. Lim, “Canon 24mm f/1.4 L II USM Lens”
Available: http://tk2899.blogspot.sg/2008/09/canon-24mm-f14-l-ii-usm-lens.html

[140] Y. Kanamori, M. Okochi, and K. Hane, “Fabrication of antireflection subwavelength gratings at the tips of optical fibers using UV nanoimprint lithography”, Optics Express, vol. 21, pp. 322-328, January 2013.

[141] J.H. Choi et al., “Fabrication of TiO_2 nano-to-microscale structures using UV nanoimprint lithography”, Nanotechnology, vol. 24, pp. 195301-195308, April 2013.

[142] T. Khaleque, H.G. Svavarsson, and R. Magnusson, “Fabrication of resonant patterns using thermal nano-imprint lithography for thin-film photovoltaic applications”, Optics Express, vol.21, pp. A631-A641, May 2013.

[143] J.W. Leem et al., “Nanostructured encapsulation cover glasses with wide angle broadband antireflection and self-cleaning properties for III-V multi-junction solar cell applications” Solar Energy Materials and Solar Cells, vol. 120, pp. 555-560, January 2014.

[144] S. Sarkar and S.K. Pradhan, “Tailoring of optical and wetting properties of sputter deposited silica thin films by glancing angle deposition”, Applied Surface Science, vol. 290, pp. 509-513, January 2014.

[145] S. Sun et al., “Fabrication of antireflecting Si nanostructures with low aspect ratio by nanosphere lithography technique”, Nano-Micro Letters, vol. 5, pp. 18-25, March 2013.

[146] H.K. Raut et al., “Robust and durable polyhedral oligomeric silsesquioxane based antireflective nanostructures with broadband quasi omnidirectional properties”, Energy and Environmental Science, vol. 6, pp. 1929-1937, April 2013.

[147] Z. Yu et al., “Fabrication of large area subwavelength antireflection structures on Si using trilayer resist nanoimprint lithography and liftoff”, Journal of Vacuum Science and Technology B, vol. 21, pp. 2874-2878, November/December 2003.

[148] J.H. Kim et al., “Enhancement of outcoupling efficiency of organic light emitting diodes using a planarized moth-eye structure on glass substrates”, Optics Letters, vol. 38, pp. 3773-3775, September 2013.

[149] D.S. Kim, D.H. Kim, and J.H. Jang, “A nanoscale conical polymethyl methacrylate (PMMA) sub-wavelength structure with a high aspect ratio realized by a stamping method”, Optics Express, vol. 21, pp. 8450-8459, March 2013.

[150] M.E. Park et al., “Fabrication of a Ni nanoimprint stamp for an antireflective layer using an anodic aluminium oxide template”, Journal of Nanoscience and Nanotechnology, vol. 13, pp. 7586-7589, November 2013.

[151] S. Landis et al., “Silicon solar cells efficiency improvement with nanoimprint lithography technology”, Microelectronic Engineering, vol. 111, pp. 224-228, November 2013.

[152] S. Ji et al., “Optimal moth eye nanostructure array on transparent glass towards broadband antireflection”, Applied Materials and Interfaces, vol. 5, pp. 10731-10737, October 2013.

[153] T. Maier et al., “Antireflective surface structures in glass by self assembly of SiO_2 nanoparticles and wet etching”, Optics Express, vol. 21, pp. 20254-20259, August 2013.

[154] C.H. Sun et al., “Templated fabrication of large area subwavelength antireflection gratings on silicon”, Applied Physics Letters, vol. 91, pp. 231105, December 2007.

[155] Y.F. Huang et al., “Improved broadband and quasi-omnidirectional antireflection properties with biomimetic silicon nanostructures”, Nature Nanotechnology, vol. 2, pp. 770-774, December 2007.

[156] J.W. Leem et al., “Nanostructured encapsulation cover glasses with wide angle broadband antireflection and self-cleaning properties for III-V multi-junction solar cell application”, Solar Energy Materials and Solar Cells, vol. 120, pp 555-560, January 2014.

[157] G. B. Goffredo, “Smart surfaces for architectural heritage: self-cleaning titanium dioxide nano-coatings on trevartine”, Thesis 2013.

[158] M. Qu, J. He and J. Zhang, Superhydrophobicity, Learn from the Lotus Leaf", Intech, Available: http://www.intechopen.com/books/biomimetics-learning-from-nature/superhydrophobicity-learn-from-the-lotus-leaf

[159] Y.L. Zhang et al., "Recent developments in superhydrophobic surfaces with unique structural and functional properties", Soft Matter, vol. 8, pp. 11217-11231, August 2012.

[160] A. J. C. Sanchez (2013, October 9), "Superficies Superhidrofilas Y Superhidrofobas", Ingenieria de Materiales, Available: http://www.ingenieriadememateriales.com/articulo-superficies-superhidrofilas-y-superhidrofobas/

[161] M. Faustini et al., "Hydrophobic, antireflective, self-cleaning, and antifogging sol-gel coatings: An example of multifunctional nanostructured materials for photovoltaic cells", Chemical Materials, vol. 22, pp. 4406-4413, July 2010.

[162] S. Guldin et al., "Self-cleaning antireflective optical coatings", Nano Letters, vol. 13, pp. 5329-5335, October 2013.

[163] V.A. Ganesh et al., "Photocatalytic superhydrophilic TiO_2 coating on glass by electrospinning", RSC Advances, vol. 2, pp. 2067-2072, January 2012.

[164] D. Verhovsek et al., "The synthesis of anatase nanoparticles and the preparation of photocatalytically active coatings based on wet chemical methods for self-cleaning applications", International Journal of Photoenergy, Article ID 329796, pp. 1-10, March 2012.

[165] Z. Zhao et al., "Orientated anatase TiO_2 nanocrystal array thin films for self-cleaning coating", Chemical Communications, vol. 49, pp. 8958-8960, August 2013.

[166] F. Shi, Z. Wang, and X. Zhang, "Combining a layer-by-layer assembling technique with electrochemical deposition of gold aggregates to mimic the legs of water striders", Advanced Materials, vol. 17, pp. 1005-1009, April 2005.

[167] Colburn et al., "Development and advantages of step-and-flash lithography", Available: http://www.molecularimprints.com/pdf/archives/tech_articles/TA_colburn_bailey_choi.pdf

[168] Y.C. Tsai, M.D. Wu, and W.P. Shih, "Fabrication and characterization of e-beam photoresist array for biomimetic self-cleaning dry adhesives", Microelectronic Engineering, vol. 88, pp. 2126-2128, August 2011.

[169] R. Furstner et al., "Wetting and self-cleaning properties of artificial superhydrophobic surfaces", Langmuir, vol. 21, pp. 956-961, January 2005.

[170] B. Liu et al., “Fabricating super-hydrophobic lotus leaf like surfaces through soft lithographic imprinting”, Macromolecular Rapid Communications, vol. 27, pp. 1859-1864, November 2006.

[171] T. Zhang et al., “Black silicon with self-cleaning surface prepared by wetting processes”, Nanoscale Research Letters, vol. 8, pp. 351-355, August 2013.

[172] B.B. Wang, J.T. Feng, Y.P. Zhao, and T.X. Yu, “Fabrication of novel superhydrophobic surfaces and water droplet bouncing behaviour – part 1: stable ZnO-PDMS superhydrophobic surface with low hysteresis constructed using ZnO nanoparticles”, Journal of Adhesion Science and Technology, vol. 24, pp. 2693-2705, January 2010.

[173] E. K. Kim, T. Hwang, and S.S. Kim, “Change in microstructure and surface properties of electrospray-synthesized silica layers”, Journal of Colloid and Interface Science, vol. 364, pp. 561-565, December 2011.

[174] Y. Yin, and X. Wang, “Enhanced bioactivity of sandblasted and acid-etched titanium surfaces”, Advanced Materials Research, vol. 79, pp. 393-396, August 2009.

[175] M. M. Stanton et al., “Super-hydrophobic, highly adhesive, polydimethylsiloxane (PDMS) surfaces”, Journal of Colloid and Interface Science, vol. 367, pp. 502-508, February 2012.

[176] R.K. Wang, H.R. Liu, and F.W. Wang, “Facile preparation of raspberry-like superhydrophobic polystyrene particles via seeded dispersion polymerization”, Langmuir, vol. 29, pp. 11440-11448, August 2013.

[177] D. Hong et al., “Preparation of superhydrophobic, long-neck vase-like polymer surfaces”, Physical Chemistry Chemical Physics, vol. 15, pp. 11862-11867, May 2013.

[178] V.A. Ganesh et al., “Superhydrophobic fluorinated POSS-PVDF-HFP nanocomposite coating on glass by electrospinning”, Journal of Materials Chemistry, vol. 22, pp. 18479-18485, July 2012.

[179] M. Ma et al., “Superhydrophobic fabrics produced by electrospinning and chemical vapour deposition”, Macromolecules, 38, pp. 9742-9748, October 2005.

[180] N. Vourdas, A. Tserepi, and E. Gogolides, “Nanotextured superhydrophobic transparent poly(methyl methacrylate) surfaces using high density plasma processing”, Nanotechnology, vol. 18, pp. 125304-125310, February 2007.

[181] E. Farsari, M. Kostopoulou, E. Amanatides, D. Mataras, and D.E. Rapakoulias, “Comparative study of plasma deposited fluorocarbon coatings on different substrates”, Journal of Physics D: Applied Physics, vol. 44, pp. 194007-194012, April 2011.

[182] S. Patra et al., "Hydrophobic self-cleaning surfaces of ZnO thin films synthesized by sol-gel technique", Journal of Physics D: Applied Physics, 42, pp. 075301-075304, July 2011.

[183] Y.K. Lai et al., "Bioinspired TiO_2 nanostructure films with special wettability and adhesion for droplets manipulation and patterning", Scientific Reports, vol.3, Article number: 3009, May 2013.

[184] I.P. Parkin, and R.G. Palgrave, "Self-cleaning coatings", Journal of Materials Chemistry, vol. 15, pp. 1689-1695, January 2005.

[185] L. Caballero, "Photoinactivation of Escherichia coli on acrylic paint formulations using fluorescent light", Dyes and Pigments, vol. 86, pp. 56-62, June 2010.

[186] S. Worasukhkhung et al., "Hydrophilic property of TiO_2 films sputtered on glass ITO for self cleaning glass and heat mirror applications", Procedia Engineering, vol. 32, pp. 780-786, November 2011.

[187] S.A. Boden, and D.M. Bagnall, "Optimization of moth-eye antireflection schemes for silicon solar cells", Progress in Photovoltaics: Research and Applications, vol. 18, pp. 195-203, March 2010.

[188] B.J. Kim, and J. Kim, "Fabrication of GaAs subwavelength structure for solar cell applications", 19, pp. A326-A330, April 2011.

[189] M. Burghoorn et al., "Single layer broadband anti-reflective coating for plastic substrates produced by full wafer and roll-to-roll step-and-flash nano-imprint lithography", Materials, vol. 6, pp. 3710-3726, August 2013.

[190] A. Marchand et al., "Contact angles on a soft solid: From Young's law to Neumann's law", Physical Review Letters, vol. 109, pp. 236101-236105, December 2012.

[191] A. Shahraz, A. Borhan, K. A. Fichthorn, "A theory for the morphological dependence of wetting on a physically patterned solid surface", Langmuir, vol. 28, pp. 14227-14237, September 2012.

[192] P.F. Rios et al., "The effects of nanostructure and composition on the hydrophobic properties of solid surfaces", Journal of Adhesion Science and Technology, vol. 20, pp. 563-587, March 2006.

[193] S. Strobel, C. Kirkendall, J.B. Chang, and K.K. Berggren, "Sub-10 nm structures on silicon by thermal dewetting of platinum", Nanotechnology, vol. 21, pp. 505301-505307, November 2010.

[194] Y.J. Oh, C.A. Ross, Y.S. Jung, Y. Wang, and C.V. Thompson, "Cobalt nanoparticle arrays made by templated solid-state dewetting", Small, vol. 5, pp. 860-865, February 2009.

[195] J.B. Schneider (2013, November 14), “Understanding the finite difference time domain method”, Available: http://www.eecs.wsu.edu/~schneidj/ufdtd/ufdtd.pdf

[196] D. C. Jenn, “Finite Difference Time-Domain Method in Three Dimensions”, Available: http://www.globalspec.com/reference/25292/203279/4-6-finite-difference-time-domain-method-in-three-dimensions.

[197] RSOFT products, Available: http://optics.synopsys.com/rsoft/

[198] Thin film deposition technology, Available: http://www.mdcvacuum.co.uk/resources/downloads/pdfs/sec8.pdf

[199] Fabrication Techniques, Available: http://www.ece.utep.edu/research/cdte/Fabrication/index.htm

[200] e-guns, Available: http://www.hositrad.com/vacuum-products/e-guns/

[201] R.B. MacKnight et al., “RTP applications and technology options for the sub-45 nm nodes”, Proceedings, RTP 2004 Conference, Portland, USA, 2004.

[202] T. Tatsumi et al., “Etch rate control in a 27 MHz reactive ion etching system for ultralarge scale integrated circuit processing”, Journal of Vacuum Science and Technology, vol. 17, pp. 1562-1569, July 1999.

[203] E. R. Parker et al., “Inductively coupled plasma etching of bulk titanium for MEMS applications”, Journal of the Electrochemical Society, vol. 152, pp. C675-C683, August 2005.

[204] P. Strasser et al., “An ICP-RIE etching process for InP-based photonic crystals using $Cl_2/Ar/N_2$ chemistry”, Proceedings, International Conference on Indium Phosphide and Related Materials, pp. 242-245, May 2005.

[205] Y. Wang et al., “Integrated SOI rib waveguide using inductively coupled plasma reactive ion etching”, IEEE Journal of Selected Topics in Quantum Electronics, vol. 11, pp. 254-259, January/February 2005.

[206] M.V. Galiova et al., “Elemental mapping in fossil tooth root section of Ursus arctos by laser ablation inductively coupled plasma mass spectrometry (LA-ICP-MS)”, Talanta, vol. 105, pp. 234-243, February 2013.

[207] Lindarti Purwaningsih, “Fabrication of nanostructured materials and their applications”, Thesis for Master of Science, 2011.

[208] Newport, “Simulation of solar radiation” Available: http://www.newport.com/Technical-Note-Simulation-of-Solar Irradiation/411986/1033/content.aspx

[209] M. Andersen, and J. de Boer, “Goniophotometry and assessment of bidirectional photometric properties of complex fenestration systems”, Energy and Buildings, vol. 38, pp. 836-848, July 2006.

[210] M.Q. Liu et al., “Study on methodology of LED’s luminous flux measurement with integrating sphere”, Journal of Physics D: Applied Physics, vol. 41, pp. 144012, July 2008.

[211] M.L. Rastello, E. Miraldi, and P. Pisoni, “Luminous-flux measurements by an absolute integrating sphere”, Applied Optics, vol.35, pp. 4385-4391, August 1996.

[212] Y.S. Khoo et al., “Comparison of angular reflectance losses between PV modules with planar and textured glass under Singapore outdoor conditions”, IEEE Journal of Photovoltaics, vol. 4, pp. 362-367, January 2014.

[213] M. Nakamura, M. Masuda, and K. Shinihara, “Multiresolutional image analysis of wood and other materials”, Journal of Wood Science, vol. 45, pp. 10-18, February 1999.

[214] “Goniophotometer testing services for glass and windows” Available: http://www.eguide.com.sg/Companies/Solar-Energy-Research-Institute-of-Singapore-SERIS/Goniophotometer-Testing-Services-for-Glass-and-Windows-8509

[215] W.L. Min, B. Jiang, and P. Jiang, “Bioinspired self-cleaning antireflection coatings”, Advanced Materials, vol. 20, pp. 3914-3918, August 2008.

[216] Schott Glass, “Optical Properties”, Available: http://www.schott.com/borofloat/english/attribute/optical/index.html?so=singapore&lang=english

[217] C.V. Thompson, “Solid state dewetting of thin films”, Annual Review of Materials Research, vol. 42, pp. 399-434, May 2012.

[218] H.V. Kanel et al., “Epitaxy of metal silicides”, Thin Solid Films, vol. 184, pp. 295-308, January 1990.

[219] J. Lienemann et al., “Modeling, simulation and experimentation of a promising new packaging technology: Parallel fluidic self-assembly of microdevices”, Sensors Update, vol. 13, pp. 3-43, November 2003.

[220] V.I. Merkulov et al., “Patterned growth of individual and multiple vertically aligned carbon nanofibres”, vol.36, pp. 3555-3558, April 2000.

[221] F.M. Davidson et al., “Lamellar twinning in semiconductor nanowires”, Journal of Physical Chemistry C, vol. 111, pp. 2929-2935, January 2007.

[222] S. Tiwari et al., “A silicon nanocrystals based memory”, Applied Physics Letters, vol. 68, pp. 1377-1379, March 1996.

[223] F. Cheynis et al., “Stress effects on solid-state dewetting of nano-thin films”, International Journal of Nanotechnology, vol. 9, pp. 396-411, February 2012.

[224] L.K. Verma, M. Sakhuja, J. Son, A.J. Danner, H. Yang, H.C. Zeng, and C.S. Bhatia, “Self cleaning and antireflective packaging glass for solar modules”, Renewable Energy, vol. 36, pp. 2489-2493, September 2011.

[225] J.W. Leem, Y. Yunhae, J. Su, “Enhanced transmittance and hydrophilicity of nanostructured glass substrates with antireflective properties using disordered gold nanopatterns” Optics Express, vol. 20, pp. 4056-4066, February 2012.

[226] V. Zorba, X. Chen,and S.S. Mao, “Superhydrophilic TiO_2 surface without photocatalytic activation” Applied Physics Letters, vol. 96, pp. 093702-093704, March 2010.

[227] Taylor JM, Scattering Theory, Optical Binding Phenomena: Observations and Mechanism, Springer Theses 2011; pp. 11-49.

[228] Saleh BEA, Teich MC. Fundamentals of Photonics, second ed. Wiley, Hoboken 2007.

[229] S. Venkataraj, J. Wang, P. Vayalakkara, and A.G. Aberle, “Light scattering enhancement by double scattering technique for multijunction thin film silicon solar cells”, IEEE Journal of Photovoltaics, vol. 3, pp. 605-612, April 2013.

[230] K. Lovchinov et al., “Correlation between the haze ratio and the surface roughness of electrochemically deposited nanostructured ZnO films”, Journal of Physics: Conference Series, vol. 356, pp. 012025, 2012.

[231] American Chemical Society, “Self-cleaning technology from Mars can keep terrestrial solar panels dust-free”, Available: http://www.acs.org/content/acs/en/pressroom/newsreleases/2010/august/self-cleaning-technology-from-mars-can-keep-terrestrial-solar-panels-dust-free.html

[232] F. Padera (2009, November 4), “Haze measurements using an integrating sphere”, PerkinElmer UV/Vis/NIR Spectroscopy Resource Page, Available: http://pe.taylorjl.net/PE_Blog/?p=183

[233] K. Vogt, “Optische Untersuchungen an der Cornea der MehlmotteEphestia kuhniella”, Journal of Comparitive Physiology, vol. 88, pp. 201-206, 1974.

[234] P. Benjamin and C. Weaver, “The adhesion of evaporated metal films on glass”, Proceedings of The Royal Society A: Mathematical, Physical and Engineering Sciences, vol. 261, pp. 516-531, 1961.

[235] D.A.G. Bruggeman, “Effective medium theories”, Annual Physics, vol. 24, pp. 636-679, 1935.

[236] J. Son, S. Kundu, L.K. Verma, M. Sakhuja, A.J. Danner, C.S. Bhatia, and H. Yang, “A practical Superhydrophilic self cleaning and antireflective surface for outdoor photovoltaic applications”, Solar Energy Materials and Solar Cells, vol. 98, pp. 46-51, 2012.